BRNO UNIVERSITY OF TECHNOLOGY

VYSOKÉ UČENÍ TECHNICKÉ V BRNĚ

CENTRAL EUROPEAN INSTITUTE OF TECHNOLOGY BUT

STŘEDOEVROPSKÝ TECHNOLOGICKÝ INSTITUT VUT

SUPPORTED NANOSTRUCTURED PD CATALYST USING ATOMIC LAYER DEPOSITION: FROM METHANOL OXIDATION TO HYDROGEN EVOLUTION REACTION

PODPOROVANÝ NANOSTRUKTUROVANÝ PD KATALYZÁTOR NA BÁZI DEPOZICE ATOMÁRNÍCH VRSTEV: OD OXIDACE METANOLU PO VÝVOJ VODÍKU

DOCTORAL THESIS

DIZERTAČNÍ PRÁCE

AUTHOR

AUTOR PRÁCE

Bilal Bawab, M.Sc.

SUPERVISOR

ŠKOLITEL

Dr. Ing. Jan Macák

BRNO 2024

Abstract

In this thesis, the catalytic capabilities of Pd species deposited by Atomic Layer Deposition (ALD) was explored on different substrates. Pd species composed of Nanoparticles (NPs) and Single atoms (SAs) were synthesized on anodic TiO_2 nanotube (TNT) layers and carbon papers, respectively, to investigate their performance in methanol electro-oxidation and the alkaline hydrogen evolution reaction (HER). Pd NPs were deposited on TNT layers as methanol oxidation catalyst, leveraging their large surface area and direct electrical contact through the titanium foil. TEM analysis showed Pd particle sizes between 7 and 12 nm, with a shift to a porous Pd layer formation beyond 450 ALD cycles. Cyclic voltammetry revealed that catalytic activity peaked at 400 and 450 cycles, indicating optimal Pd loading and anti-poisoning characteristics, potentially enabling direct CH_3OH to CO_2 conversion. The other role the Pd achieved through the presence of SAs and NPs. Pd species were decorated on carbon papers were studied as HER catalyst. the samples before and after electrochemical measurements were characterized with X-ray photoelectron spectroscopy confirming the presence of Pd^{2+} species. The electrochemical active surface area increased significantly with ALD cycles, reaching a plateau at 300c Pd. Notably, CP 600c Pd demonstrated an overpotential of 4.55 mV, the lowest reported for Pd electrocatalysts in alkaline conditions. This highlights the synergistic effects of Pd configurations on HER enhancement and explores the mechanism by which the HER process occurs.

Abstrakt

V této práci byly zkoumány katalytické schopnosti druhů Pd deponovaných metodou Atomic Layer Deposition (ALD) na různých substrátech. Druhy Pd složené z nanočástic (NP) a jednotlivých atomů (SA) byly syntetizovány na vrstvách anodických nanotrubiček TiO_2 (TNT) a uhlíkových papírech, aby se prozkoumalo jejich chování při elektrooxidaci methanolu a reakci vývoje alkalického vodíku (HER). Pd NP byly naneseny na vrstvy TNT jako katalyzátor oxidace methanolu, čímž se využil jejich velký povrch a přímý elektrický kontakt přes titanovou fólii. TEM analýza ukázala velikosti částic Pd mezi 7 a 12 nm, s posunem k tvorbě porézní vrstvy Pd po 450 cyklech ALD. Cyklická voltametrie odhalila, že katalytická aktivita dosáhla vrcholu po 400 a 450 cyklech, což ukazuje na optimální zatížení Pd a vlastnosti proti otravě, což potenciálně umožňuje přímou konverzi CH_3OH na CO_2. Další role Pd dosáhla přítomností SA a NP. Druhy Pd byly dekorovány na uhlíkových papírech a byly studovány jako HER katalyzátor. vzorky před a po elektrochemických měřeních byly charakterizovány rentgenovou fotoelektronovou spektroskopií potvrzující přítomnost druhů Pd^{2+}. Elektrochemicky aktivní povrchová plocha se významně zvýšila s cykly ALD a dosáhla plató při 300c Pd. Pozoruhodné je, že CP 600c Pd vykazoval nadměrný potenciál 4,55 mV, což je nejnižší hodnota udávaná pro Pd elektrokatalyzátory v alkalických podmínkách. To zdůrazňuje synergické účinky Pd konfigurací na zesílení HER a zkoumá mechanismus, kterým dochází k HER procesu.

Keywords

Atomic Layer Deposition, HER, MOR, catalysis, Pd species, poisoning, overpotential, alkaline, stable, water splitting, clean hydrogen, fuel cells.

klíčová slova

Depozice Atomové Vrstvy, HER, MOR, katalýza, druhy Pd, otrava, nadměrný potenciál, alkalický, stabilní, štěpení vody, čistý vodík, palivové články.

Table of content

Acknowledgments

Foremost, I am profoundly thankful to my supervisor, Dr. Jan Macak, whose continuous guidance have been crucial throughout my entire PhD program. His continuous follow up in addition to the constructive criticism has improved my scientific and writing skills enormously. I also want to express my gratitude for giving me the chance to participate in the scientific conferences where I got the opportunity to meet specialists in the deposition field.

I would also like to acknowledge my former colleagues in Dr. Jan Macak's research group, including Dr. Siowwoon Ng, Pavan Kumar Chennam, Dr. Mahnaz Alijani, Ahmet Erdem Ince, Kaushik Baishya, Nasrollah Naseri Joda, Dr. Martina Říhová, Dr. Hanna Ingrid Sopha, and last but not least to Dr. Ivan Saldan for his continuous follow up with HERMES project.

I thank Dr. Eva Kolíbalova for her help with the TEM characterization, Dr. Ondrej Man for TEM lamella preparation, for Dr. Raúl Zazpe for his informative support during the ALD processes and for Jhonatan Rodriguez-Pereira for his valuable input during XPS analysis.

I would like to acknowledge Dr. Sitaramanjaneya Mouli Thalluri for the great motivation and support during the challenging periods of my academic pursuit. His support has been a cornerstone in overcoming the obstacles of my doctoral research journey.

My academic journey has been significantly enriched through the lectures given by several exceptional professors, each of whom has contributed to my growth. I would like to express my appreciation to Dr. Jan Macak, Prof. Jaroslav Cihlář, and Dr. Hermann Detz, whose classes have left important source of knowledge on my academic experience.

Special thanks for Prof. Giovanni Zangari for accepting me as a visiting student during my internship at the University of Virginia, USA. His invaluable mentorship, both within and outside the laboratory, has been an enriching experience. Additionally, I extend my gratitude to the members of Prof. Zangari's research group, including Qiyuan Lin, Yin Xu, Ahmed Rasin, Yunkai Sun, Amir Chamaani, and Lee Kendall, for their support.

I am grateful to my family for their endless support and love, especially my parents, who have been by my side throughout the journey. I must not miss my brother Ali Bawab for the deep conversations we had along the way, which gave me tremendous inspiration.

Last but not least, I acknowledge the Central European Institute of Technology - CEITEC Nano Research Infrastructure for the measurements/sample fabrication. In addition, I acknowledge the Center of Materials and Nanotechnologies at the University of Pardubice, where the photoelectrochemical measurements has been carried out.

Author's declaration

I declare that I have conducted this doctoral thesis titled "Supported Nanostructured Pd Catalyst Using Atomic Layer Deposition: From Methanol Oxidation to Hydrogen Evolution Reaction", independently, under the supervision of Dr.-Ing. Jan Macak. The work includes proper citations and references from relevant literature and professional sources.

Bilal Bawab

List of conferences attended and posters/talks presented

- **NANOCON 2021, 13th International Conference on Nanomaterials – Research and Application.** Brno, Czech Republic. October 20 – 22, 2021

Poster: *Anodic TiO_2 Nanotube Layers as Scaffolds for Deposition of Functional Materials*

- **Regional Meeting of the International Society of Electrochemistry – ISE**. Prague, Czech Republic. August 15, 2022

Oral presentation: *Cu_2O: a Photoanodic Functional Material and Its Stabilization Against Oxidation*

- **CEITEC PhD Retreat**. Telč, Czech Republic. September 3, 2022

Oral presentation: *Cu_2O: a Photoanodic Functional Material and Its Stabilization Against Oxidation*

List of publications

- **B. Bawab**, S. M. Thalluri, J. Rodriguez-Pereira, H. Sopha, R. Zazpe, and J. M. Macak, "Anodic TiO_2 nanotube layers decorated by Pd nanoparticles using ALD: An efficient electrocatalyst for methanol oxidation," *Electrochimica Acta*, vol. 429, p. 141044, Oct. 2022, doi: 10.1016/j.electacta.2022.141044. **(I.F. 6.6)**

- S. M. Thalluri J. Rodriguez-Pereira, R. Zazpe, **B. Bawab**, E. Kolíbalová, L. Jelinek, and Jan M. Macak, "Enhanced C-O Functionality on Carbon Papers Ensures Lowering Nucleation Delay of ALD for Ru towards Unprecedented Alkaline HER Activity," Small, vol. 19, no. 32, Apr. 2023, doi: 10.1002/smll.202300974. **(I.F. = 13.3)**

- **B. Bawab***, S. M. Thalluri, E. Kolíbalová, R. Zazpe, L. Jelinek, J. Rodriguez-Pereira, J. M. Macak, "Synergistic effect of Pd single atoms and nanoparticles deposited on carbon supports by ALD boosts alkaline hydrogen evolution reaction," Chemical Engineering Journal, vol. 482, p. 148959, Feb. 2024, doi: 10.1016/j.cej.2024.148959. **(I.F. = 15.1)**

* B. Bawab and Sitaramanjaneya M.Thalluri contributed equally to this paper

List of abbreviations

ALD Atomic Layer Deposition

CA Chronoamperometry

C_{dl} Double-Layer Capacitance

CE Counter Electrode

CV Cyclic Voltammetry

DMFC Direct Methanol Fuel Cell

ECMF Electrochemical Milling and Faceting

ECSA Electrochemical Surface Area

EDX Energy-Dispersive X-Ray Spectroscopy

EIS Electrochemical Impedance Spectroscopy

Eq. Equation

FE Faradaic Efficiency

FFT Fast Fourier Transformation

FTO Fluorine-doped Tin Oxide

HAADF-STEM High-Angle Annular Dark-Field Scanning Transmission Electron Microscopy

HER Hydrogen Evolution Reaction

ICP-OES Inductively Coupled Plasma Optical Emission Spectrometry

LSV Linear Sweep Voltammetry

MOR Methanol Oxidation Reaction

N_{ALD} Number of ALD cycles

NP/s Nanoparticle/s

OER Oxygen Evolution Reaction

PGU Potentiostat/Galvanostat Unit

Q_M Charge for Monolayer Reduction

R_{ct} Charge Transfer Resistance

RE Reference Electrode

RHE Reference Hydrogen Electrode

SA/s Single atom/s

SAED Selected-Area Electron Diffraction

SEM Scanning Electron Microscopy

TEM Transmission Electron Microscopy

TNT/s Titanium Dioxide Nanotube/s

TOF Turnover Frequency

WE Working Electrode

XPS X-Ray Photoelectron Spectroscopy

XRD X-ray Diffraction

ΔG_{H^*} Hydrogen Absorption Energy

1. Chapter 1: Introduction

1.1. General overview and background

The demand for sustainable energy solutions has become increasingly urgent in the face of escalating energy demands and environmental concerns. As traditional fossil fuels continue to dominate global energy production, the imperative to transition towards cleaner alternatives has become undeniable. Among the group of emerging energy sources, hydrogen gas (H_2) stands out as a promising fuel [1], transition to a new era of clean and efficient energy utilization. H_2 possesses several key attributes that make it an important prospect for energy production. Its remarkable energy density, coupled with its ease of storage and transport, result in an exceptionally versatile fuel option. Furthermore, H_2 combustion yields only water as a byproduct, offering a compelling solution to overcome greenhouse gas emissions.

The color-coding system for H_2 is a simple way to indicate the source and environmental impact of H_2 production. Green H_2 is produced using renewable energy sources such as wind or solar power, making it the most sustainable option. Blue H_2 is derived from natural gas with capturing the emitted carbon capture to minimise harmful emissions. Grey H_2 is also made from natural gas but without capturing the emitted carbon, leading to higher emissions. H_2 can be produced from coal in two forms: The color distinction refers to the type of coal used. Turquoise H_2 is produced through a process called methane pyrolysis, which yields H_2 and solid carbon. Purple and Pink H_2 are generated using electrolysis that involve nuclear energy. White H_2 is naturally occurring and found underground. **Table 1.1** summarise some of the mostly used techniques to produce H_2. The current methods of H_2 production include drawbacks. Processes such as steam reforming of natural gas or coal gasification heavily rely on carbon-based resources, perpetuating carbon emissions and environmental degradation. Despite the high efficiencies, it is important to explore alternative processes that are more sustainable. Consequently, there is an urgent imperative to develop innovative and sustainable approaches to H_2 generation. Among the various pathways to clean H_2 production, water splitting emerges as a particularly promising solution. This process involves the dissociation of water molecules into H_2 and oxygen gases, typically facilitated by the application of an electric current or harnessing solar energy. Beyond

its intrinsic environmental benefits, water splitting holds immense potential for integration with fuel cells [2].

Table 1.1. *Efficiency % estimation and environment impact of different processes to extract H_2.*

Process	**Identification color**	**Efficiency (%)**	**ref**	**Environmental Impact**
Photoelectrochemical Cells	Green	10-18%	[3]	Low (No CO_2 emissions)
Steam Reforming of Natural Gas	Grey	~81%	[4], [5]	High (CO_2 emissions)
Coal Gasification	Brown/black	60-70	[6], [7]	High (CO_2 emissions)
Electrolysis of Water (water splitting)	Green/pink/purple	95	[8]	Moderate (Energy Intensive)

Fuel cells represent a cornerstone of the transition towards a sustainable energy future. By harnessing the chemical energy of H_2 and O_2, these devices can efficiently generate electricity [9] while emitting only water compared to the pollutants associated with conventional combustion engines. Fuel cells have acquired significant attention, particularly in the transportation sector, where they offer a compelling alternative to traditional internal combustion engines, promising enhanced efficiency and reduced emissions.

1.2. Process of water splitting reaction.

Water splitting is a process that involves two half-reactions: the hydrogen evolution reaction (HER) and the oxygen evolution reaction (OER), which occur at the cathode and the anode of the water splitting device, respectively. Both reactions have high thermodynamic and kinetic barriers, which means that they require a large amount of energy and a long time to complete. Therefore, the main challenge is to reduce the energy requirement and increase the reaction rate of both the HER and OER. For this purpose, various strategies have been employed to modify the electrode materials, optimize the electrolyte composition, and design novel catalysts.

The invested energy used to split water will be stored in H_2 molecule according to the following reaction:

$$H_2O + 237.2\ \text{kJmol (electricity)} + 48.6\ \text{kJmol (heat)} \rightarrow H_2 + \frac{1}{2}O_2 \qquad (1.1)$$

Where 237.5 kJ/mol is the Gibbs free energy, 48.6 kJ/mol is referred to the overpotential needed to drive the reaction forward, which then convert to heat and stored in H_2 molecule.

Figure 1.1 provide a representation of the activation energy (E_a) needed for the electrochemical system to be driven forward. The x-axis depicts the progress of the reaction, where the left and right sides represent the reactants and products of the reaction. The introduction of a catalyst significantly reduces the E_a required to reach the designated products compared to the absence of a catalyst. Consequently, the presence of a catalyst increases the reaction rate without affecting the thermodynamic equilibrium, which is described by Gibbs free energy (Eq. 1.1). It is important to note that a negative Gibbs free energy ($G < 0$) is required for the reaction to be spontaneous.

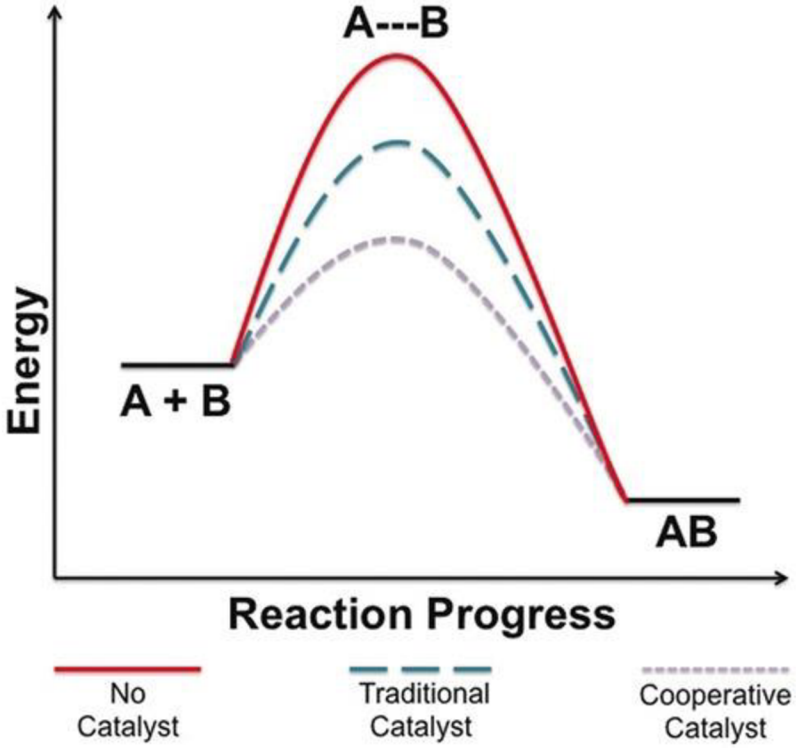

Figure 1.1. *Activation energy diagram for electrochemical system with and without a catalyst* [10].

Among the different types of catalysts, noble metal-based materials have shown remarkable performance for both the HER and OER, due to their high intrinsic activity, good conductivity, and high stability [11]. However, the high cost and scarcity of noble metals limit their large-scale application and motivate the search for alternative and cheaper catalysts. One of the most studied and promising materials is Palladium (Pd). Pd has a high catalytic activity and selectivity for the HER due to the H-Pd bonding discussed in **section 1.5** of this chapter, as well as a good stability and resistance to poisoning. One of the effective ways to reduce the Pd loading and enhance its utilization is to deposit Pd NPs on 2D carbon supports [12], such as graphene [13], carbon nanotubes [14] or carbon papers [15]. The carbon supports can provide a large surface area, a high electrical conductivity, and a strong interaction with Pd NPs, which can improve the dispersion, stability, and activity of Pd catalysts. Moreover, the 2D carbon supports can also be doped with heteroatoms, such as N, S, or P, to create more active sites and modify the electronic structure of Pd catalysts [16]. Pd is a metal that can absorb and release large amounts of H_2 gas reversibly, making it a potential material for H_2 storage and purification [17]. Pd can form an alloy with hydrogen, called palladium hydride, which has a higher hydrogen-to-metal ratio than other metal hydrides. Palladium hydride can store up to 900 times its own volume of H at room temperature and atmospheric pressure [18].

1.3. Pd catalyst deactivation and limitations

The most commonly used catalysts for HER and OER are based on precious metals/metals oxides such as platinum (Pt) and iridium oxide (IrO_2), which have high activity and stability in acidic media, but are scarce and expensive, For example, a study by Guillen-Soler et al. [19] demonstrated that while Pd nanoparticles can enhance the HER when used in a hybrid structure with MoS_2 and polyoxometalate (POM), the scarcity and high cost of Pd make it impractical for widespread application. In contrast, non-precious metal catalysts such as nickel-based (Ni-based) [20] and copper-based (Cu-based) [21] catalysts are more abundant and cheaper. However, it faces challenges such as rapid charge recombination and susceptibility to photo-corrosion, which limit its efficiency and durability. Pd has been reported to exhibit bifunctional catalytic properties for both OER and HER in acidic media and can deliver low overpotentials. However, the efficiency of the catalyst can be significantly affected by its microstructure and the platform on which it is used. Therefore, it is important to search for a catalyst design that can meet the

required standards for reducing the amount of Pd used, both due to its high cost and the impact of its morphology, such as the crystalline planes and shapes, which directly affect the surface area exposed to the electrolyte and, consequently, the final efficiency of the catalyst. Additionally, Pd finds widespread application as a catalyst for methanol oxidation in direct methanol fuel cells (DMFCs). However, the catalytic performance of Pd is susceptible to degradation due to surface poisoning by adsorbed intermediate compounds, notably carbon monoxide (CO). The formation of stable CO layers on the Pd surface obstructs the active sites crucial for methanol and oxygen adsorption, consequently impairing catalytic activity and stability. Moreover, the catalyst's activity may decline over time due to the oxidative conditions which can lead to its deactivation.

Catalyst deactivation during electrochemical water splitting is a significant issue that affects both the efficiency and longevity of the system. This deactivation can occur due to various factors, including the accumulation of reaction intermediates on the catalyst surface and changes in the catalyst's active sites. Suryanto et al. [22] discussed the development of a nickel–iron oxide interface catalyst that exhibits both HER and OER activity, but they also noted that maintaining this dual-functionality over time is challenging due to corrosion-induced compositional and structural changes.

1.4. Pd catalyst synthesis

The synthesis of Pd nanostructures can be performed through various techniques. The most used methods such as Chemical Vapor Deposition (CVD) [23], Sol-Gel Process [24], Microemulsion techniques [25], Sonochemical Synthesis [26]. Similarly, Microwave-Assisted Synthesis uses microwave radiation to achieve rapid and uniform heating [27], which can significantly reduce the synthesis time for Pd nanostructures. Electrodeposition and Atomic Layer Deposition (ALD) stand out as prominent methods due to the ease of synthesis and high controllability level respectively. Each technique offers unique advantages and challenges in tailoring Pd catalysts to meet specific application requirements.

In the electrochemical process such as electrodeposition, the presence of the Helmholtz layer at the electrode-electrolyte interface presents a complex interplay of benefits and challenges for accurate electrochemical measurements. One significant challenge arises from the limited mass

transport in the depletion region. This restricted ion diffusion can lead to concentration gradients near the electrode surface, potentially slowing down desired reactions and causing discrepancies in current-potential measurements. Furthermore, the applied potential directly influences the Helmholtz layer structure and composition, giving rise to double layer effects (ihp and ohp) as represented in **Figure 1.2**. The voltage drops across the layer described by Eq. 1.2 is caused by this potential-dependent phenomenon. This phenomenon also combines the potential drop with the pH of the electrolyte used, resulting in a difference between the applied and real potential experienced by the reacting species at the electrode surface. This deviation from ideal behavior complicates the study of reaction mechanisms and thermodynamic properties.

$$V_H = \frac{2.3kT}{e}(pH_0 - pH) \tag{1.2}$$

Where pH_0 is the pH at which the charge is equal to zero, T is the reaction temperature, k is the equilibrium constant, and e is the charge of an electron.

Fortunately, strategies exist to mitigate these challenges and achieve more reliable data. One approach involves tunning the supporting electrolyte concentration that can enhance the ion mobility within the bulk solution, reducing the impact of limited diffusion near the electrode. However, careful balancing is crucial, as overly concentrated electrolytes can promote unwanted side reactions. Another approach utilizes pulsed electrochemical techniques, like pulsed potential deposition. By turning on-off cycles of applied potential, promoting diffusion during the off-time and influencing the dynamics of the Helmholtz layer. This can minimize concentration gradients, suppress side reactions, and ultimately improve the efficiency and accuracy of electrochemical measurements.

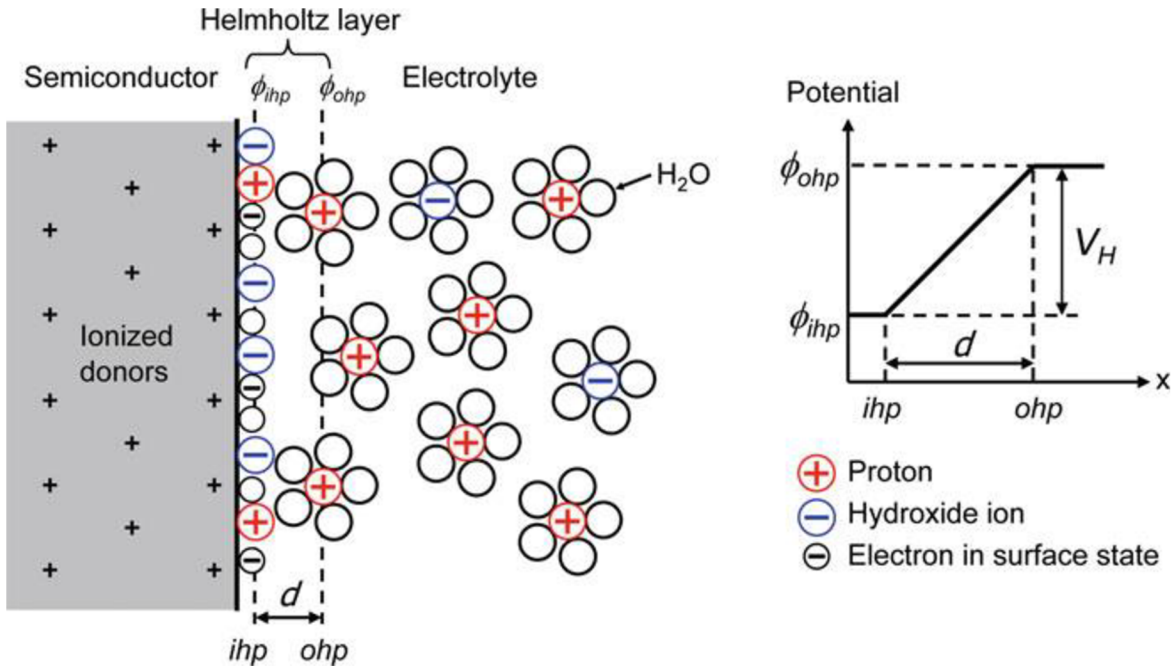

Figure 1.2. *Schematic representation of the inner (ihp) and outer(ohp) Helmholtz planes at the interface between the electrode surface and the electrolyte* [28].

The morphology and thickness of the Pd deposited layers can be controlled by varying the solution composition, potential, and time. However, pulsed potential electrodeposition (PPD) as represented in **Figure 1.3** offers distinct advantages over its continuous counterpart. This method capitalizes on the crucial role of the pause time, the interval between deposition pulses, to achieve improved film characteristics and address limitations inherent in continuous deposition. The key advantage of PPD lies in its ability to control the morphology and properties of deposited films. The pause time facilitates diffusion, replenishing the depletion zone formed during the pulse and allowing adsorbed species to arrange themselves on the surface, ultimately leading to smoother, denser, and more uniform films [29]. Additionally, by manipulating the pulse duration and frequency, researchers can tailor the composition, crystal structure, and other

functional properties of the deposited material for specific applications [30].

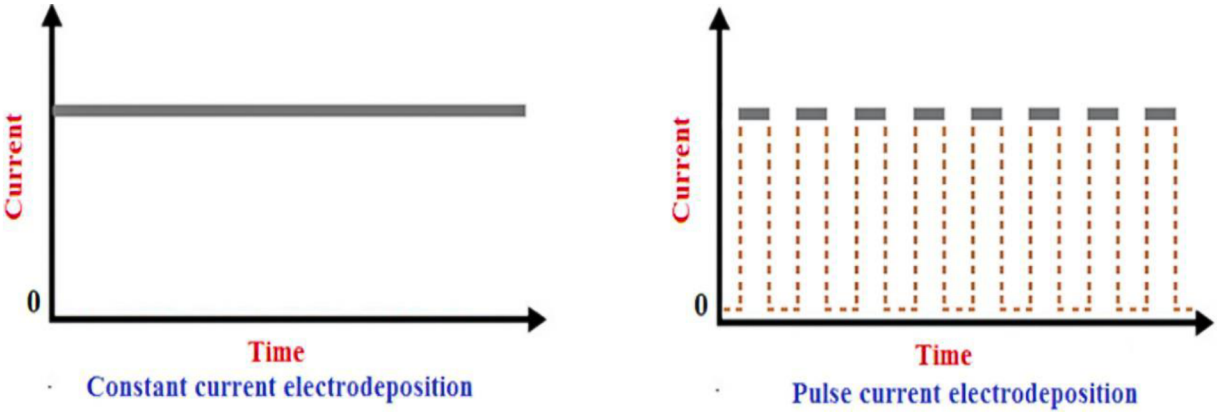

Figure 1.3. *Pulsed deposition versus continuous deposition diagram* [31]

It is important to note that while the pause time significantly reduces the depletion zone, complete elimination might not be achievable in all scenarios. The efficacy of depletion zone reduction depends on the interplay between pulse parameters, diffusion rates, and electrolyte properties. However, despite the partially depleted zone, PPD still offers significant advantages over continuous deposition, making it a preferred technique for various advanced material synthesis applications. Following each pulse, nucleated material, such as reduced Pd ions on existing Pd nuclei, continues to grow, resulting in the formation of various shapes and sizes of Pd nanostructures [32]. The nucleation and growth mechanism of Pd nanostructures by electrodeposition can be more complicated and depends on several factors, such as the solvent, Pd ion concentration, pulse duration and frequency, and substrate material. In the work of *Fuentes et al.* [33], Pd growth follows a 3D-controlled structure on the nucleated Pd^0 sites. The structural formations differ depending on the substrate used, forming spherical clusters on highly oriented pyrolytic graphite (HOPG) and cauliflower structures on Ti with a narrow size distribution.

The crystalline structure of electrodeposited Pd depends on the substrate, the precursor, and the deposition parameters. For example, Pd deposited on graphene oxide showed a flower-like morphology with (111) dominant facets, while Pd deposited on ITO showed spherical nanoparticles with (100) facets. The reason for obtaining different morphology is related to the nucleation and growth processes, the adsorption of anions or additives, and the surface energy of the facets. (111) facets for example have high surface energy, favouring rapid growth along these

planes. Result in polyhedral or dendritic shapes. (100) facets have lower surface energy, leading to slower growth. yield cubic or octahedral particles.

Previous works have tuned the relative exposure of (100) and (111) facets in Pd nanocrystals during formic acid oxidation. The resulting electrocatalytic activity varied with shape (cubes to octahedrons). However, during the nucleation mechanism, *Kim et al.* [34] propose a two-step nucleation mechanism for Pd on carbon electrodes, involving the formation of $(PdCl_4)^{2-}$ complexes and their subsequent reduction to Pd^0 atoms. A kinetic model has been developed for the growth of Pd nanoparticles on carbon electrodes, based on the aggregation of Pd atoms and the coalescence of Pd clusters. It was validated that the growth rate and particle size distribution depend on the applied potential and the $PdCl_2$ concentration.

Atomic Layer Deposition (ALD) ALD is a well-established gas phase deposition technique based on alternating self-limiting gas-surface chemical reactions. The precursors are introduced separately to react with the active surface sites followed by purging steps using an inert gas (N_2 or Ar) avoiding any chemical reaction in the gas phase between the precursors. The unparalleled sub-nanometer thickness control lies in the self-limiting nature of the chemical surface reactions, caused by the limited number of active surface sites (available to react with the gas phase precursor), restricting the growth process to one layer per cycle. The ALD cycle is repeated until the desired layer thickness is achieved. More importantly, ALD is the only deposition method that enables conformal and uniform deposition on complex substrates including high aspect ratio structures and nanostructured porous materials, regardless the electronic conductivity of the material to be deposited, unlike in the previously described electrodeposition technique [35]. ALD enables to deposit various types of materials, such as metal oxides, sulfides, nitrides, but also different noble metal nanostructures, which offers numerous fascinating opportunities, harvested in this work as well as in the recent literature.

The ALD process of noble metals (such as Pt or Pd), however does not follow the typical ALD layer by layer growth. Instead, the process starts by nucleation that occurs selectively on the surface sites that have a high affinity for the noble metal precursor, such as functional groups originated by the co-reactant, defects, steps, or edges. The growth rate and especially the size of the growing objects is strongly affected mainly by ALD parameters as the precursor of choice, the deposition temperature and the number of ALD cycles. As the number of cycles increases,

the single atoms (nuclei) atoms form clusters, which grow into nanoparticles with increasing number of cycles. The nanoparticles can eventually coalesce and form a continuous film as represented in **Figure 1.4**, depending on the surface mobility and the interparticle distance [36]. This is in strong contrast, to the typical growth of metal oxides that in general lacks of nucleation delay leading to the formation of uniform and continuous layers [37]. This is because metal oxides readily form strong metal-oxygen bonds. which result in a more uniform and complete layer on the substrate surface, leading to a layer-by-layer growth.

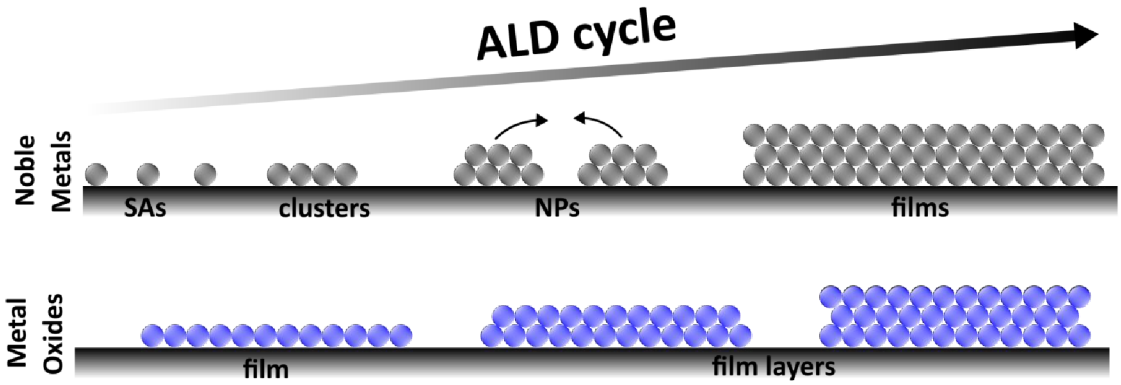

Figure 1.4. *Schematic representation of nucleation of noble metals during ALD process in comparison to classical ALD growth of e.g. metal oxides, both are drawn as function of ALD cycles that increase from left to right.*

In particular, the Pd ALD process involves two steps: firstly, exposing the substrate to a Pd precursor, such as Palladium (II) hexafluoroacetylacetonate ($Pd(hfac)_2$), which mainly adsorbs onto the active functional groups of the surface; secondly, exposing the substrate to a reducing agent, such as formalin or H_2, which reacts with the adsorbed precursor and forms Pd metal. The cycle is repeated until the desired metal size and/or morphology (clusters, nanoparticles, continuous film) is achieved. One must note that the ALD precursor must fulfilled three basic criteria: i) volatility to provide sufficient vapor pressure; ii) thermal resistance to withstand the deposition temperature (usually above 100°C); iii) reactivity with the substrate and the co-reactant. The precursor also should present additional features, such as to be chemically resistant toward air and moisture for easy handling, to be noncorrosive including by-products, to present low toxicity, and allow cost-effective and large-scale synthesis [38].

The selection of co-reactants, such as O_2, O_3, H_2O, or formaldehyde, further influences the interaction between the precursor and the substrate by influencing the nucleation sites. O_2 and O_3, for example, can promote the formation of bridging oxide species on the surface, influencing the growth pattern of film. Conversely, H_2O or formaldehyde can act as hydroxylating agents, modifying the surface termination and the adsorption of the metal precursor.

Sun et. al. [39] described the process at which the deposition of Pt for example nucleates on a carbon substrate using O_2 as a co-reactant. A monolayer of oxygen-containing functional groups act as anchoring points for the provided (methylcyclopentadienyl)-trimethylplatinum ($MeCpPtMe_3$) precursor in the second step of the ALD cycle. Upon exposure of the precursor, some of the ligands react with the adsorbed oxygen and form other species such as CO_2, H_2O, and hydrocarbon fragments as by-products. Consequently, controlling the distribution and uniformity of nucleation can be tuned by providing selective quantity of the co-reactant per each cycle.

Furthermore, the effect of substrate must be taken into account, when studying the growth mechanism. The growth of Pd on oxides or carbon substrates for example depends on several factors mentioned before in addition to the presence of functional groups on the surface, which directly influence the reactivity and the nucleation behaviour. According to the Volmer-Weber mechanism [40], Pd can form 3D islands on the carbon surface through instantaneous nucleation and diffusion-controlled growth [41]. The ALD temperature affects the size and shape of the Pd islands, as well as the surface diffusion and reaction kinetics of the Pd precursors. The surface morphology of the carbon substrate influences the distribution and density of the Pd islands, as well as the defects and edges that can act as nucleation sites [42]. The presence of functional groups on the carbon surface, such as hydroxyls, carboxyl's, sulfates, and sulfides, can modify the surface charge, the adsorption affinity, and therefore the oxidation state of the Pd atoms, leading to different nucleation and growth behaviours. When discussing other noble metals, such as Pt, the nucleation process is similar to that of Pd. In their study, *Han-Bo-Ram et. al.* [43] examined the effects of substrate microstructure, surface hydrophilicity, and catalytic activity on Pt nucleation and film formation during ALD. It was found increasing the thickness of the TiO_2 layers used for Pt nucleation resulted in the transformation from amorphous to anatase. This

recrystallisation occur due to the longer exposure of TiO_2 to heat with higher number of cycles to achieve the thicker layers. This transformation enhanced Pt nucleation, in addition to the hydrophilicity effect of the substrate, which enhanced the formation of the nucleation sites for wider Pt distribution and growth. Other studies have shown that carbon substrates with high oxygen content can induce the formation of Pd core-shell nanostructures [44], which have enhanced catalytic activity towards methanol oxidation reaction (MOR). However, other studies have reported that sulfur-containing functional groups can inhibit the Pd nucleation or cause the formation of PdS, which has lower catalytic activity [45]. Therefore, the nucleation and growth of Pd on carbon substrates is a sensitive and tuneable process that can result in various Pd nanostructures with different properties and applications.

The different structure formation of the deposited material can greatly affect its catalytic properties due to the different electronic structures and energy bands for each as shown in **Figure 1.5**. Single Atoms (SAs) have localized electronic states with separated energy levels. Each atom contributes well-defined atomic orbitals. These states are influenced by the atomic number and electronic configuration. While SAs can be catalytically active due to their high surface energy, unique electronic states, and strong interaction with the support [46], their low coordination number, SAs aggregates overtime leading to the loss in stability and activity [47]. For example, when Pd atoms are supported on a substrate or close to other atoms, their electronic states can be altered due to charge transfer or electronic interactions. This can lead to changes in the oxidation state of the Pd atoms and lower their catalytic properties.

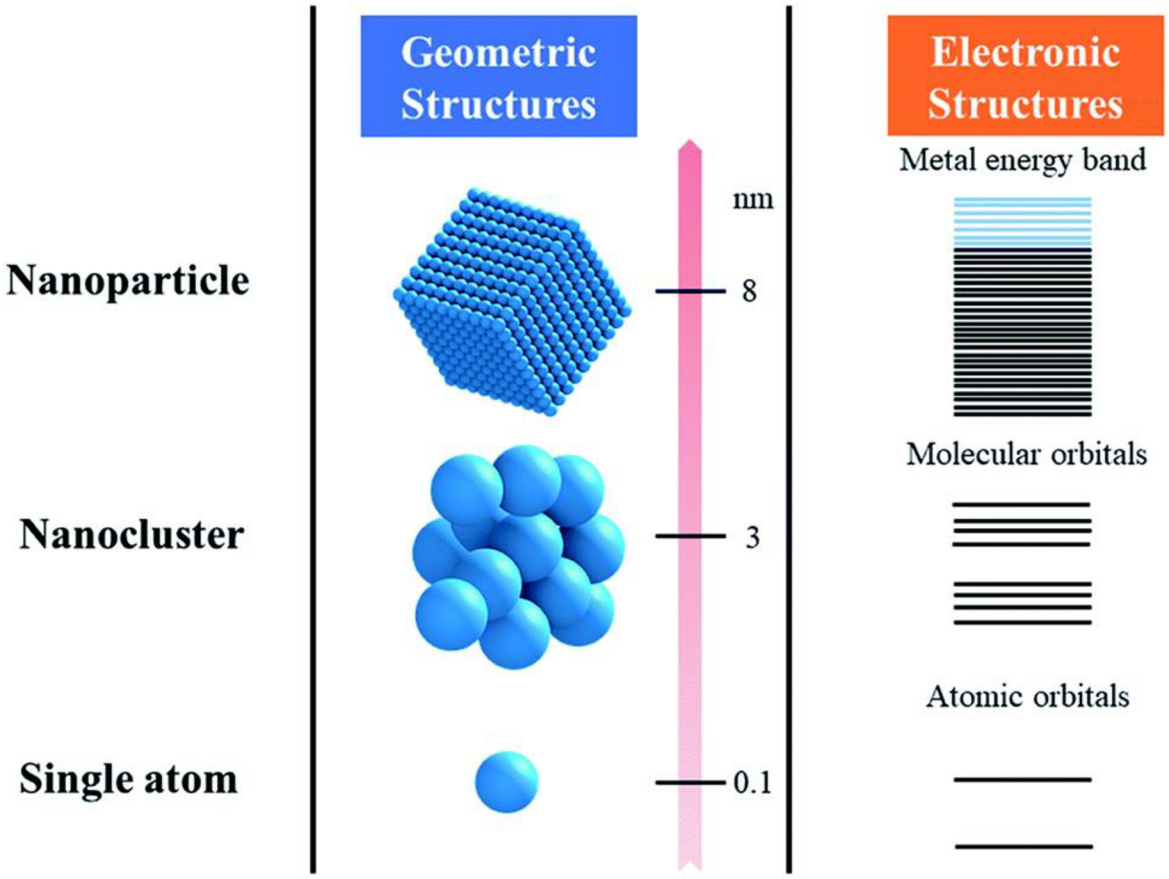

Figure 1.5. *Geometric and electronic structures of SAs, nanoclusters, and NPs* [48].

Nanoclusters consist of several hundred atoms. As the cluster size increases, the energy levels broaden into bands due to the hybridization of atomic orbitals within the cluster. On the other hand, nanoparticles contain thousands to millions of atoms and exhibit bulk-like behavior. Their electronic structure includes well-defined energy bands, resulting from collective interactions across the entire particle. During the HER process, the overlap of d-band states with hydrogen orbitals enables the efficient adsorption and dissociation of H_2 molecules, thereby promoting the reaction.

1.5. H-Pd bonding

The effect of hydrogen adsorption/desorption on Pd is detrimental to explain the Pd activity as a catalyst for water splitting reactions. For this reason, molecular orbital theory is used to describe the bonding between atoms. Molecular orbitals are the result of the overlap of atomic orbitals, which are the regions of space where electrons are most likely to be found around an atom.

When two atoms such as Pd and H approach each other, their atomic orbitals can interact and combine to form new orbitals that belong to the whole molecule and can hold electrons that are shared between the atoms. Generally, Pd forms stronger bonds with hydrogen when compared to Pt for example, because it has smaller atomic radius [49]. This means that Pd has higher adsorption and lower desorption energies of H when compared with Pt. How well transition metal-based catalysts can acquire and release H is also influenced by how the empty d orbitals of the transition metals and the s orbital of H interact with each other.

The strength of the bond depends on the energy difference and the electron occupancy of the molecular orbitals [50]. H has one "s" orbital, which is spherical and can overlap with any orbital of another atom. The s and p orbitals of Pd are similar to those of the second period elements, such as carbon (C), nitrogen (N), and oxygen (O), which can hybridize to form new orbitals. For example, carbon can form sp, sp2, or sp3 hybrid orbitals, depending on the number of bonds and lone pairs. These hybrid orbitals can then overlap with the s orbital of hydrogen to form sigma (σ) molecular orbitals [51], which are symmetrical along the bond axis. However, O and fluorine (F), which are also second period elements, cannot hybridize their s and p orbitals, because they have very different energies. The s orbital is much lower in energy than the p orbital, and the energy gap is too large for them to mix. Therefore, the s and p orbitals of O and F remain separate and do not form new orbitals. Instead, they overlap directly with the s and p orbitals of hydrogen to form sigma (σ) and pi (π) molecular orbitals, respectively.

The d orbitals of Pd are more complex and have different orientations and symmetries [52], which are characterized by increased complexity and a greater number of nodes compared to σ and π molecular orbitals. It is worth noting that Pd is unique among metals due to its Pauling electronegativity of 2.20, which is the same as H [53]. This allows for the sharing of electrons between H and Pd without the generating a large dipole, thus forming a hydride easily.

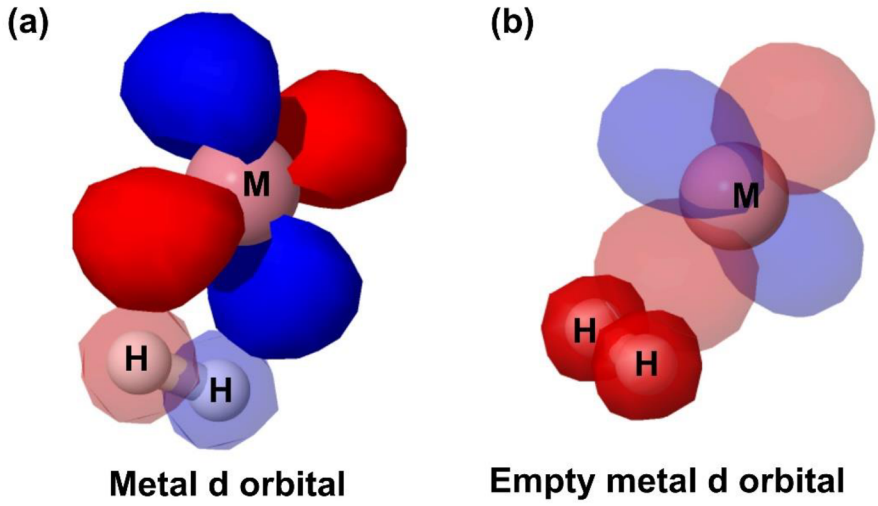

Figure 1.6. *Graphical representation of the bonding between H_2 on a metal with d orbital. Knowing that Pd have a full 4d orbital.*

Figure 1.6. represent the bonding diagram of H_2 with a metal 4d orbital. The (a) case represents full d orbital as the case of Pd and the (b) case represents the bonding in case of empty. The bond between two hydrogen atoms consists of both π and σ bonds. The σ bond is formed by the overlap of the dihydrogen orbital that holds the electrons. The π bond is formed by the transfer of electrons from the metal's d orbital to the dihydrogen orbital that weakens the bond. In the context of dissociative adsorption, H_2 on a Pd cluster is catalyzed by the dangling bonds of the Pd surface and electron correlations. Notably, the 4d orbitals of Pd play a pivotal role, with the outer 5s orbital assuming a secondary function in this catalytic process [54].

Dong et al. [55] reported how the atomic hydrogen interact with different facets of Pd crystals, such as (111), (100), and (110), which have different arrangements of atoms on the surface. They concluded that the higher hydrogenation activity of more open surfaces of Pd(110), could be related to the faster diffusion of hydrogen on the Pd crystalline plan. Another work by *Sampyo et. al.* [56] Describes the diffusion of hydrogen relative to different Pd crystalline plans. They compare the activation energy barriers for H to diffuse from the surface to the subsurface, and among different sites on the surface and the subsurface. It was found that the diffusion barrier from the surface to the subsurface on Pd (211) is lower than that on Pd (111), implying a higher

probability of finding subsurface hydrogen on Pd (211). Hydrogen prefers to bind at high coordination sites on all surfaces, with similar adsorption energies and geometries [57]. One of the descriptors for hydrogen binding on Pd is the d-band center which refers to the energy level of the d-orbitals of surface metal atoms. this band center can shift due to alloying with other elements such as indium (In) [58].

Finally, the nature of interaction of hydrogen with Pd enhances the catalytic activity of the system, facilitating the dissociative adsorption of H_2 and demonstrating the potential for designing Pd catalysts in a more "molecular" form. Where the dissociation of H_2 adsorbed molecule with least amount of energy leading to the dissociation of H_2 into to hydrogen atoms [59]. The important part is that this process completely reversible, with equilibrium between hydrogen molecule and radicals form as shown in Eq. 1.3 below.

$$H_2 \leftrightarrows H^* + H^* \tag{1.3}$$

It is worth noting that during the adsorption process, the stability of the Pd-Pd bond and the unique electronic interactions contribute to the catalytic ability of the system. This is due to electron back-transfer from the bonding MO of H_2 to that of Pd_2, which weakens the H-H bond but does not significantly affect the Pd-Pd bond.

1.6. Objectives of the thesis

a) Study the effect of Pd nanoparticles loaded within nanotubular TiO_2 substrates to overcome the poisoning issues that limit Pd activity during MOR.
b) Design and find the optimum Pd morphology and loading quantity for HER and compare the catalytic activity with the reported Pd catalyst in the literature.
c) Investigate the effect of using treated carbon substrates on the activity of Pd species, using ALD as a precision-controlled technique to synthesis Pd species. Where species can be associated with the presence of SAs, SA clusters, NPs, or all of these at the same time.

1.7. Contribution of the thesis

By following the proposed methodology, this thesis aims to exploit the most relevant aspects that govern the electrocatalyst performance along with the catalyst design using ALD. The successful synthesis of the catalyst for both MOR and HER, as mentioned in the objective section, will result in a more efficient catalyst design, ultimately saving more energy. Furthermore, the enhancement of the synthesised catalyst durability for water splitting devices is expected to reduce maintenance requirements, consequently lowering operational costs for end-users in the market. This strategic combination of methodologies not only aims to improve the catalyst design but also to address practical implications related to energy efficiency and cost-effectiveness in water splitting applications.

1.8. Outline of the thesis

The search for efficient and sustainable electrocatalysts for energy conversion processes has been a driving force in current research. **Chapter 1** of this dissertation starts by general introduction to provide understanding about different aspects that affect Pd catalytic activity and the use metal oxides as a promising cheap photocatalyst for water splitting. Additionally, it provides overview on the challenges encountered during the catalytic process of a catalyst and the studied solution to overcome these challenges. The fundamental aim of this research is to utilize the potential of Pd-based catalysts for two critical electrochemical reactions. MOR and HER are the focus of our investigation. Additionally, the use of ALD with controlled parameters has been investigated as a potential synthesis technique for designing a Pd catalyst, due to its exceptional precision and control. The sections of this thesis are structured with a specific focus on the catalysts synthesis techniques and their applications.

The **2nd chapter** of this thesis focuses on methanol oxidation reaction (MOR), a crucial process in fuel cells and direct methanol fuel cells (DMFCs). Methanol fuel cells have emerged as a promising technology for portable power sources and electric vehicles due to their high energy density. However, their widespread adoption has been hindered by the lack of efficient and durable MOR electrocatalysts. In this context, our research ventures into the precise deposition of Pd nanoparticles onto TiO_2 nanotubes (TNTs) using ALD. The novelty here lies in the intersection of ALD with MOR, a relatively unexplored research area. By employing ALD, high

level of control was achieved over Pd nanoparticle size and distribution, enabling us to tailor catalysts with remarkable performance and durability. This section aims to examine the complex interactions between Pd nanoparticles and TNTs, revealing the mechanisms that confer resistance to CO poisoning. Our research aims to tackle the crucial problem of CO poisoning in MOR and, as a result, presents a groundbreaking route towards sustainable methanol-based energy conversion.

In the **3rd chapter** studies the synergistic effects of Pd SAs and nanoparticles when deposited onto carbon papers (CPs) using ALD. The generation of clean and sustainable hydrogen is essential for a green energy future. HER plays a central role in hydrogen production technologies, and the search for efficient electrocatalysts is very important. The novelty lies in the unique combination of ALD and Pd-based catalysts for HER, offering precise control over the catalyst's atomic arrangement. By utilizing the inherent benefits of SAs and nanoparticles on CPs, overpotentials are significantly reduced, making these catalysts highly efficient. Our work paves the way for increase in HER efficiency and stability. Moreover, the detailed characterization techniques employed in this section not only provide valuable insights into the catalyst's structure but also ensure its long-term viability. This section thus contributes significantly to the field of clean hydrogen production and highlights the important role of ALD in catalyst design.

The importance of this study is its contribution to the development of sustainable water splitting as a clean source of energy. By connecting the dots between MOR, HER, this dissertation consolidates various aspects of electrochemical catalysis, each serving a specific objective to improve the energy conversion efficiency.

References

[1] T. da Silva Veras, T. S. Mozer, D. da Costa Rubim Messeder dos Santos, and A. da Silva César, "Hydrogen: Trends, production and characterization of the main process worldwide," *Int. J. Hydrogen Energy*, vol. 42, no. 4, pp. 2018–2033, 2017, doi: https://doi.org/10.1016/j.ijhydene.2016.08.219.

[2] Q. Hassan, S. Algburi, A. Z. Sameen, M. Jaszczur, and H. M. Salman, "Hydrogen as an energy carrier: properties, storage methods, challenges, and future implications," *Environ. Syst. Decis.*, 2023, doi: 10.1007/s10669-023-09932-z.

[3] M. F. Weber and M. J. Dignam, "Splitting water with semiconducting photoelectrodes—Efficiency considerations," *Int. J. Hydrogen Energy*, vol. 11, no. 4, pp. 225–232, 1986, doi: https://doi.org/10.1016/0360-3199(86)90183-7.

[4] Y. Shirasaki and I. Yasuda, "12 - Membrane reactor for hydrogen production from natural gas at the Tokyo Gas Company: a case study," in *Woodhead Publishing Series in Energy*, vol. 2, A. B. T.-H. of M. R. Basile, Ed., Woodhead Publishing, 2013, pp. 487–507. doi: https://doi.org/10.1533/9780857097347.2.487.

[5] New York State Energy Research and Development Authority, "HYDROGEN FACT SHEET Hydrogen Production – Steam Methane Reforming (SMR)," p. 4, 2004, [Online]. Available: www.nyserda.org

[6] R. Y. Kannah, S. Kavitha, O. P. Karthikeyan, G. Kumar, N. V. Dai-Viet, and J. R. Banu, "Techno-economic assessment of various hydrogen production methods–A review," *Bioresour. Technol.*, vol. 319, p. 124175, 2021.

[7] S. Kshirsagar and A. B. K. Malladi, "Conventional Pathways for Hydrogen Production." [Online]. Available: https://wri-india.org/blog/conventional-pathways-hydrogen-production

[8] L. Blain, "Record-breaking hydrogen electrolyzer claims 95% efficiency." [Online]. Available: https://newatlas.com/energy/hysata-efficient-hydrogen-electrolysis/

[9] X. Li *et al.*, "Water Splitting: From Electrode to Green Energy System," *Nano-Micro Lett.*, vol. 12, no. 1, p. 131, 2020, doi: 10.1007/s40820-020-00469-3.

[10] B. Aguila *et al.*, "Lower Activation Energy for Catalytic Reactions through Host–Guest Cooperation within Metal–Organic Frameworks," *Angew. Chemie*, vol. 130, no. 32, pp. 10264–10268, 2018, doi: 10.1002/ange.201803081.

[11] D. Bhalothia *et al.*, "Recent Advancements and Future Prospects of Noble Metal-Based Heterogeneous Nanocatalysts for Oxygen Reduction and Hydrogen Evolution Reactions," *Applied Sciences*, vol. 10, no. 21. 2020. doi: 10.3390/app10217708.

[12] J. Huo *et al.*, "Stability of Pd nanoparticles on carbon-coated supports under hydrothermal conditions," *Catal. Sci. Technol.*, vol. 8, no. 4, pp. 1151–1160, 2018, doi: 10.1039/C7CY02098H.

[13] S. Sarkar, S. Patel, and D. Mukherjee, "Materials Today Sustainability Palladium phosphoselenide (PdPSe) – Reduced graphene oxide composite : A tri-functional electrocatalyst and a cathode catalyst for alkaline fuel cells," vol. 25, no. October 2023, 2024.

[14] T.-F. Choo, N. Mat Zali, N. U. Saidin, and K.-Y. Kok, "Gamma Radiolysis-Synthesized Carbon Nanotube–Supported Palladium as Electrocatalyst for Oxygen Reduction Reaction," *Electrocatalysis*, vol. 14, no. 3, pp. 418–428, 2023, doi: 10.1007/s12678-022-00807-6.

[15] B. Bawab *et al.*, "Synergistic effect of Pd single atoms and nanoparticles deposited on carbon supports by ALD boosts alkaline hydrogen evolution reaction," *Chem. Eng. J.*, vol. 482, no. August 2023, 2024, doi: 10.1016/j.cej.2024.148959.

[16] J. Zhang and L. Dai, "Heteroatom-Doped Graphitic Carbon Catalysts for Efficient Electrocatalysis of Oxygen Reduction Reaction," *ACS Catal.*, vol. 5, no. 12, pp. 7244–7253, Dec. 2015, doi: 10.1021/acscatal.5b01563.

[17] B. D. Adams and A. Chen, "The role of palladium in a hydrogen economy," *Mater. Today*, vol. 14, no. 6, pp. 282–289, 2011, doi: https://doi.org/10.1016/S1369-7021(11)70143-2.

[18] Y. Zhou *et al.*, "Decomposition of Supported Pd Hydride Nanoparticles for the Synthesis of Highly Dispersed Metallic Catalyst," *Chem. Mater.*, vol. 30, no. 22, pp. 8116–8120, Nov. 2018, doi: 10.1021/acs.chemmater.8b02192.

[19] M. Guillen-Soler, N. V Vassilyeva, E. P. Quirós-Díez, J. M. Vila-Fungueiriño, A. Forment-Aliaga, and M. del C. Gimenez-Lopez, "A Hierarchical Polyoxometalate/Pd/Mos2 Hybrid: Developing an Efficient Novel Bifunctional Catalyst for Water Splitting," *Adv. Sustain. Syst.*, vol. n/a, no. n/a, p. 2300607, Dec. 2023, doi: https://doi.org/10.1002/adsu.202300607.

[20] A. G. Oshchepkov, G. Braesch, A. Bonnefont, E. R. Savinova, and M. Chatenet, "Recent Advances in the Understanding of Nickel-Based Catalysts for the Oxidation of Hydrogen-Containing Fuels in Alkaline Media," *ACS Catal.*, vol. 10, no. 13, pp. 7043–7068, 2020, doi: 10.1021/acscatal.0c00101.

[21] Y. Fang and Y. Guo, "Copper-based non-precious metal heterogeneous catalysts for environmental remediation," *Cuihua Xuebao/Chinese J. Catal.*, vol. 39, no. 4, pp. 566–582, 2018, doi: 10.1016/S1872-2067(17)62996-6.

[22] B. H. R. Suryanto, Y. Wang, R. K. Hocking, W. Adamson, and C. Zhao, "Overall electrochemical splitting of water at the heterogeneous interface of nickel and iron oxide," *Nat. Commun.*, vol. 10, no. 1, p. 5599, 2019, doi: 10.1038/s41467-019-13415-8.

[23] C. Liang *et al.*, "Synthesis and Catalytic Performance of Pd Nanoparticle/Functionalized CNF Composites by a Two-Step Chemical Vapor Deposition of Pd(allyl)(Cp) Precursor," *Chem. Mater.*, vol. 21, no. 12, pp. 2360–2366, Jun. 2009, doi: 10.1021/cm8031225.

[24] D.-S. Bae, K.-S. Han, and J. H. Adair, "Synthesis and microstructure of Pd/SiO2 nanosized particles by reverse micelle and sol–gel processing," *J. Mater. Chem.*, vol. 12, no. 10, pp. 3117–3120, 2002, doi: 10.1039/B203203C.

[25] A. M. Perez-Coronado, L. Calvo, N. Alonso-Morales, F. Heras, J. J. Rodriguez, and M. A. Gilarranz, "Multiple approaches to control and assess the size of Pd nanoparticles synthesized via water-in-oil microemulsion," *Colloids Surfaces A Physicochem. Eng. Asp.*, vol. 497, pp. 28–34, 2016, doi: https://doi.org/10.1016/j.colsurfa.2016.02.012.

[26] N. Arul Dhas and A. Gedanken, "Sonochemical preparation and properties of nanostructured palladium metallic clusters," *J. Mater. Chem.*, vol. 8, no. 2, pp. 445–450, 1998, doi: 10.1039/A706100E.

[27] Y. Yu, Y. Zhao, T. Huang, and H. Liu, "Microwave-assisted synthesis of palladium nanocubes and nanobars," *Mater. Res. Bull.*, vol. 45, no. 2, pp. 159–164, 2010, doi: https://doi.org/10.1016/j.materresbull.2009.09.028.

[28] A. J. Cowan *et al.*, *Photoelectrochemical Hydrogen Production*, vol. 102, no. 1. in Electronic Materials: Science & Technology, vol. 102. Boston, MA: Springer US, 2012. doi: 10.1007/978-1-4614-1380-6.

[29] C. Larson and J. P. G. Farr, "Current research and potential applications for pulsed current electrodeposition - A review," *Trans. Inst. Met. Finish.*, vol. 90, no. 1, pp. 20–29, 2012, doi: 10.1179/174591912X13238641755178.

[30] M. B. Kale, R. A. Borse, A. Gomaa Abdelkader Mohamed, and Y. Wang, "Electrocatalysts by Electrodeposition: Recent Advances, Synthesis Methods, and Applications in Energy Conversion," *Adv. Funct. Mater.*, vol. 31, no. 25, pp. 1–24, 2021, doi: 10.1002/adfm.202101313.

[31] V. Yarlagadda, G. Lin, P. Y. Chong, and T. Van Nguyen, "High Surface Area Carbon Electrodes for Bromine Reactions in H2-Br2 Fuel Cells," *J. Electrochem. Soc.*, vol. 163, no. 1, p. A5126, 2016, doi: 10.1149/2.0171601jes.

[32] H. E. M. Hussein, H. Amari, B. G. Breeze, R. Beanland, and J. V. MacPherson, "Controlling palladium morphology in electrodeposition from nanoparticles to dendrites: Via the use of mixed solvents," *Nanoscale*, vol. 12, no. 42, pp. 21757–21769, 2020, doi: 10.1039/d0nr05630h.

[33] A. S. Fuentes, A. F. Filippin, and M. del C. Aguirre, "Pd Nucleation and Growth Mechanism Deposited on Different Substrates," *Procedia Mater. Sci.*, vol. 8, pp. 541–550, 2015, doi: 10.1016/j.mspro.2015.04.107.

[34] Y. R. Kim *et al.*, "Nucleation and Aggregative Growth of Palladium Nanoparticles on Carbon Electrodes: Experiment and Kinetic Model," *J. Phys. Chem. C*, vol. 119, no. 30, pp. 17389–17397, 2015, doi: 10.1021/acs.jpcc.5b03513.

[35] S. E. Potts, H. B. Profijt, R. Roelofs, and W. M. M. Kessels, "Room-Temperature ALD of Metal Oxide Thin Films by Energy-Enhanced ALD," *Chem. Vap. Depos.*, vol. 19, no. 4–

6, pp. 125–133, Jun. 2013, doi: https://doi.org/10.1002/cvde.201207033.

[36] J. Y. Feng *et al.*, "Tuning size and coverage of Pd nanoparticles using atomic layer deposition," *Appl. Surf. Sci.*, vol. 539, no. August 2020, 2021, doi: 10.1016/j.apsusc.2020.148238.

[37] S. E. Potts, W. Keuning, E. Langereis, G. Dingemans, M. C. M. van de Sanden, and W. M. M. Kessels, "Low Temperature Plasma-Enhanced Atomic Layer Deposition of Metal Oxide Thin Films," *J. Electrochem. Soc.*, vol. 157, no. 7, p. P66, 2010, doi: 10.1149/1.3428705.

[38] R. W. Johnson, A. Hultqvist, and S. F. Bent, "A brief review of atomic layer deposition: from fundamentals to applications," *Mater. Today*, vol. 17, no. 5, pp. 236–246, 2014, doi: https://doi.org/10.1016/j.mattod.2014.04.026.

[39] S. Sun *et al.*, "Single-atom catalysis using Pt/graphene achieved through atomic layer deposition," *Sci. Rep.*, vol. 3, pp. 1–9, 2013, doi: 10.1038/srep01775.

[40] C. I. Fornari, G. Fornari, P. H. de O. Rappl, E. Abramof, and J. dos S. Travelho, "Monte Carlo Simulation of Epitaxial Growth," M. Zhong, Ed., Rijeka: IntechOpen, 2018, p. Ch. 5. doi: 10.5772/intechopen.70220.

[41] Y. Lei *et al.*, "Synthesis of Pt–Pd Core–Shell Nanostructures by Atomic Layer Deposition: Application in Propane Oxidative Dehydrogenation to Propylene," *Chem. Mater.*, vol. 24, no. 18, pp. 3525–3533, Sep. 2012, doi: 10.1021/cm300080w.

[42] C. Wang, L. Hu, K. Poeppelmeier, P. C. Stair, and L. Marks, "Nucleation and growth process of atomic layer deposition platinum nanoparticles on strontium titanate nanocuboids," *Nanotechnology*, vol. 28, no. 18, p. 185704, 2017, doi: 10.1088/1361-6528/aa688d.

[43] H. B. R. Lee and S. F. Bent, "Microstructure-dependent nucleation in atomic layer deposition of Pt on TiO 2," *Chem. Mater.*, vol. 24, no. 2, pp. 279–286, 2012, doi: 10.1021/cm202764b.

[44] H. Zhang *et al.*, "Pd@Pt Core–Shell Nanostructures with Controllable Composition Synthesized by a Microwave Method and Their Enhanced Electrocatalytic Activity toward Oxygen Reduction and Methanol Oxidation," *J. Phys. Chem. C*, vol. 114, no. 27, pp. 11861–11867, Jul. 2010, doi: 10.1021/jp101243k.

[45] C. Qian, J. Bian, F. Ju, and H. Ling, "Effect of PdSx on Sulfur Resistance of Pd-Based Catalysts for CO Oxidation," *Ind. Eng. Chem. Res.*, vol. 62, no. 6, pp. 3038–3049, Feb. 2023, doi: 10.1021/acs.iecr.2c04098.

[46] L. Liu and A. Corma, "Metal Catalysts for Heterogeneous Catalysis: From Single Atoms to Nanoclusters and Nanoparticles," *Chem. Rev.*, vol. 118, no. 10, pp. 4981–5079, May 2018, doi: 10.1021/acs.chemrev.7b00776.

[47] H. Hu *et al.*, "Stability of single-atom catalysts for electrocatalysis," *J. Mater. Chem. A*, vol. 10, no. 11, pp. 5835–5849, 2022, doi: 10.1039/D1TA08582D.

[48] J. Cai, R. Javed, D. Ye, H. Zhao, and J. Zhang, "Recent progress in noble metal nanocluster and single atom electrocatalysts for the hydrogen evolution reaction," *J. Mater. Chem. A*, vol. 8, no. 43, pp. 22467–22487, 2020, doi: 10.1039/D0TA06942F.

[49] A. Dedieu, "Theoretical Studies in Palladium and Platinum Molecular Chemistry," *Chem. Rev.*, vol. 100, no. 2, pp. 543–600, Feb. 2000, doi: 10.1021/cr980407a.

[50] R. F. W. Bader, "Molecular Orbitals for Homonuclear Diatomics," *Nature*, vol. 433, pp. 848–851, 2005.

[51] I. V Alabugin, S. Bresch, and G. dos Passos Gomes, "Orbital hybridization: a key electronic factor in control of structure and reactivity," *J. Phys. Org. Chem.*, vol. 28, no. 2, pp. 147–162, 2015.

[52] G. Cotton, F.A. and Wilkinson, *Advanced Inorganic Chemistry. 5th Edition*, 5th ed. New York, 1988. [Online]. Available: https://chemistlibrary.files.wordpress.com/2015/05/cotton-wilkinson-advanced-inorganic-chemistry.pdf

[53] C. Nwosu, "An Electronegativity Approach to Catalytic Performance," *J. Tech. Sci. Technol.*, vol. 1, no. 2, pp. 25–28, 2012.

[54] V. A. Matsura *et al.*, "A Quantum-Chemical Study of Dissociation of H2 Molecule on Palladium Clusters," *Russ. J. Gen. Chem.*, vol. 74, no. 7, pp. 975–979, 2004, doi: 10.1023/B:RUGC.0000045849.54881.4f.

[55] W. Dong, V. Ledentu, P. Sautet, A. Eichler, and J. Hafner, "Hydrogen adsorption on palladium: a comparative theoretical study of different surfaces," *Surf. Sci.*, vol. 411, no. 1, pp. 123–136, 1998, doi: https://doi.org/10.1016/S0039-6028(98)00354-9.

[56] S. Hong and T. S. Rahman, "Adsorption and diffusion of hydrogen on Pd(211) and Pd(111): Results from first-principles electronic structure calculations," *Phys. Rev. B*, vol. 75, no. 15, p. 155405, Apr. 2007, doi: 10.1103/PhysRevB.75.155405.

[57] P. Ferrin, S. Kandoi, A. U. Nilekar, and M. Mavrikakis, "Hydrogen adsorption, absorption and diffusion on and in transition metal surfaces: A DFT study," *Surf. Sci.*, vol. 606, no. 7–8, pp. 679–689, 2012.

[58] M. Kauppinen and H. Grönbeck, "Hydrogen Adsorption on Pd – In Intermetallic Surfaces," *Top. Catal.*, vol. 66, no. 17, pp. 1457–1464, 2023, doi: 10.1007/s11244-022-01748-6.

[59] H. Nakatsuji and M. Hada, "Interaction of a hydrogen molecule with palladium," *J. Am. Chem. Soc.*, vol. 107, no. 26, pp. 8264–8266, 1985.

Chapter 2: Anodic TiO_2 nanotube layers decorated by Pd nanoparticles using ALD: An efficient electrocatalyst for methanol oxidation

Published as "Anodic TiO_2 nanotube layers decorated by Pd nanoparticles using ALD: An efficient electrocatalyst for methanol oxidation," B. Bawab, S. M. Thalluri, J. Rodriguez-Pereira, H. Sopha, R. Zazpe, and J. M. Macak, *Electrochimica Acta*, vol. 429, p. 141044, Oct. 2022.

2.1. Abstract

In this chapter, the performance of Pd nanoparticles (NPs) prepared by Atomic Layer Deposition (ALD) as a catalyst for methanol electro-oxidation has been reported. Pd NPs were decorated onto anodic TiO_2 nanotube (TNT) layers as supporting material that possess a large available surface area and direct electrical contact via the underlying titanium foil. Different Pd loadings (150 – 300 – 450 – 600 ALD cycles) show different particles sizes ranging between 7 and 12 nm, as revealed by TEM. Coalescence dominated visibly from 450 ALD cycles, which led to a porous Pd layer all along the TNT walls rather than the growth of individual particles. Electrocatalytic performance was investigated by cyclic voltammetry (CV), where the catalytic activity increased proportional with Pd loading up to the highest values for 400 and 450 cycles, whereas a further increase in the number of ALD cycles (N_{ALD}) did not show any additional improvement in methanol oxidation current densities. TNT layers decorated with 400, 450 and 600 Pd ALD cycles show featureless curves suggesting complete anti-poisoning ability or possibly a proof of a direct conversion from CH_3OH to CO_2 (without any intermediate byproducts). The lack of an oxidation peak during the anodic scan and therefore a reduction peak during the cathodic scan, confirms Pd NPs (stabilized by TiO_2) efficiently utilize OH_{ads} and chemisorbed CH_3OH in a way that its CO poisoning was inhibited. As a result, the tuned high surface area TNT layers exhibited excellent performance as a supporting material for Pd NPs against formation of electrochemical poisoning species. Finally, the mechanism of the TNT layers interaction with Pd NPs, which led to the propelling methanol oxidation reaction without loss in performance over cycling is postulated.

2.2. Introduction

The ever-increasing global energy demand along with the environmental issues, originated from the use of fossil fuel, triggered an intense search for sustainable and clean energy alternatives. Direct methanol fuel cells (DMFCs), in which the chemical energy stored in methanol is converted to electrical energy, have been explored in the last years. Unlike hydrogen fuel cells, DMFCs use liquid fuel that allows easier handling and transportation. The two main reactions that determine the activity of DMFCs are the anodic methanol oxidation reaction (MOR) and cathodic oxygen reduction reaction (ORR) [1]. The catalytic reaction kinetics during the fuel cell activity is dependent on the electrode surface morphology and/or nanoparticles (NPs) sizes. Larger NPs can relatively increase the NPs surface exposed to the surrounding electrolyte as compared to the interacted substrate surface [2]. In contrary, smaller NPs are less likely to have CO poisoning specially at high temperatures, due to oxygen bond break resulting in oxygen desorption at this level, which shows more resistant to CO poisoning [3]. Noble metal-metal oxide–support interactions generally play a significant role in electrocatalysis, as they maintain a high catalytic activity of noble metal NPs due to their tolerance towards poisoning from reaction byproducts. The use of metal oxide supports, such as MnO_2 [4], SnO_2 [5], or TiO_2 [6], proved to be very beneficial as they are highly stable and maintain consistent conversion efficiency in fuel cells. Supporting materials, decorated by NPs as a catalyst, enhance the electron transport at the catalyst/electrolyte interface. The presence of oxide supporting material, whether it is a reducible metal oxide, such as TiO_2 or FeO_x, or a not reducible oxide such as ZrO_2 [7], can directly affect the catalytic activity. For instance, in catalytic converters used in the automotive industry, CO interacts with oxygen on the catalyst surface producing CO_2. Hence, the reaction can proceed in two directions. In case the supporting material provides oxygen, as it happens with TiO_2, these oxygen atoms will substitute the missing oxygen on the surface. Otherwise, CO most likely substitutes oxygen atoms and deactivates the surface [8]. In parallel, approaches based on variations in the electrode morphology (nano-, meso-, and macroporous materials) have shown a huge impact to prevent the development and accumulation of intermediate products on the active electrode surface. In addition, the use

of alkaline electrolytes showed higher catalytic activity towards the anodic regime compared with acidic electrolytes [9]. One must bear in mind that testing noble metals, such as Pd, under intense anodic conditions in alkali medium can result in total deactivation, due to the formation of Pd hydroxylates. Also the electrolyte concentrations can directly affect the MOR rate [10].

Regarding the noble metal NPs used as catalyst towards methanol electro-oxidation, the inherent stability of Pt makes it a great catalyst choice as an anode in DMFCs. However, taking into consideration the Pt scarcity and the corresponding high costs for large scale Pt production, a search for alternative catalysts has been initiated. Alloys of Pt with other noble metals, such as Pd, are considered to be used on DMFCs electrodes in order to reduce or substitute Pt mass. While a complete MOR during the electrochemical process involves the transfer of 6 electrons to have CO_2 as an end-product, incomplete oxidation can result in other undesired products such as formaldehydes, formic acids, and CO [11]. Pd has the tendency to bond with CO molecules, which leads to poisoning of the active surface. Even at lower temperatures, the process can still facilitate CO to react, forming $Pd(CO)_x$ compounds [12]. Hydration reaction that is more predominant on Pd surface as compared to Pt, can later form OH groups that support the de-poisoning of the intermediate “CO” during methanol oxidation [13], as shown later also in this paper.

The importance of having NPs is based on the fact, that it significantly improves the surface to volume ratio, providing more catalytic active sites. The growth of uniform Pd NPs on high specific surface area supporting materials is of paramount importance due to the improved NPs count per unit area of support, thus increasing the catalytic activity of the process. Several reports have reported on the employment of Pd NPs on different substrates [14][15][16]. The available literature shows that the deposition of Pd NPs on TNT layers utilizing different techniques such as electrochemical milling [17], chemical bath deposition [18][19] and electrodeposition [20], suffers from non-uniform depositions with variations in coverage density all along the surface. Some of the published literatures have focused on ALD based deposition of Pd NPs on TNT layers for their applications on organic molecule degradation [2][15][21][22]. Well dispersed Pd NPs over TNT layers were obtained in these papers and their activities for different catalytic

reactions were proposed. However, TNT layers as a standalone are not a good material for the electrocatalytics purposes, knowing its poor electrical conductivity. However, as a supporting material, high surface area TNT layers can be detrimental to facilitate the oxidation of reactant molecules (methanol). This is due to an enormous amount of surface hydroxyl groups that are well known to oxidize intermediate products, majorly CO generated during methanol electrooxidation [23].

In this chapter, the performance of Pd nanoparticles (NPs) prepared by Atomic Layer Deposition (ALD) was reported as a catalyst for methanol electro-oxidation. Pd NPs were decorated onto anodic TiO_2 nanotube (TNT) layers as supporting material that possess a large available surface area and direct electrical contact via the underlying titanium foil. Different Pd loadings (150 – 300 – 450 – 600 ALD cycles) show different particles sizes ranging between 7 and 12 nm, as revealed by transmission electron microscopy. Coalescence dominated visibly from 450 ALD cycles, which led to a porous Pd layer all along the TNT walls rather than the growth of individual particles. Electrocatalytic performance was investigated by cyclic voltammetry (CV), where the catalytic activity increased proportional with Pd loading up to the highest values for 400 and 450 cycles, whereas a further increase in the number of ALD cycles (N_{ALD}) did not show any additional improvement in methanol oxidation current densities. TNT layers decorated with 400, 450 and 600 Pd ALD cycles show featureless curves suggesting complete anti-poisoning ability or possibly a proof of a direct conversion from CH_3OH to CO_2 (without any intermediate byproducts). The lack of an oxidation peak during the anodic scan and a reduction peak during the cathodic scan confirms Pd NPs (stabilized by TiO_2) efficiently utilize OH_{ads} and chemisorbed CH_3OH in a way that its CO poisoning was inhibited. As a result, the tuned high surface area TNT layers exhibited excellent performance as a supporting material for Pd NPs against formation of electrochemical poisoning species. Finally, the mechanism of the TNT layers interaction with Pd NPs, which led to the propelling methanol oxidation reaction without loss in performance over cycling is postulated. The aim is to conformaly decorate TNT layers by homogeneously distributed Pd NPs using ALD and to evaluate their catalytic activity profiles for methanol electro-oxidation. Therefore, the ability of Pd NPs on TNT (Pd/TNT) layer electrodes to withstand against surface poisoning is elaborated. Pd NPs were decorated by ALD onto 5

µm thick anatase TNT layers. The morphology and the chemical composition of the resulting Pd/TNT layers were investigated in detail by scanning electron microscope (SEM), transmission electron microscopy (TEM), X-ray diffraction (XRD), and X-ray photoelectron spectroscopy (XPS). The electrocatalytic activity of Pd/TNT layers towards methanol electro-oxidation was evaluated by cyclic voltammetry (CV) and chronoamperometry (CA) as a function of the number of ALD cycles.

2.3. Experimental part

2.3.1. TNT layer preparation

The detailed protocol for the TNT layer was published in our previous work [24]. Briefly, Ti foils (Sigma-Aldrich, 0.127 mm, 99.7% purity) were degreased and anodized at room temperature using a high-voltage potentiostat (PGU-200 V, IPS Elektroniklabor GmbH) to develop TNT layers of ~5 µm thickness and ~230 nm diameter in an ethylene glycol-based electrolyte containing 10% water and 0.15 M NH_4F at 100 V for 4 hours. Ti foils and TNT layers were annealed in air for 1 h at 400 $^{\circ}$C.

2.3.2. Atomic Layer Deposition of Pd

Pd NPs were deposited onto TNT layers and onto annealed Ti foils using TFS 200 ALD reactor (Beneq) provided with stop-flow configuration. Palladium(II)hexafluoroacetylacetonate $Pd(C_5HF_6O_2)_2$ (95%, Strem Chemicals) and formalin (37% formaldehyde in water with 10–15% of methanol, Sigma-Aldrich) were used as the Pd precursor and co-reactant, respectively. The Pd precursor was heated up to 65 °C, while the deposition process temperature was 200 °C. One ALD cycle (N_{ALD} = 1) was defined by the following sequence: Pd pulse (2 s)-exposure (10 s)-N_2 purge (20 s)-formalin pulse (1 s)-exposure (10 s)-N_2 purge (20 s). A preliminary step to enhance the density of hydroxyl functional groups on the surface substrate was applied to improve the Pd nucleation. Such preliminary step consisted of 5 ALD cycles (water pulse (0.5 s)-exposure (10 s)-N_2 purge (20 s)) followed by 20 cycles (Pd (0.25 s)-exposure (10 s)-N_2 purge (20 s)) was employed with pulse, exposure, and purge durations programmed as “5 * (0.5:10:20 s) and 20 * (0.25:10:20 s)” for H_2O and Pd precursor respectively prior to

the actual deposition of Pd. The sole necessity of H_2O pulse is to create -OH functional groups on the substrate so that Pd can nucleate efficiently.

2.3.3. Characterization methods

Blank and Pd decorated TNTs (Pd/TNTs) and Pd/Ti foils were characterized by scanning electron microscope (SEM) FEI Verios 460L. Pd/TNTs were also characterized by an high-resolution transmission electron microscope (HRTEM) Thermo Fisher Scientific Titan Themis 60-300, operated at 300 kV and equipped with a C_s image aberration corrector, a high angle annular dark field detector for scanning transmission electron microscopy (STEM-HAADF) imaging, and Super-X energy dispersive X-ray (EDX) spectrometer with four 30 mm^2 windowless detectors for STEM-EDX analysis to check the morphology and Pd NPs size/distribution. The crystalline structure of Pd/TNT layers was assessed using X-ray diffraction XRD (Rigaku Smartlab 3 kW diffractometer equipped with Cu-Kα1 radiation source). Surface chemical state of Pd NPs before and after electrochemical measurements were studied using X-ray photoelectron spectroscopy (XPS) Kratos Analytical Axis Supra instrument, with Al-Kα monochromatic X ray source (hν = 1486.69 eV). The spectra were deconvoluted using the CasaXPS software and referenced to the Femi Level cut off, which means is at 0 eV on the binding energy scale. Pd 3d spectra were deconvoluted with asymmetric Lorentzian function LA (1.5, 4, 45) for metallic state (Pd^0), mixed Gaussian-Lorentzian functions GL (30) for Pd oxides or hydroxides and Pd plasmon loss.

2.3.4. Electrochemical analysis

The electrochemical measurements were carried out in a normal three electrodes electrochemical cell at room temperature. Autolab VIONIC potentiostat supported by INTELLO software was used for this purpose. Two solutions of 1M KOH and 1M KOH/CH_3OH were used as electrolytes. The reference electrode was Ag/AgCl 3M KCl (E = 0.210 V vs RHE). A Pt foil was used as counter electrode, where Pd decorated Ti foils (Pd/Ti) and Pd/TNT layers were used as working electrodes. Before every measurement, degassing of all electrolytes was carried out by bubbling with ultra-high purity nitrogen for at least 15 minutes, this to ensure the removal of the dissolved

unwanted oxygen that can interfere during the electrochemical oxidation process. All potentials given in this paper were recalculated versus RHE. Cyclic voltammetric (CV) measurements were carried at a scanning rate of 10 mV s^{-1}. Electrochemical impedance spectroscopy (EIS) was conducted using the same setup as above, using methanolic KOH as a solution at 0.8 V vs. RHE. In order to check and compare the stability of various Pd/TNT layers and Pd/Ti foils, chronoamperometric (CA) measurements were performed at an applied potential of 0.9 V vs RHE for 2 hours. The geometrical surface area (0.636 cm^2) was used to determine the current densities. In addition, the electrochemical active surface area (ECSA) has been determined and compared with the literature results.

2.4. Results and discussion

2.4.1. Structural characterization

The scanning electron microscope (SEM) images depicted in **Figure 2.1** offer a visual representation of TNT layers, each 5 µm thick with an inner diameter of approximately 250 nm. These layers were decorated with Pd NPs through varying cycles of Pd ALD, ranging from 0 to 600 cycles. Notably, the images confirm a homogeneous distribution of Pd NPs across both the inner and outer walls of the TNT layers. As one can expect, an increase in the N_{ALD} results in a higher density of Pd NPs on the TNT layer surface. Starting from N_{ALD} of 450 cycles, Pd nanoparticles begin to coalesce, resulting in a porous Pd layer, as shown in **Figure 2.1d**.

Figure 2.A.1[*], displaying SEM images of the oxidized titanium foils decorated with Pd NPs using analogous Pd ALD cycles (N_{ALD}): 0, 150, 300, 350, 400, 450 and 600, presents an intriguing contrast. Here, the Pd NPs exhibit coalescence at 300 cycles, a notably earlier occurrence compared to the TNT layers. This disparity can be attributed to the distinct nucleation density offered by the TNT layers along with their significantly higher surface area, accommodating a higher Pd loading. Consequently, the comparative analysis of NP size from Pd/Ti becomes challenging due to the premature coalescence observed in this context. Additionally, the thickness of these specimens poses a limitation

[*] Appendix data can be found at the end of this chapter, page 48.

on TEM analysis, as the specimens are impervious to electrons, inhibiting detailed structural characterization.

The elemental composition analysis through energy-dispersive X-ray spectroscopy (EDX) provides valuable insights into the weight percentage (wt %) distribution of C, Ti, O, and Pd. **Figure 2.A.2** elucidates a direct correlation between the Pd content on Pd/TNT layers and the increasing number of Pd ALD cycles. Concurrently, the EDX spectra illustrated in **Figure 2.A.3** approve the increasing Pd along with increasing N_{ALD}.

The morphological features of Pd/TNT layers were further characterized by HRTEM and compared with the non-decorated Pd layer (0 N_{ALD}). HRTEM images in **Figure 2.2** provide an overview of the size and distribution of Pd NPs on TNTs. The Pd NPs were uniformly distributed all along the walls of TNT layers. As mentioned above, Pd NPs coalescence started from 450 ALD cycles (**Figure 2.2d**). Regarding the Pd NPs size dependency with the number of ALD cycles, **Figure 2.2f** shows the average Pd NPs size for each sample with different number of ALD cycles, determined using the statistical analyses from TEM images. The average sizes of Pd NPs at 150, 300, and 450 ALD cycles measured 7.5, 10.5, and 12.5 nm, respectively. Notably, a higher ALD cycle count (600) indicates further coalescence of Pd NPs, initiating the formation of a porous Pd layer along the TNT walls.

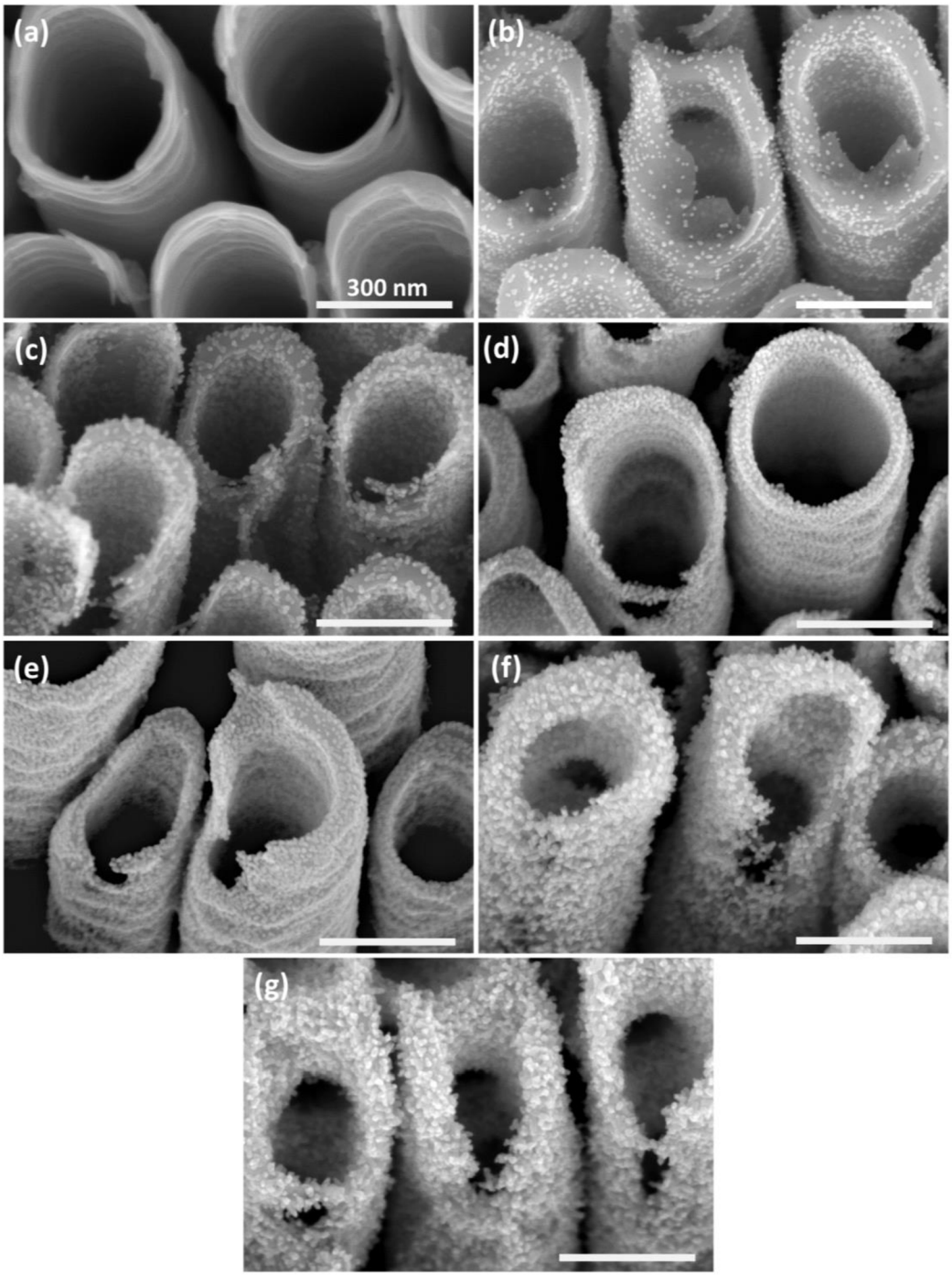

Figure 2.1. *SEM top views of 5 µm thick TNT layers decorated with Pd NPs using different* N_{ALD}*: (a) 0, (b) 150, (c) 300, (d) 350, (e) 400, (f) 450, (g) 600. The scale bars in all images represent 300 nm.*

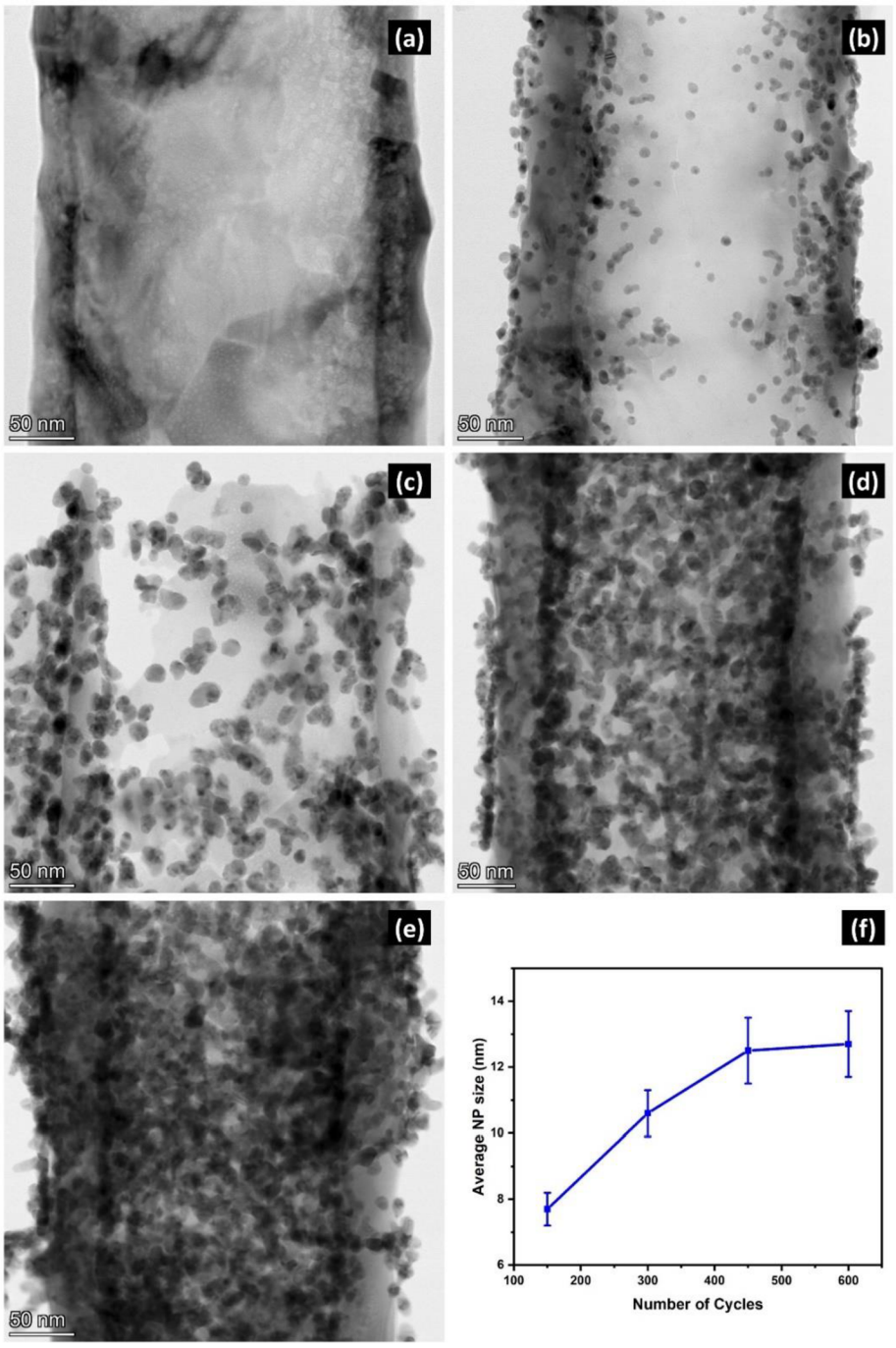

Figure 2.2. *TEM images of single TNT with Pd NPs grown after 0 (a), 150 (b), 300 (c), 450 (d), and 600 (e) Pd N_{ALD}, respectively. (f) Average NPs size as function of N_{ALD} (for the same samples as in a) to e)).*

The XRD patterns, as illustrated in **Figure 2.3a**, offer crucial insights into the structural characteristics of the pristine titanium nanotube (TNT) layer. The distinct peaks observed are representative of the anatase TiO_2 phase, with prominent peaks registered at 25.2° and 48°, corresponding to the (101) and (200) anatase peaks, respectively. Additionally, supplementary peaks identified at 38.4° and 40.2° signify the crystalline planes of Ti substrate, specifically the (002) and (101) planes. The introduction of palladium (Pd) by atomic layer deposition (ALD) onto the TNT layers results in noticeable changes in the XRD patterns, particularly in the higher Pd loading (450 and 600 N_{ALD}). The expected appearance of the (111) Pd plane diffraction peak at 40.1° is obscured by the overlap with the Ti (101) peak, making it difficult to distinguish. Closer examination of the 40.1° peak in the 600 ALD cycle sample reveals a broadening of the peak with reduced intensity. This broadening, which is relatively different from other peaks, indicates the reduction in size of the Pd nanoparticle crystals. Another significant observation is the appearance of a broad peak around 46.2°, attributed to the Pd (200) plane, which is clearly visible only in TNT layers decorated with 450 and 600 Pd N_{ALD} cycles. This appearance correlates with the formation of a porous Pd structure, which is different from samples deposited with lower Pd ALD cycles (150 and 300). In the latter, the dispersed nature of the Pd nanoparticles within the TNT walls hinders their detection by X-ray diffraction.

Figure 2.3b show high resolution Pd, Pd 3d XPS spectra obtained before and after the CA. Both spectra show the corresponding spin-orbit splitting Pd $3d_{5/2}$ / Pd $3d_{3/2}$ with similar shapes. Seven components were used to deconvolute both spectra; six associated to the spin-orbit splitting, which correspond to three different chemical species, and the leftover for the characteristic plasmon loss that appears as Pd is mostly metallic. The first doublet (red peaks) are centered at 335.3 / 340.6 eV confirming the presence of metallic Pd (Pd^0) [25]. The binding energies corresponding to the second doublet (blue peaks) at 336.9 / 340.5 eV, were related to Pd^{2+} [26], while those from the third doublet (green peaks), located at 338.7 / 344.0 eV were assigned to Pd^{4+} [27]. Pd^{2+} and Pd^{4+} could be related to corresponding oxides or hydroxides [28][29]. Since no major differences were found from chemical species and/or binding energies shifts in Pd spectra before and after the electrochemical measurements, quantification of the oxidation states was performed, as shown in **Figure 2.3c**. According to these results, it is evident that after CA

measurements the amount of metallic Pd decreases slightly (around 4.3%), while the content of Pd^{2+} increases.

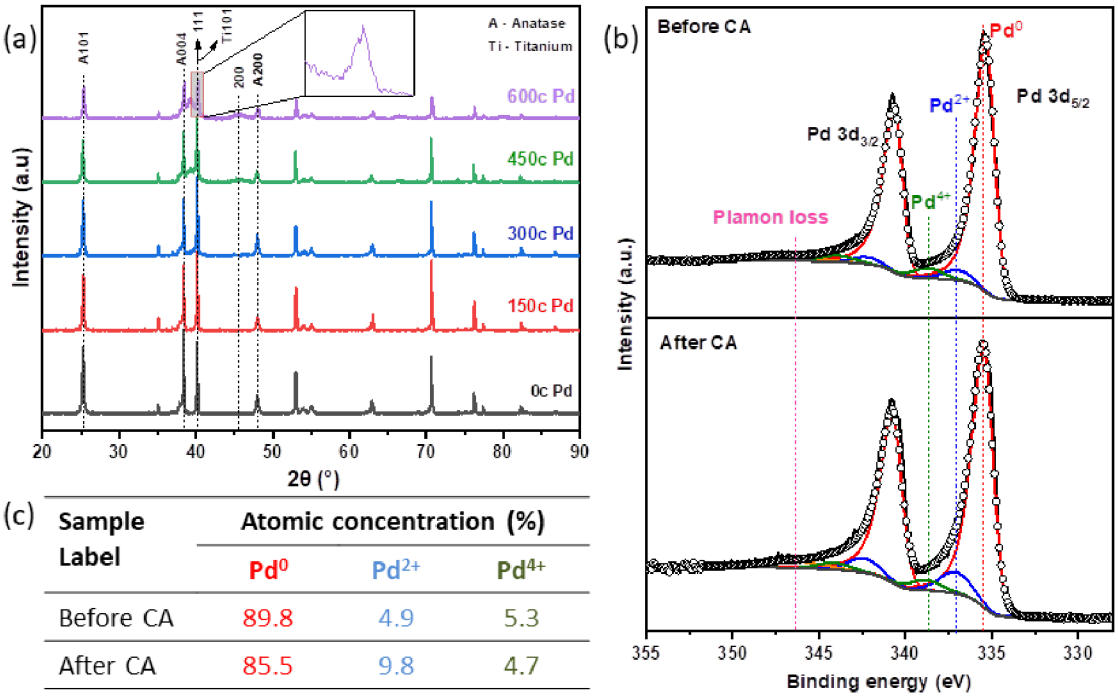

(c)

Sample Label	Atomic concentration (%)		
	Pd^0	Pd^{2+}	Pd^{4+}
Before CA	89.8	4.9	5.3
After CA	85.5	9.8	4.7

Figure 2.3. *a) XRD patterns of 5 µm thick Pd/TNT layers decorated with N_{ALD} = 0, 150, 300, 450, and 600 Pd. b) Pd 3d XPS high resolution spectra of 600c Pd/TNT layers before and after chronoamperometric (CA) measurements. c) Atomic concentration of Pd obtained from the fitted XPS spectra.*

2.4.2. Electrochemical activity

Figure 2.4a exhibits the electrocatalytic activity profile of Pd/Ti foils in electrolyte of 1 M KOH solution. The blank foil shows no response along the CV in the potential range (0 to 1.2 V), indicating no oxidation reaction occurs. Increasing Pd N_{ALD} from 150 to 600 enhanced the current density at lower potentials, showing sharp peak at around 0.1 V. This peak represents the desorption of H on the Pd NPs surface due to the electrolyte (1M KOH) enriched with dissociated hydroxyl groups. While it is well known that the Pd surface gets gradually oxidized as the anodic scan moves towards higher potential region for E > 0.7 V [30], the reverse scan shows a reduction peak at around 0.7 V representing

the desorption of oxygen (reduction of PdO to Pd), adsorbed during the previous forward scan between 0.75 and 1.2 V. **Figure 2.4b** depicts the CVs obtained from the set of Pd/Ti foils tested in 1 M KOH/CH_3OH. Noticeable oxidation peaks appear starting from Ti foils decorated with 300 Pd N_{ALD}. The results also indicate that increasing Pd N_{ALD} deposited on Ti foils leads to an increase in the methanol oxidation peak current density, and therefore in the cathodic scan the CO oxidation peak current density. The highest current density value of 8.9 mA cm^{-2} corresponds to the Ti foils decorated with 450 Pd N_{ALD}, while those decorated with 300 and 600 Pd N_{ALD} show comparatively lower values of 5.8 and 7.8 mA cm^{-2} at ~0.8 V (noted from the third CV cycle).

The electrocatalytic activity of Pd NPs on Ti foils in methanolic KOH electrolyte shown in **Figure 2.4b** follows the trend of anodic oxidation of MeOH and cathodic oxidation of CO [31]. The obtained CV scans are explained by the fact that during the anodic scan, the sample surface is being activated within a certain potential range, after which it becomes deactivated by oxide species (such as CO), attached on Pd NPs surface preventing further electro-oxidation of methanol. Oxidation reaction initiates at around 0.7 V and the resulting current density increases to reach the electro-oxidation limit at 0.8 V. At this point (0.8 V), the catalytic active sites of Pd NPs surface were poisoned due to adsorption of CO intermediate formed during methanol oxidation, decreasing the current density until the surface is completely inactivated. However, reactivation of the Pd NPs surface occurs during the reverse cathodic scan within a potential value ranging between 0.7 and 0.6 V, due to oxidation of the adsorbed CO molecules (to CO_2) and reduction of PdO to metallic Pd.

The metallic Pd and Pd hydroxides are responsible for the increase in the current density among samples of Pd/Ti foils. Along the potential increase in the anodic scan the number of neighboring OH groups on Pd also increases. Thus, such increment of OH groups at higher potentials facilitates an additive effect on the removal of the CO molecules, adsorbed during the anodic scan.

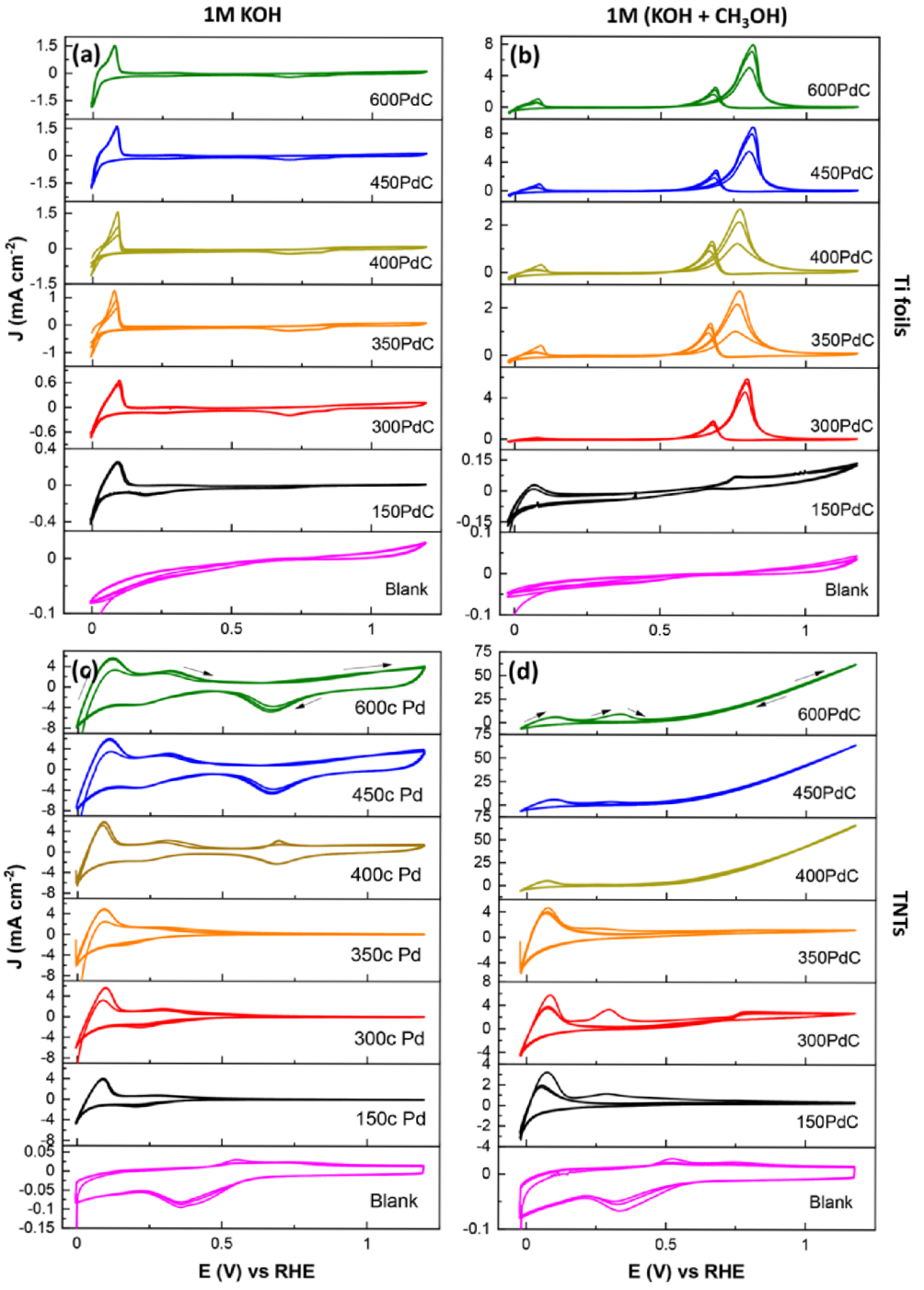

Figure 2.4. *CV curves of three consecutive cycles for Pd/Ti foils (a, b) and Pd/TNT layers (c, d) decorated with different N_{ALD} (0, 150, 300, 350, 400, 450, and 600), recorded in 1 M KOH (a, c) and methanolic (1 M KOH + 1 M CH_3OH) electrolyte by applying a scanning rate of 10 mV s^{-1}.*

Figure 2.4c-d shows the electrocatalytic performance obtained from Pd/TNT layers, which behaves differently from Pd/Ti foils, when it comes to MOR. TNT layers tested in non-methanolic electrolyte (**Figure 2.4c**) show similar peaks compared with Ti foils. Such that in the oxygen adsorption range (0.7 – 1.2 V), Pd-OH, PdO, and/or PdO_x could be formed, while a desorption reduction peak is more pronounced in Pd/TNT layer decorated with 400, 450 and 600 Pd N_{ALD} compared with Ti foils due to higher Pd loadings. Furthermore, **Figure 2.4d** shows Pd/TNT layers performance in methanolic KOH, showing current densities of 66.7, 64.8 and 62.6 mA cm^{-2} obtained at 1.2 V for 400, 450 and 600 Pd N_{ALD} respectively. The CVs show no visible anodic and cathodic peaks, thus representing a featureless polarization curve with an onset potential of 0.5 V. The TNT layer is an oxyphilic oxygen atoms provider. It appears to be an effective oxidizer to mitigate electro-oxidation of methanol on the Pd/TNT layer surface, circumventing either CO poisoning of Pd NPs surface or avoiding formation of intermediate organic species. [8, 23, 32]

2.4.3. Poisoning/de-poisoning mechanism

During the electrode deactivation, observed for Pd/Ti foils, CO species, in addition to other intermediates formed during the process of methanol electro-oxidation, are believed to be the main electrode poisoning species. As a matter of fact, based on the previous literature [32] CO is not the only source of poisoning the catalyst surface, and removal of CO is a diffusion controlled process, which explains the slow desorption process. The oxidation of CO_{ads} is considered as the rate determining step according to the following reaction, and it is well known that the complete MOR can yield CO_2 as end product:

$$CH_3OH_{ads} + 4OH^- \rightarrow CO_{ads} + 4H_2O + 4e^- \quad \text{Eq. 1}$$

$$CO_{ads} + 2OH^- \rightarrow CO_2 + H_2O + 2e^- \quad \text{Eq. 2}$$

In a typical anodic scan of MOR (**Figure 2.4b**) the oxidation starts and carries on until a certain potential where the adsorbed OH groups can no longer react with the available CO molecules adsorbed on the surface (CO_{ads}), leading to a current density drop. CO and OH groups are believed to be evolving during the same potential window. However, the

effect of higher potential excels the activity of OH groups. To simplify, CO bonding on the surface can only lead to a loss of surface activity as explained before and shown in (**Figure 2.4b**), while the CO oxidation reaction occurring with the neighboring OH groups, bonded into the surface of high surface area TNTs, plays an important role in clearing CO molecules and the other adsorbed species.

The obtained featureless curves (**Figure 2.4d**) show no decline in the current density during consecutive CVs within the applied potential range (0 to 1.2 V). In order to study such effect, the potential range is split into two parts. A lower potential region below the peak potential value around 0.8 V (**Figure 2.4b**), and a higher region above this value. At the lower potential region, adsorption of CH_3OH takes place, and Eq. 1 applies resulting in CO adsorbed on the surface. Following, Eq. 2 applies at higher potential, supported by the oxophilic nature of TiO_2 and its electron donor properties, which enhance the CO_{ads} oxidation kinetics enough to keep the CH_3OH oxidation without surface blockage by intermediates. Thus, CO_{ads} oxidation reaction is not considered as the rate determining step anymore with the Pd/TNT layers.

The electrochemical surface area (ECSA) was determined using the integrated reduction peak of PdO. The value of charge for the reduction of a PdO monolayer was taken from the literature [33][34] with $Q_M = 424\ \mu C\ cm^{-2}$ For each electron in a Pd atom, it requires around 210 $\mu C\ cm^2$ as a charge to reduce one PdO layer. The reduction of PdO monolayer involves two electrons per Pd atom. The ECSA value was determined using the following formula.

$$ECSA = \frac{Q_{int}}{Q_M}$$

Since the value of Q_{int} is scan rate dependent, it is correct to use different scan rates for determining the final value of charge integrated from the reduction peak.

The ECSA of Pd/TNT layers decorated with 450 Pd and 600 Pd N_{ALD} were calculated to be 176 cm^2 and 213 cm^2, far higher as compared to 0.636 cm^2 obtained as the corresponding geometrical area (defined as the dimensional area exposed to the electrolyte, without taking the surface porosity into consideration). The ECSA value

obtained for the TNT layer decorated with 600 Pd N_{ALD} is about 7 times larger than the ECSA values reported in the literature, which were estimated to be 22.3, 29.6, and 7.1 cm^2 for Pd/TNT layers (500, 700, and 900 Pd N_{ALD}) [2], and 14.2 cm^2 for palladium supported TiO_2 nanotube array (Pd-TNTA) developed by electrochemical milling and faceting (ECMF) method [17].

Electrochemical impedance spectroscopy (EIS) was used as a powerful tool to study the electron-transfer kinetics of the methanol oxidation reaction. EIS measurements were carried out at a frequency range (10^{-2} and 10^5 Hz), and an AC amplitude of 10 mV at a potential value of 0.8 V vs RHE. In general, the charge transfer resistance value is represented by the diameter of the semicircle. A smaller diameter corresponds to a smaller charge transfer resistance, which in turn represents a high charge transfer rate provided the evaluation performed for all the samples at the same potential**. Figure 2.5** represents the Nyquist plots for Pd/TNT layers decorated with different N_{ALD} of Pd. The Nyquist plots for Ti foils and a comparative assessment of charge transfer resistance values for both foils and TNTs with Pd are provided in **Figure 2.A.4-5**. The decrease in charge transfer resistance for TNTs decorated with N_{ALD} Pd is evident and no significant difference among samples with 400, 450 and 600 N_{ALD} was observed, which aligns with observed current densities from CV for the samples.

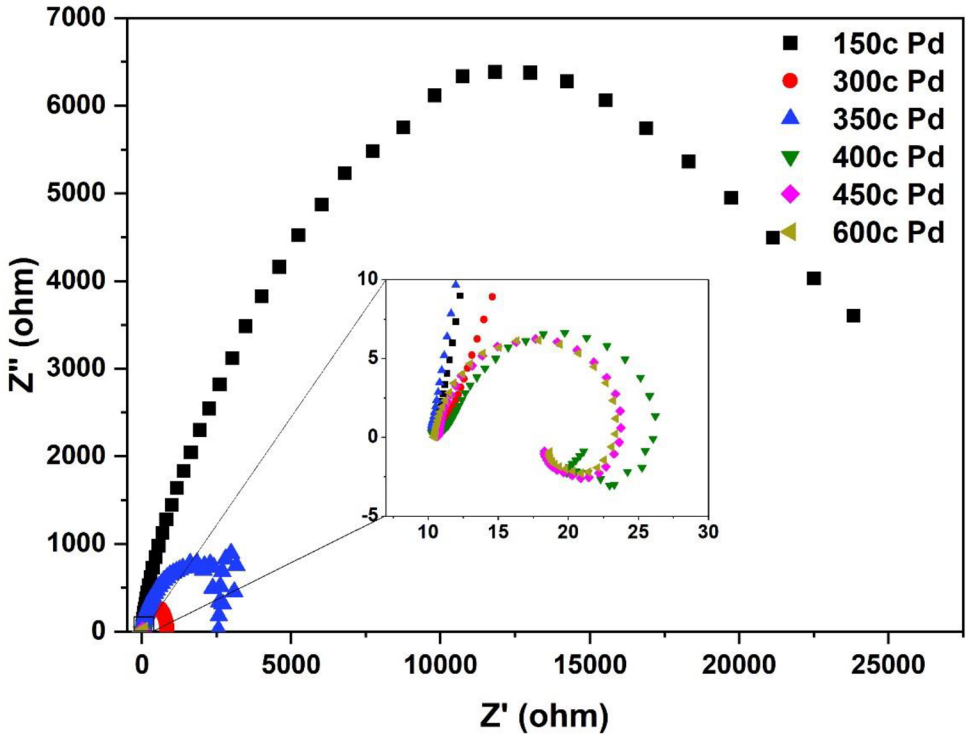

Figure 2.5. *EIS Nyquist plots for Pd/TNT layers using different* N_{ALD}.

In order to evaluate the stability of Pd NPs in 1M KOH electrolyte within the potential range of 0 – 1.4V, 22 consecutive CV cycles were performed for TNTs decorated with Pd NPs using N_{ALD} = 600, as shown in **Figure 2.6**. The resulting CV curves showed several meaningful regions in the anodic as well as in the cathodic scan, as described ahead. The lower potential (region 1) corresponds to hydrogen desorption or adsorption in addition to K^+ cation species [35]. This process takes place as a result of a previous adsorption process happened during the reverse scan at potential ranges between (0 – 0.2V). The peak intensity increase with cycling could be due to accumulation of the adsorbed species at the surface during cycling. In (region 2), the lower current density corresponds to the double layer charge, but the current density increases upon cycling. It is shown in ref [36] that it is unlikely that the rise of the anodic peak during cycling is related to oxide formation. At the same time, the decrease in oxygen adsorption current density (region 3) may indicate the lower quantities of the adsorbed OH groups on the surface and PdO could be formed alternatively. The detailed oxidation process is not yet fully understood.

The formed OH groups react with monoxides obtained during dehydrogenation process leading to a complete reaction. Then the slight increase in current density of the sharp cathodic peak (region 4) represents the reduction of PdO into Pd, where the intensity increases with increasing the palladium oxide on surface.

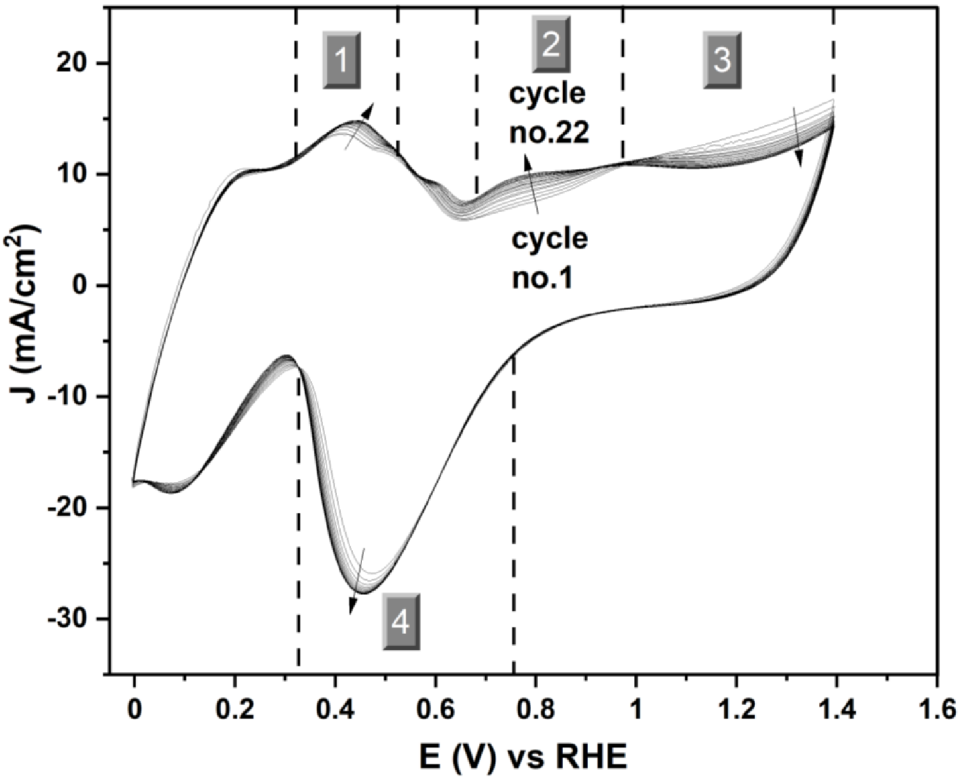

Figure 2.6. *CV curves (22 consecutive cycles) obtained in 1M KOH for 5µm TNTs decorated with Pd NPs using* N_{ALD} *= 600.*

2.4.4. Electrode stability

In order to exploit the stability of Pd NPs on TNTs in 1M KOH + 1M CH_3OH electrolyte, 22 consecutive CV cycles were performed for TNTs decorated with Pd NPs using N_{ALD} = 450, within the potential range of 0 – 1.2V. The resulting CV curves shown in **Figure 2.A.7** prove very good stability of the sample tested.

In order to gain a further insight into the stability of the Pd/Ti foils and Pd/TNT layers´ electrocatalyst, chronoamperometric (CA) measurements were carried out for 2 hours at 0.9 V. CA curves obtained for Pd/TNT layers are shown in **Figure 2.7**. CA curves for

Pd/Ti foils are shown in **Figure 2.A.6**. Pd/Ti foils show a drastic decrease in the current densities during the CA analysis confirming the effect of CO poisoning that led to a loss of active sites responsible for methanol electro-oxidation. Whereas the results obtained from Pd/TNT layers confirm the benefits of noble metal - metal oxide support interaction, by providing significantly higher tolerance to CO poisoning. The CA results depict relatively stable current densities along the CA test for the Pd/TNT layers decorated with 600 Pd N_{ALD}, developing a current density of 28.5 mA cm^{-2} (**Figure 2.7**). In contrast, the Pd/TNT layers decorated with 450, 400, 350, 300, and 150 Pd N_{ALD} show comparatively a higher current density drop (compared to the initial current density) after 2h test, with current densities of 24.8, 16.7, 0.5, 1.07, and 0.07 mA cm^{-2}, respectively. Interestingly, the drop in current densities was attenuated for a higher Pd N_{ALD}. Thus, the percentages of current density loss were 16.1%, 23.7%, 32.1%, 42.8%, 49%, and 75.8% for 600, 450, 400, 350, 300 and 150Pd N_{ALD}, respectively. Therefore, the results indicate that the Pd NPs size plays a significant role in the electrocatalytic performance. Thus, the dominance of the OH coverage on small Pd NPs will decrease the catalytic active Pd surface responsible for methanol adsorption, leading to a higher drop in the current densities under long term performance [37]. Hence, based on the results obtained in this work, it is suggested that the drop in current densities is in relation to the size of Pd NPs deposited onto TNT layers for different N_{ALD}, where the current density stability follows this trend: 600 > 450 > 400 > 350 > 300 > 150c. It is worth clarifying that the current drop in the same plot can be separated into two parts. The fast drop during the first few seconds is related to electron accumulation when the circuit is closed. Following, as the potential is triggered, the high current recorded just after t = 0 s is due to the trapped electrons at the surface, while, as mentioned above, the later current density decrease is ascribed to decrease in metallic Pd content produced by a gradual oxidation of metallic Pd to PdO (Pd^{2+}) as noted in the table of **Figure 2.3c**. In the next period, the current densities are much more stable. In addition to the ability of Pd/TNT layers to stand against poisoning, the obtained current densities show decent records, when compared with other literatures – for comparison see **Table 2.1**.

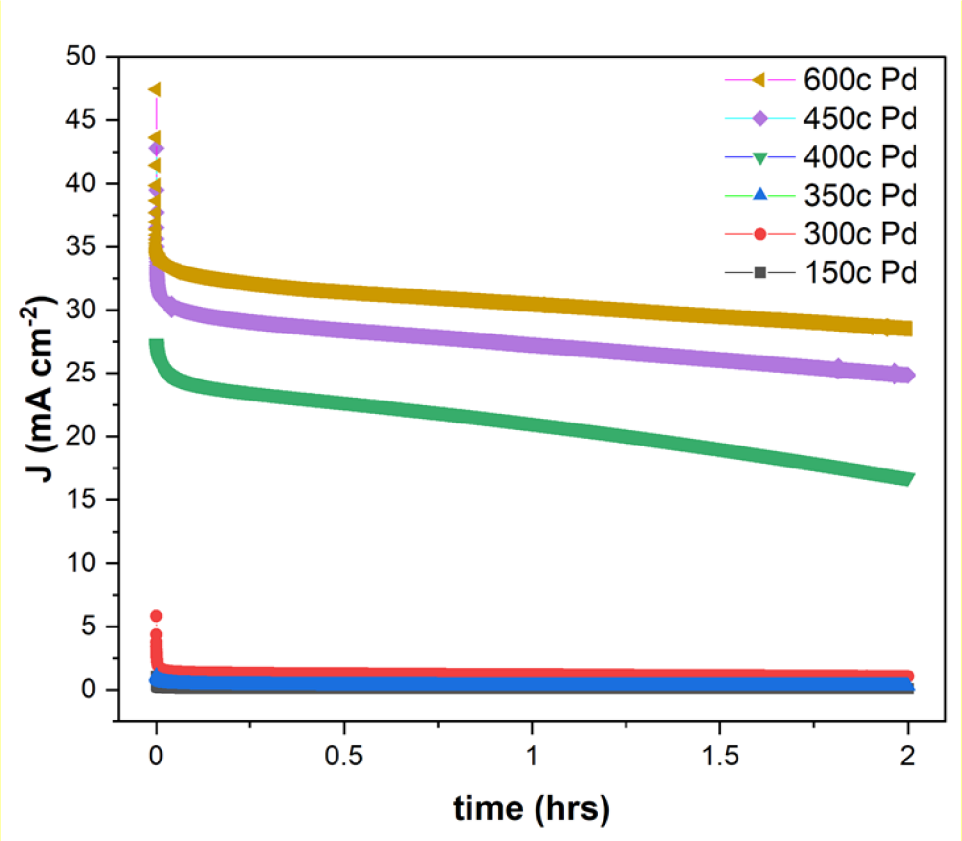

Figure 2.7. *Chronoamperometric (CA) curves demonstrating the stability of Pd/TNT layers with different* N_{ALD} *(150, 300, 350, 400, 450, and 600). CA curves were recorded in 1M KOH + 1M* CH_3OH *at 0.9*V_{RHE} *for 2 h.*

To confirm the stability of the Pd loaded TNTs, the surface chemical state of TNT layers decorated with 600 Pd N_{ALD} was further investigated after the electrochemical measurements by the wide survey spectra (**Figure 2.A.8a**). In both cases (before and after electrochemical measurements), the spectra reveal the presence of C, O, Ti, F and Pd. The C signal comes from the adventitious carbon. The presence of oxygen can be identified from the Auger O KLL signal, since the O 1s has a strong overlapping with the Pd $3p_{3/2}$ signal. Ti peaks are due to the substrate (TNT layers), while F is a remnant from the Ti foil anodization process. In order to verify the chemical nature of TiO_2 after the ALD process, additional high resolution XPS analysis was conducted for Pd/TNTs sample produced with 600c of Pd ALD process (i.e. before any electrochemical experiment). This sample spent the longest time in the ALD reductive atmosphere. shows

The Ti 2p high resolution spectrum of the corresponding sample was shown in **Figure 2.A.8b**. The spectrum reveals only the Ti^{4+} state, since Ti $2p_{3/2}$ is at ~459 eV. Thus, it is clear that no reduction of Ti^{4+} to Ti^{3+} occurred during the ALD process.

Table 2.1. *Overview of current densities obtained from the published literature and compared with density acquired in this work. All values determined or calculated at 0.9V vs RHE, if not denoted otherwise.*

		From CV			From CA	
	Substrate	**Scan rate mV s^{-1}**	**Current density (mA cm^{-2})**	**Onset potential**	**Area considered from current density (mA cm^{-2})@time@ V**	**Ref.**
Ethanol oxidation	SnO_2/Pd 500 cycles	25	1.19 ECSA	-0.465	(ECSA) 0.4 @0s 0.19 @3500s	[38]
	TiO_2 TNTs/Pd 500 cycles	25	0.63 ECSA	-0.465	(ECSA) 0.2375 @0s 0.175 @3500s	[2]
	Pd/TiO_2C	50	18	0.424	Chronopotentiometric 3mA cm^{-2} @0s@0.57V 3mA cm^{-2} @28800s@ 0.72V	[19]
Methanol oxidation	Smooth Pt electrode	50	3.84×10^{-9} A	0.5	NA	[39]
	Pd/C	20	3.1	0.6	NA	[30]
	PdRh/C	20	5	0.6	NA	
	Pd/TiO_2 NTs in H_2SO_4	50	8.66 A	0.436	NA	[40]
	60-65% porous Pd	25	710	0.15	NA	[10]

	Pd/TiO_2-C	50	2.24 (ECSA)	0.44	(ECSA) 1.83 @7200s	[41]
	TiO_2/Pd 450 cycles	10	32	~0.5	(Geometric) 24.8 @7200sec @0.9V	**This work**

2.5. Conclusion

ALD is an effective method to load NP of Pd on high aspect ratio substrates. Thus, it was used to decorate TNT layer by Pd NPs using different number of ALD cycles. The mechanism of methanol electrochemical oxidation was successfully assessed using CV and extended potentiostatic measurements. The formation of featureless curves represents an innovation in bypassing the poisoning effects of methanol electro-oxidation intermediates. The advantage of this process can be claimed to the presence of TiO_2, an oxophilic supporting material for Pd NPs, which effectively promote a complete conversion of CH_3OH to CO_2. In addition to the supporting effect of the TiO_2 nanotube substrate, NPs size proved to show an important effect against surface deactivation, where increasing the NPs size from 7.5 to 12.5 nm (towards porous Pd layer) show much lower loss in current. Notably, XPS analysis for 600c Pd provided significant evidence about the Pd oxidation state after chronoamperometric measurements, obtained as 85.5% in metallic form of Pd^0, which slightly lower value compared to before CA. Such that, the decrease in metallic Pd content (oxidized to Pd^{2+}) can stand as the main reason of activity loss during MOR, where no clear poisoning occurred as an effect of adsorbed carbonyl groups on the surface of Pd NPs.

2.A. Appendix:

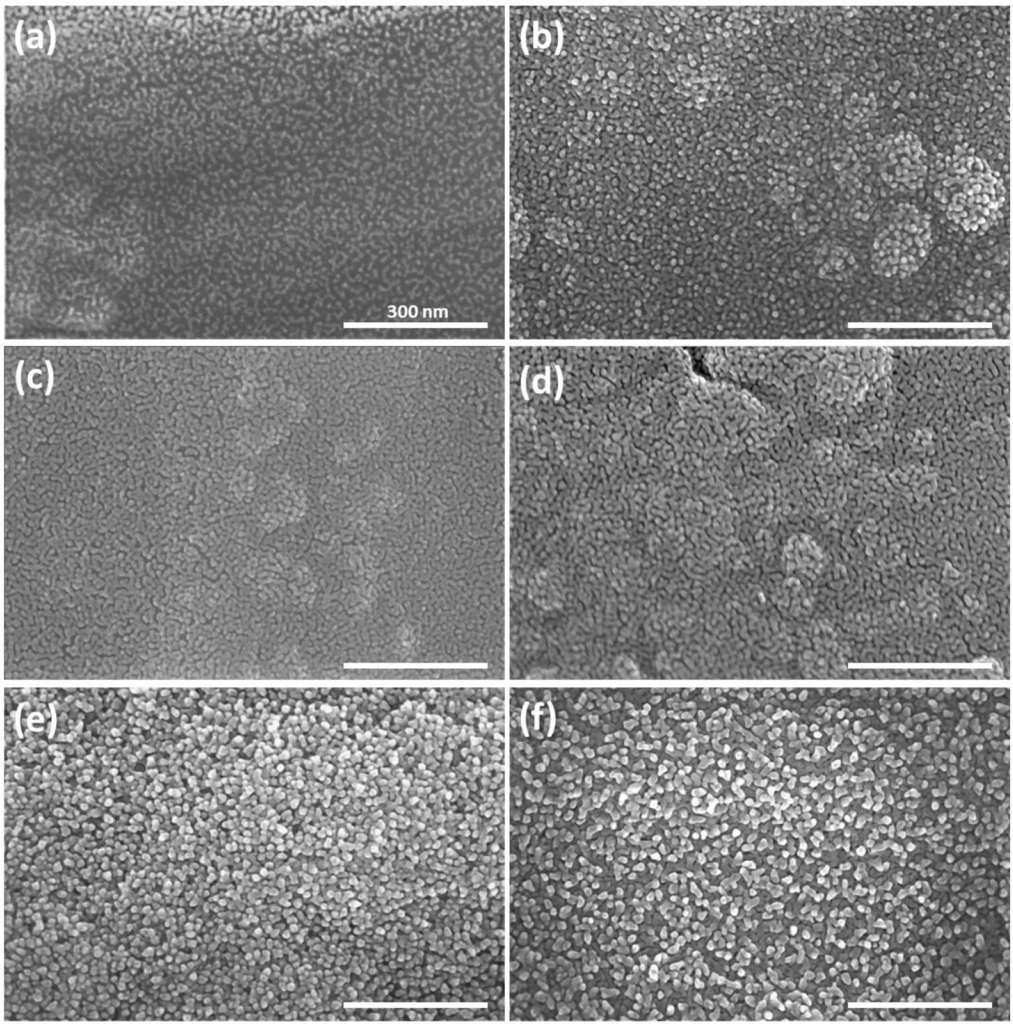

Figure 2.A.1. *SEM of Ti substrates decorated with Pd NPs using different* N_{ALD}*: (a) 150, (b) 300, (c) 350, (d) 400, (e) 450 and (f) 600. The scale bars in all images represent 300 nm.*

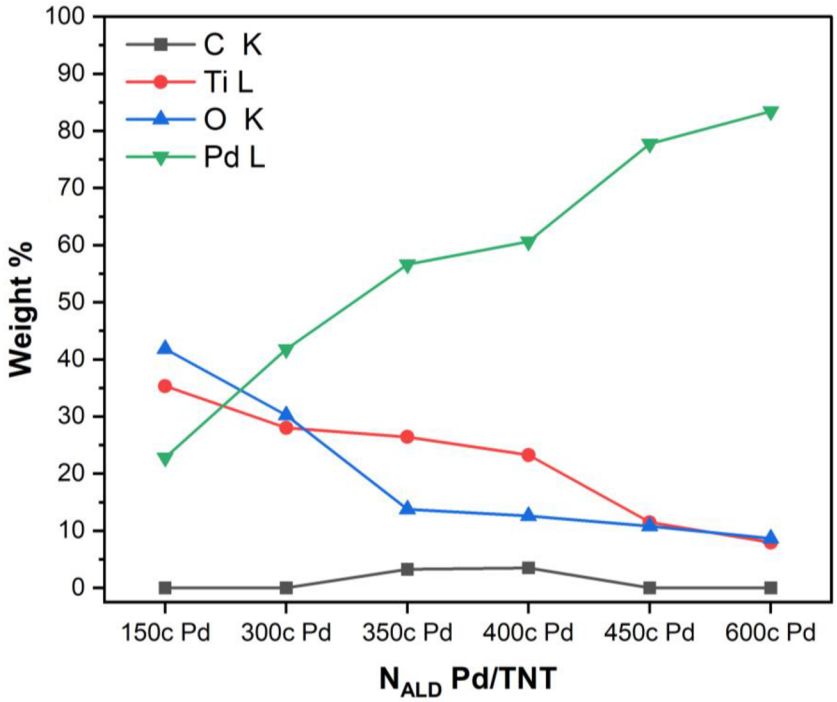

Figure 2.A.2. *EDX quantification of elements for Pd decorated TNTs with different* N_{ALD} *= 150, 300, 350, 400, 450, and 600, before electrochemical measurements, acquired using 5kv as electron beam energy source.*

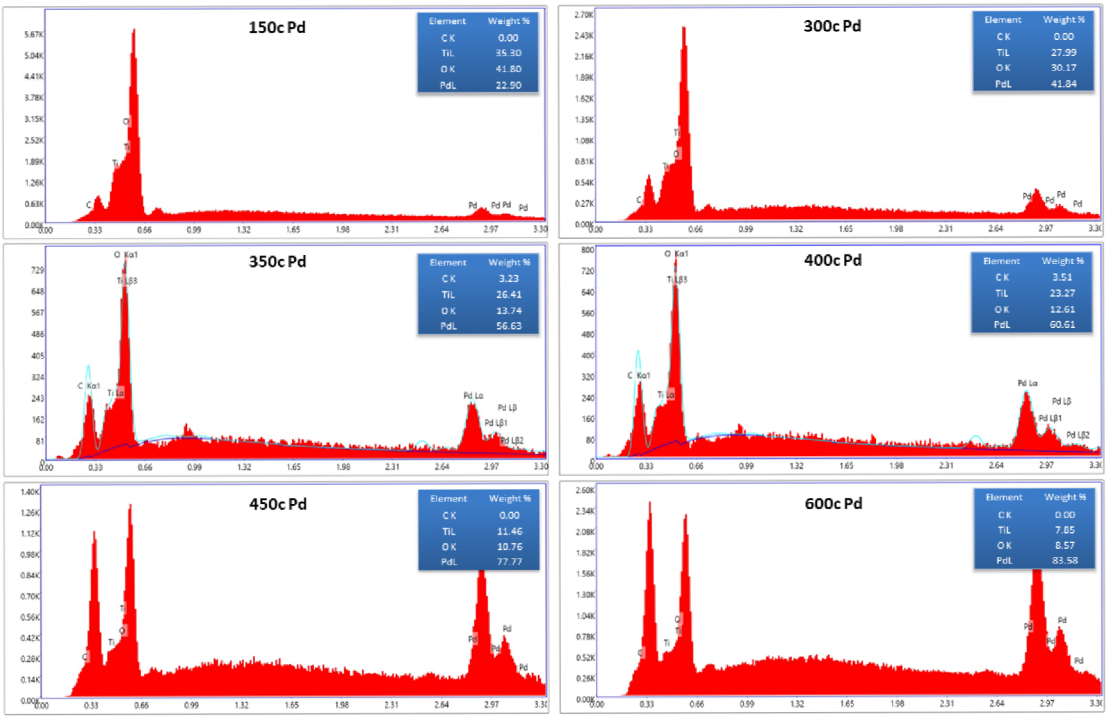

Figure 2.A.3. *EDX spectra recorded for Pd/TNTs with different* N_{ALD} *= 150, 300, 350, 400, 450, and 600, before electrochemical measurements, acquired using 5kV electron beam energy.*

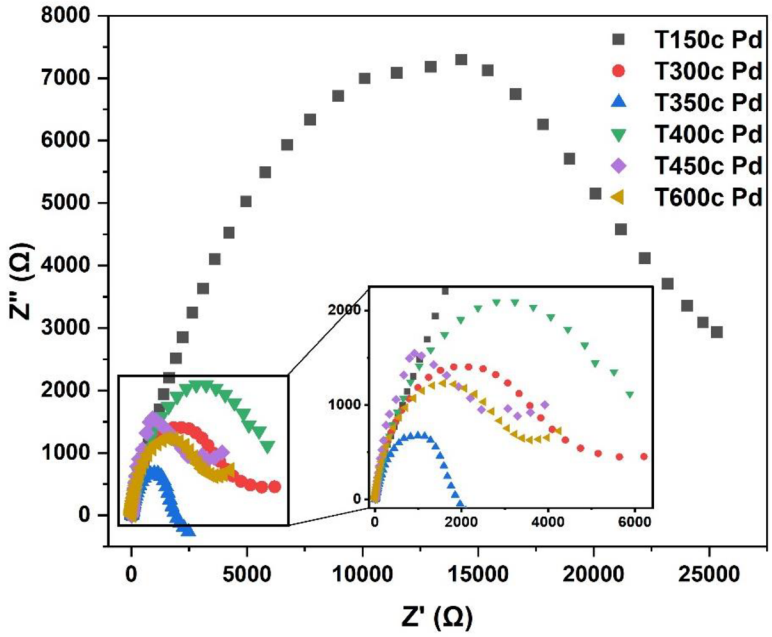

Figure 2.A.4. *EIS Nyquist plots for Ti foils decorated with Pd using N_{ALD} = 150, 300, 350, 400, 450, 600, recorded at 0.8 V_{RHE} in 1M KOH + 1M CH_3OH.*

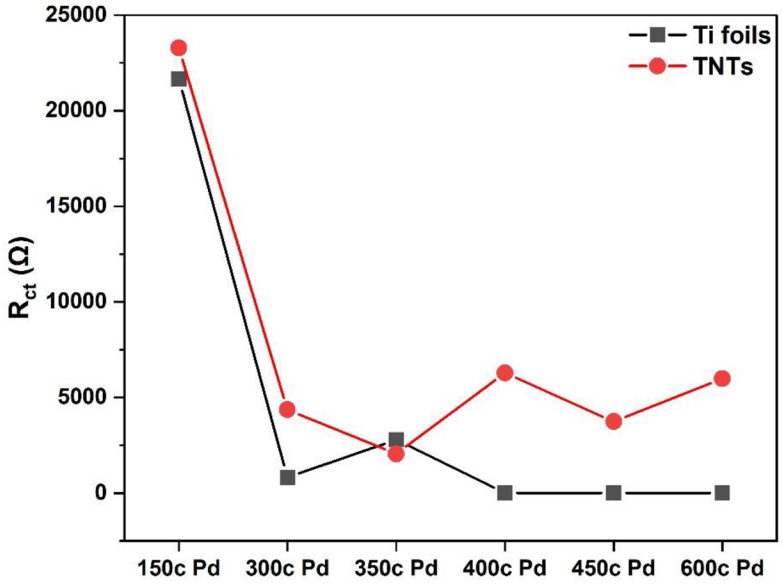

Figure 2.A.5. *Charge transfer resistance (R_{ct}) for Pd deposited on TNTs and Ti foils obtained by fitting the EIS Nyquist plots, shown in* ***Figure 2.5*** *and* ***Figure 2.A.4****, respectively. Using [R(RQ)] circuit model for Ti foils and [R(RQ)(RQ)] for TNTs.*

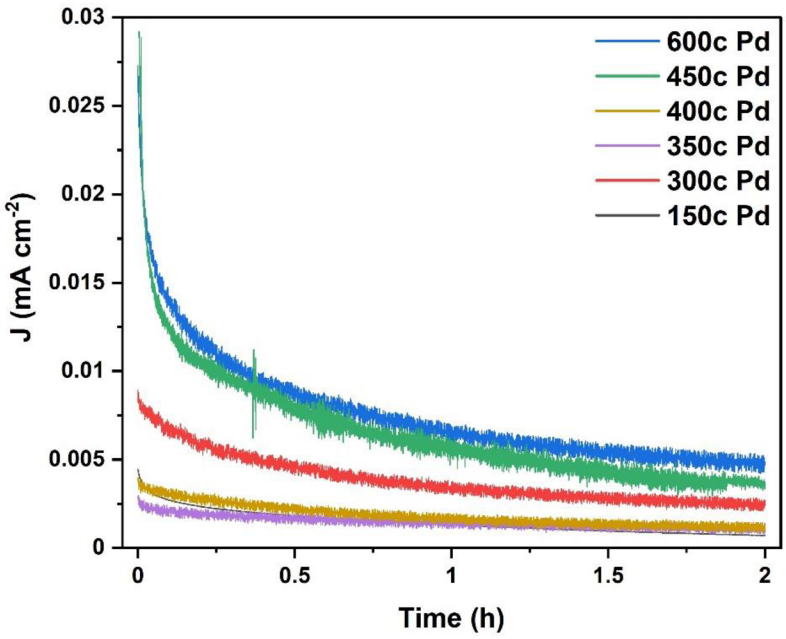

Figure 2.A.6. *Chrono-amperometric curves recorded to evaluate the stability of Pd decorated Ti foils with different N_{ALD} =150, 300, 350, 400, 450, and 600, recorded in 1M KOH + 1M CH_3OH at 0.9V for 2 h.*

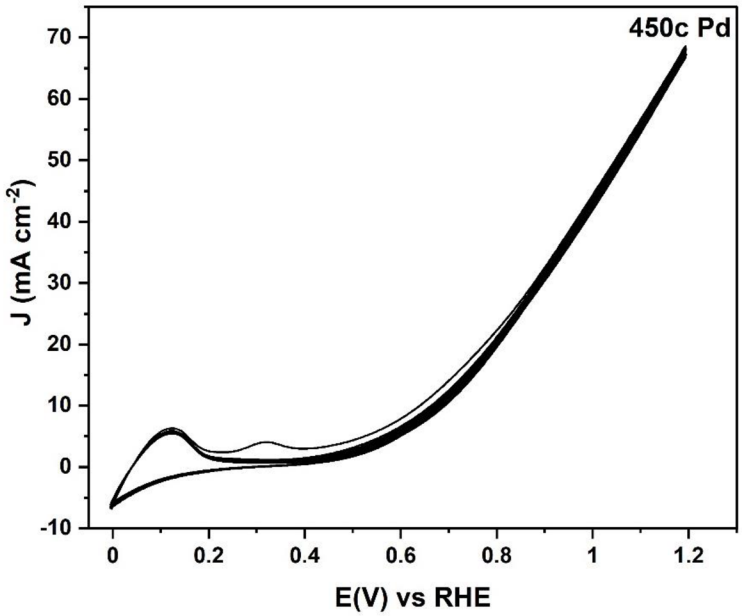

Figure 2.A.7. *Cyclic voltammogram for the TNT layer decorated with 450c Pd ALD cycles, recorded for 22 cycles in 1M KOH + 1M CH_3OH.*

(a)

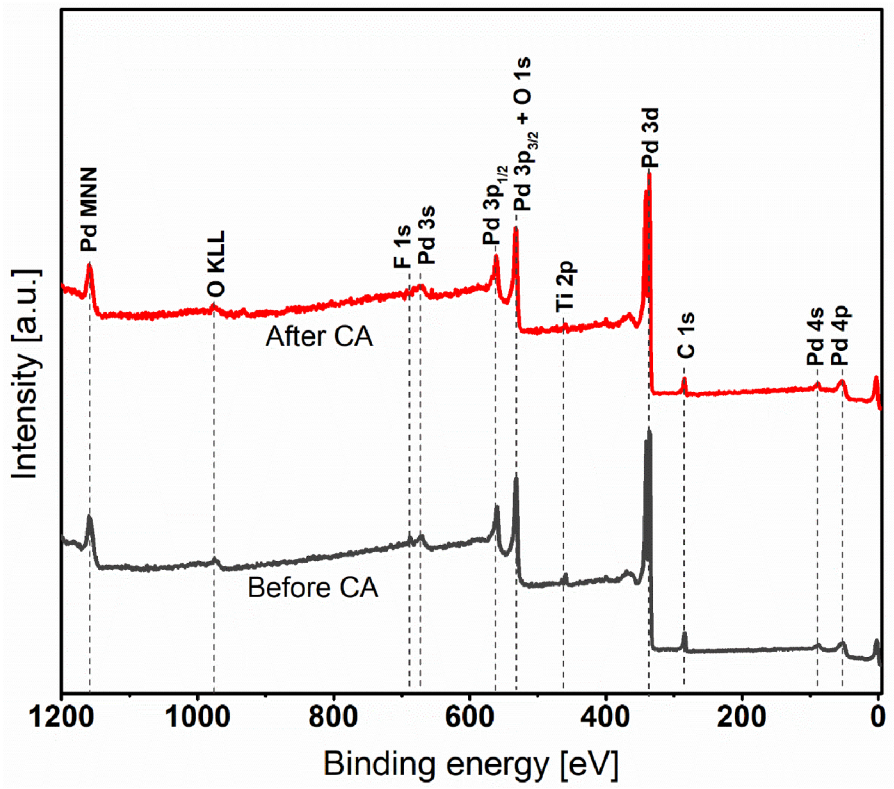

(b)

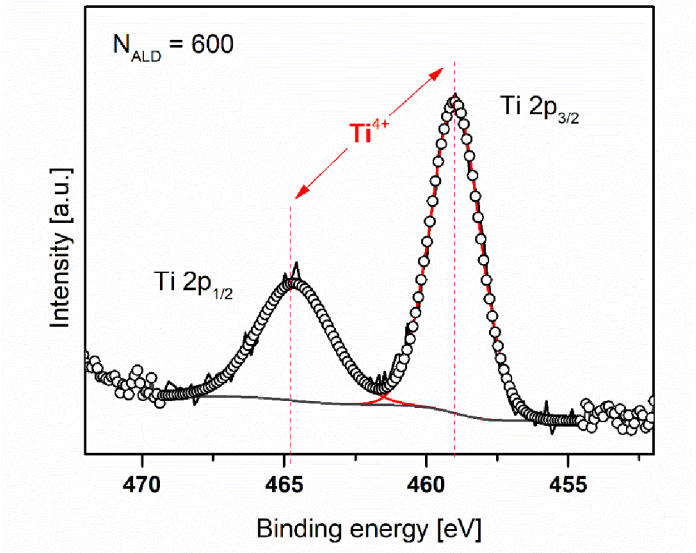

Figure 2.A.8. *a) Wide XPS survey spectra of Pd/TNT layer with 600 Pd N_{ALD} before and after CA measurements, b) Ti 2p high resolution spectrum reveals only the Ti^{4+} state, since Ti $2p_{3/2}$ is at ~459 eV.*

References

[1] V.C. Anitha, R. Zazpe, M. Krbal, J.E. Yoo, H. Sopha, J. Prikryl, G. Cha, S. Slang, P. Schmuki, J.M. Macak, Anodic TiO2 nanotubes decorated by Pt nanoparticles using ALD: An efficient electrocatalyst for methanol oxidation, J. Catal. 365 (2018) 86–93. https://doi.org/10.1016/j.jcat.2018.06.017.

[2] L. Assaud, N. Brazeau, M.K.S. Barr, M. Hanbücken, S. Ntais, E.A. Baranova, L. Santinacci, Atomic Layer Deposition of Pd Nanoparticles on TiO2 Nanotubes for Ethanol Electrooxidation: Synthesis and Electrochemical Properties, ACS Appl. Mater. Interfaces 7 (2015) 24533–24542. https://doi.org/10.1021/acsami.5b06056.

[3] S. Kunz, F.F. Schweinberger, V. Habibpour, M. Röttgen, C. Harding, M. Arenz, U. Heiz, Temperature dependent CO oxidation mechanisms on size-selected clusters, J. Phys. Chem. C 114 (2010) 1651–1654. https://doi.org/10.1021/jp911269z.

[4] P. Trogadas, V. Ramani, Pt/C/MnO2 hybrid electrocatalysts for degradation mitigation in polymer electrolyte fuel cells, J. Power Sources 174 (2007) 159–163. https://doi.org/10.1016/j.jpowsour.2007.08.088.

[5] D. Horiguchi, T. Tsukatsune, Z. Noda, A. Hayashi, K. Sasaki, Pt/SnO2 Electrocatalysts on Conductive Fillers, ECS Trans. 64 (2014) 215–220. https://doi.org/10.1149/06403.0215ecst.

[6] M. Xu, P. Da, H. Wu, D. Zhao, G. Zheng, Controlled Sn-doping in TiO2 nanowire photoanodes with enhanced photoelectrochemical conversion, Nano Lett. 12 (2012) 1503–1508. https://doi.org/10.1021/nl2042968.

[7] A.R. Puigdollers, P. Schlexer, S. Tosoni, G. Pacchioni, Increasing oxide reducibility: The role of metal/oxide interfaces in the formation of oxygen vacancies, ACS Catal. 7 (2017) 6493–6513. https://doi.org/10.1021/acscatal.7b01913.

[8] Y. Suchorski, S.M. Kozlov, I. Bespalov, M. Datler, D. Vogel, Z. Budinska, K.M. Neyman, G. Rupprechter, The role of metal/oxide interfaces for long-range metal particle activation during CO oxidation, Nat. Mater. 17 (2018) 519–522. https://doi.org/10.1038/s41563-018-0080-y.

[9] M. Bellini, E. Berretti, M. Innocenti, G. Magherini, M.V. Pagliaro, L. Poggini, H.A. Miller, A. Lavacchi, F. Vizza, 3D Titania Nanotube Array Support for Water Electrolysis Palladium Catalysts, Electrochim. Acta 383 (2021) 138338. https://doi.org/10.1016/j.electacta.2021.138338.

[10] R. Manoharan, J. Prabhuram, Possibilities of prevention of formation of poisoning species on direct methanol fuel cell anodes, J. Power Sources 96 (2001) 220–225. https://doi.org/10.1016/S0378-7753(00)00683-2.

[11] J.L. Cohen, D.J. Volpe, H.D. Abruña, Electrochemical determination of activation

energies for methanol oxidation on polycrystalline platinum in acidic and alkaline electrolytes, Phys. Chem. Chem. Phys. 9 (2007) 49–77. https://doi.org/10.1039/b612040g.

[12] S.M. Lang, T. Schnabel, T.M. Bernhardt, Reactions of carbon monoxide with free palladium oxide clusters: Strongly size dependent competition between adsorption and combustion, Phys. Chem. Chem. Phys. 14 (2012) 9364–9370. https://doi.org/10.1039/c2cp23976k.

[13] H.X. Zhang, C. Wang, J.Y. Wang, J.J. Zhai, W. Bin Cai, Carbon-supported Pd-Pt nanoalloy with low Pt content and superior catalysis for formic acid electro-oxidation, J. Phys. Chem. C 114 (2010) 6446–6451. https://doi.org/10.1021/jp100835b.

[14] L.M.M. Palma, T.S.S. Almeida, A.R.R. de Andrade, Comparative study of catalyst effect on ethanol electrooxidation in alkaline medium: Pt- and Pd-based catalysts containing Sn and Ru, J. Electroanal. Chem. 878 (2020) 114592. https://doi.org/10.1016/j.jelechem.2020.114592.

[15] M.K.S. Barr, L. Assaud, N. Brazeau, M. Hanbücken, S. Ntais, L. Santinacci, E.A. Baranova, Enhancement of Pd Catalytic Activity toward Ethanol Electrooxidation by Atomic Layer Deposition of SnO 2 onto TiO 2 Nanotubes, J. Phys. Chem. C 121 (2017) 17727–17736. https://doi.org/10.1021/acs.jpcc.7b05799.

[16] X. Zhang, J. Zhu, C.S. Tiwary, Z. Ma, H. Huang, J. Zhang, Z. Lu, W. Huang, Y. Wu, Palladium Nanoparticles Supported on Nitrogen and Sulfur Dual-Doped Graphene as Highly Active Electrocatalysts for Formic Acid and Methanol Oxidation, ACS Appl. Mater. Interfaces 8 (2016) 10858–10865. https://doi.org/10.1021/acsami.6b01580.

[17] Y.X. Chen, A. Lavacchi, S.P. Chen, F. di Benedetto, M. Bevilacqua, C. Bianchini, P. Fornasiero, M. Innocenti, M. Marelli, W. Oberhauser, S.G. Sun, F. Vizza, Electrochemical milling and faceting: Size reduction and catalytic activation of palladium nanoparticles, Angew. Chemie - Int. Ed. 51 (2012) 8500–8504. https://doi.org/10.1002/anie.201203589.

[18] W. Xu, S. Zhu, Z. Li, Z. Cui, X. Yang, Synthesis and catalytic properties of Pd nanoparticles loaded nanoporous TiO2 material, Electrochim. Acta 114 (2013) 35–41. https://doi.org/10.1016/j.electacta.2013.09.084.

[19] F. Hu, F. Ding, S. Song, P.K. Shen, Pd electrocatalyst supported on carbonized TiO2 nanotube for ethanol oxidation, J. Power Sources 163 (2006) 415–419. https://doi.org/10.1016/j.jpowsour.2006.09.039.

[20] Y.H. Qin, H.H. Yang, R.L. Lv, W.G. Wang, C.W. Wang, TiO2 nanotube arrays supported Pd nanoparticles for ethanol electrooxidation in alkaline media, Electrochim. Acta 106 (2013) 372–377. https://doi.org/10.1016/J.ELECTACTA.2013.05.067.

[21] A. Merenda, M. Weber, M. Bechelany, F.-M.M. Allioux, L. Hyde, L. Kong, L.F. Dumée, Fabrication of Pd-TiO2 nanotube photoactive junctions via Atomic Layer Deposition for persistent pesticide pollutants degradation, Appl. Surf. Sci. 483 (2019) 219–230. https://doi.org/10.1016/j.apsusc.2019.03.285.

[22] J. Lu, J.G. Bao, X. Lu, D. Zheng, X. Li, Application of a Pd-TiO2 nanotube/Ti electrode prepared by atomic layer deposition to reductive dechlorination of trichloroethylene, Electrochem. Commun. 103 (2019) 72–76. https://doi.org/10.1016/j.elecom.2019.05.007.

[23] J. Shu, R. Li, Z. Lian, W. Zhang, R. Jin, H. Yang, S. Li, In-situ oxidation of Palladium–Iridium nanoalloy anchored on Nitrogen-doped graphene as an efficient catalyst for methanol electrooxidation, J. Colloid Interface Sci. 605 (2022) 44–53. https://doi.org/10.1016/j.jcis.2021.07.056.

[24] S. Das, H. Sopha, M. Krbal, R. Zazpe, V. Podzemna, J. Prikryl, J.M. Macak, Electrochemical Infilling of CuInSe 2 within TiO 2 Nanotube Layers and Subsequent Photoelectrochemical Studies, (2016). https://doi.org/10.1002/celc.201600763.

[25] M.C. Militello, S.J. Simko, Elemental Palladium by XPS, Surf. Sci. Spectra 3 (1994) 387–394. https://doi.org/10.1116/1.1247783.

[26] T.L. Barr, Recent advances in x-ray photoelectron spectroscopy studies of oxides, J. Vac. Sci. Technol. A 9 (1991) 1793–1805. https://doi.org/10.1116/1.577464.

[27] D. German, E. Pakrieva, E. Kolobova, S.A.C. Carabineiro, M. Stucchi, A. Villa, L. Prati, N. Bogdanchikova, V. Cortés Corberán, A. Pestryakov, Oxidation of 5-Hydroxymethylfurfural on Supported Ag, Au, Pd and Bimetallic Pd-Au Catalysts: Effect of the Support, Catal. 11 (2021). https://doi.org/10.3390/catal11010115.

[28] G.A. Shafeev, J. -M. Themlin, L. Bellard, W. Marine, A. Cros, Enhanced adherence of area-selective electroless metal plating on insulators, J. Vac. Sci. Technol. A 14 (1996) 319–326. https://doi.org/10.1116/1.579895.

[29] W. Gao, R. Jin, J. Chen, X. Guan, H. Zeng, F. Zhang, Z. Liu, N. Guan, Titania-Supported Pd–Cu Bimetallic Catalyst for the Reduction of Nitrite Ions in Drinking Water, Catal. Letters 91 (2003) 25–30. https://doi.org/10.1023/B:CATL.0000006312.32227.4a.

[30] T. Jurzinsky, B. Kintzel, R. Bär, C. Cremers, J. Tübke, Methanol oxidation on PdRh/C electrocatalyst in alkaline media: Temperature and methanol concentration dependencies, J. Electroanal. Chem. 776 (2016) 49–52. https://doi.org/10.1016/j.jelechem.2016.06.038.

[31] P. Krawczyk, T. Rozmanowski, M. Frankowski, Methanol Electrooxidation at Electrodes Made of Exfoliated Graphite/Nickel/Palladium Composite, Catal. Letters 149 (2019) 2307–2316. https://doi.org/10.1007/s10562-019-02785-9.

[32] P.S. Deshpande, V.R. Chaudhari, B.L.V. V Prasad, Mechanistic Aspects of Methanol Electro-Oxidation Reaction through Cyclic Voltammetry : Is It Correct to Blame Carbon Monoxide for Catalyst Poisoning ?, Energy Technol. 1900955 (2020) 1–7. https://doi.org/10.1002/ente.201900955.

[33] R. Ojani, Z. Abkar, E. Hasheminejad, J.B. Raoof, Rapid fabrication of Cu / Pd nano / micro-particles porous-structured catalyst using hydrogen bubbles dynamic template and their enhanced catalytic performance for formic acid electrooxidation, Int. J. Hydrogen Energy 39 (2014) 7788–7797. https://doi.org/10.1016/j.ijhydene.2014.03.081.

[34] S. Li, M. Yang, R. Jin, H. Niu, C. Liao, H. Yang, J. Jin, J. Ma, Coupling palladium nanocrystals over D-phenylalanine-functionalized carbon nanotubes as an advanced electrocatalyst for hydrogen evolution and ethanol oxidation, Electrochim. Acta 364 (2020) 137290. https://doi.org/10.1016/j.electacta.2020.137290.

[35] T.E. Society, C. Augusto, C. Rold, Experimental Protocol for HOR and ORR in Alkaline Electrochemical Measurements JES F OCUS I SSUE ON E LECTROCATALYSIS — I N H ONOR OF R ADOSLAV A DZIC Experimental Protocol for HOR and ORR in Alkaline, (2018). https://doi.org/10.1149/2.0011815jes.

[36] D. Zhan, J. Velmurugan, M. V Mirkin, Adsorption / Desorption of Hydrogen on Pt Nanoelectrodes : Evidence of Surface Diffusion and Spillover, (2009).

[37] D.Y. Chung, K.J. Lee, Y.E. Sung, Methanol Electro-Oxidation on the Pt Surface: Revisiting the Cyclic Voltammetry Interpretation, J. Phys. Chem. C 120 (2016) 9028–9035. https://doi.org/10.1021/acs.jpcc.5b12303.

[38] M.K.S. Barr, L. Assaud, N. Brazeau, M. Hanbücken, S. Ntais, L. Santinacci, E.A. Baranova, Enhancement of Pd Catalytic Activity toward Ethanol Electrooxidation by Atomic Layer Deposition of SnO2 onto TiO2 Nanotubes, J. Phys. Chem. C 121 (2017) 17727–17736. https://doi.org/10.1021/acs.jpcc.7b05799.

[39] E.D. Rus, R.H. Wakabayashi, H. Wang, H.D. Abruña, Methanol Oxidation at Platinum in Alkaline Media: A Study of the Effects of Hydroxide Concentration and of Mass Transport, ChemPhysChem (2021). https://doi.org/10.1002/cphc.202100087.

[40] M. Wang, D.J. Guo, H.L. Li, High activity of novel Pd/TiO2 nanotube catalysts for methanol electro-oxidation, J. Solid State Chem. 178 (2005) 1996–2000. https://doi.org/10.1016/j.jssc.2005.04.006.

[41] R. Liang, A. Hu, J. Persic, Y.N. Zhou, Palladium Nanoparticles Loaded on Carbon Modified TiO2 Nanobelts for Enhanced Methanol Electrooxidation, Nano-Micro Lett. 5 (2013) 202–212. https://doi.org/10.1007/bf03353751.

Chapter 3: Synergistic effect of Pd single atoms and nanoparticles deposited on carbon supports by ALD boosts alkaline Hydrogen Evolution Reaction

Published as "Synergistic effect of Pd single atoms and nanoparticles deposited on carbon supports by ALD boosts alkaline hydrogen evolution reaction," B. Bawab, S. M. Thalluri, E. Kolíbalová, R. Zazpe, L. Jelinek, J. Rodriguez-Pereira, J. M. Macak, Chemical Engineering Journal, vol. 482, p. 148959, Feb. 2024.

3.1. Abstract

The synergistic effects between carbon supports and noble metal species of an electrocatalyst are known to effectively boost the alkaline hydrogen evolution reaction (HER). Herein, Atomic Layer Deposition (ALD) was employed to decorate carbon papers with Pd species comprising single atoms (SAs) and nanoparticles (NPs). Transmission electron microscopy analysis revealed the metallic nature and coexistence of Pd as SAs and NPs. The results of X-ray photoelectron spectroscopy supported the evidenced SA species, manifested as the Pd^{2+}. An increase in the electrochemical active surface area from 12.98 to 413.48 cm^{-2} was evidenced with increasing ALD cycles from 30 to 300c Pd and remained unchanged until 600c Pd. The exceptional overpotential for CP 600c Pd exhibits the lowest value of 4.55 mV, compared to previous reports for Pd electrocatalysts in a non-acidic environment, and confirms the synergistic effect of Pd SAs and NPs that plays a major role in enhancing alkaline HER.

3.2. Introduction:

Hydrogen is a clean and renewable energy carrier that can be produced by electrochemical water splitting [1]. Among the catalysts studied for hydrogen evolution reaction (HER), Platinum (Pt) has emerged as a standard due to its unique activity for HER [2,3], combined with low overpotentials [4–7] and very low Pt loading [8], in addition to other catalysts such as Ru [9–12], Ir [13], and Rh [14]. However, one of the problems that arise from the utilization of Pt as well as the other mentioned catalysts is its high cost and scarcity, which limit the large-scale application. In addition, the slower kinetics of Pt in alkaline electrolytes of approximately 3 times lower than that in acidic medium [4,15], triggered the search for substitution with similar or better performance for HER purposes. The focus on hydrogen production in an alkaline medium was more in demand because corrosion issues arise from the use of an acidic environment during the long term HER process [16]. Therefore, the development of alternative catalyst is needed that can perform excellent in alkaline media.

To address these challenges, Palladium (Pd) emerges as a promising alternative to Pt showing good catalytic activity and long-term chemical stability through HER [17,18], especially in alkaline media [19]. One strategy to achieve this is to combine Pd single atoms (SAs) and nanoparticles (NPs) on suitable supports, which can create synergistic effects between the two types of Pd species and enhance the catalytic performance of Pd. A study [20] demonstrates the synergistic activity by anchoring the Pd species on carbon self-doped graphitic carbon nitride (CCN_x). The mechanism reveals that the synergy of the Pd species as electron trapping sites significantly lowers the energy barrier of H* activation. On the other hand, Pd can form alloys and hydrides with other metals to enhance its activity and stability for hydrogen evolution reaction [21,22]. Previous studies [23] demonstrate a significant low overpotential for Pd NPs of approximately 80 mV at a current density of 100 mA cm^{-2} related to the porous Pd nanoparticle assemblies. In some other cases such as Pd-Cu-H [24] that show high catalytic performance and attributes this to the better H* adsorption and activation on the Pd surface. Moreover, Zheng et al.[25] reported that with increasing the size of Pd NPs from 3 to 19 nm, higher HER exchange currents were obtained in both acidic and alkaline medium due to the

decreasing trend of surface defects with increase in NPs size. Furthermore, the proximity of active species on a support introduces the intriguing concept of the hydrogen spillover effect [26,27], wherein H* species can diffuse from donor to acceptor sites, potentially enhancing the catalytic activity. This phenomenon becomes pivotal when considering the cooperative synergy between SAs and NPs in catalysis. Recent research [28–30] has illuminated the possibility of integrating SAs and NPs on the same support, creating a platform for novel catalytic interactions. This synergy holds the potential to catalyze reactions that may be challenging for either SAs or NPs alone.

Carbon-based materials [31,32] are widely used as supports for electrocatalysts, as they are low cost, have high stability, and good electrical conductivity. Among them, carbon papers (CPs) have a high porosity and surface area [33], which can facilitate catalyst distribution, the mass transport of reactants and products during HER, good electrical conductivity known to enhance the charge transfer, and mechanical stability to support durability of catalysts for practical long term HER applications. Therefore, CPs are a promising substrate for electrocatalysis. In addition, CP can be easily treated with an acidic solution to introduce functional groups such as carboxylic acid, hydroxyl, and carbonyl on the surface of carbon substrates [34,35], which can increase their wettability and improved affinity with metal precursors during deposition process. The degree of acid treatment can affect the hydrophilicity of carbon substrates, as well as their mechanical, thermal, and electrochemical properties.

This study aims to explore the synergistic interplay between Pd SAs and NPs on a suitable support for enhanced HER performance. The employed acid-treated CPs as substrates has been employed for the deposition of Pd species using ALD [36], resulting in the simultaneous presence of Pd species as both SAs and NPs. Furthermore, along the manuscript, Pd SAs and NPs are collectively referred to Pd species. Different number of ALD cycles (N_{ALD}) comprising of 30, 45, 60, 75, 150, 300, 450 and 600 were applied to exploit the presence of Pd species and related activity for alkaline HER. High-angle annular dark field scanning transmission electron microscopy (HAADF-STEM) images evaluation confirmed the coexistence of Pd species as SAs and NPs on CPs starting from N_{ALD} = 75c Pd. The electrochemical measurements showed low overpotential values of 4.55 mV vs reversible hydrogen electrode (RHE) along with low charge transfer

resistance (R_{ct}) of 0.65 Ω at 20 mV of applied potential for the CP 600c Pd sample. To evaluate the HER activity of the catalysts, the electrochemical surface area (ECSA) and the number of available active sites was assessed. Long-term stability tests employing a staircase chronopotentiometry at different current densities show excellent stability of CPs decorated with Pd NPs for duration of 15 h in comparison to Pt developed by similar ALD route [12]. Accelerated degradations tests at high scan rate in a limited potential window further confirmed the excellent durability of the developed CP-600c Pd sample.

3.3. Experimental

3.3.1. Electrode preparation/treatment

Commercial carbon papers (CP) were treated with a 1:3 mixtures of HNO_3 and H_2SO_4 for 15 min under sonication at 60 °C. The acid treatment is known to enhance the hydrophilic nature of the carbon substrates [12,37]. Subsequently, the CPs were thoroughly rinsed with distilled H_2O several times. The resulting CPs were employed in ALD for Pd deposition.

3.3.2. Atomic Layer Deposition of Pd

Pd species were deposited onto treated CPs using a TFS 200 ALD reactor. Palladium(II)hexafluoroacetylacetonate $Pd(C_5HF_6O_2)_2$ and formalin were used as the precursor and co-reactant. The Pd precursor was heated to 65 °C and the deposition process temperature was 200 °C. The ALD cycle was defined by a sequence of Pd pulse (2 s), N_2 purge (30 s), formalin pulse (1s), and N_2 purge (30 s). A preliminary step of 250 ms of Pd precursor with a 30s N_2 purge and 1s formalin with a 30 s purge for 20 cycles was applied to lower the Pd precursor consumption. This is because in early stages of the ALD process, the volatility of the Pd precursor is significantly higher, which can lead to issues related to excess Pd precursor wastage and control. By distributing the initial pulses in this manner, better control over precursor consumption was achieve, ensuring that the reactor is always with saturated with provided pulse duration. Thus, the total number of ALD cycles were calculated taking into consideration of initial 20 cycles (20 +

x cycles = Total number of cycles). Different "number of Pd ALD cycles (N_{ALD})" were performed on CPs with: N_{ALD} = 30, 45, 60, 75, 150, 300, 450, and 600 cycles.

3.3.3. Characterization methods

Pd deposited CPs were characterized using Scanning Electron Microscopy (SEM, FEI Verios 460L) and compared to the Blank CP. High-resolution Transmission Electron Microscopy (HRTEM, Titan Themis 60-300, Thermo Fisher Scientific,) operated at 300 kV was also employed. HRTEM is equipped with a Cs image aberration corrector, high-angle annular dark field scanning transmission detector (HAADF-STEM), and Super-X energy dispersive X-ray (EDX) spectrometry with four 30 mm^2 windowless detectors for STEM-EDX analysis to evaluate the elemental composition and the morphology of the deposited Pd. The crystallinity was assessed using X-ray diffraction XRD Rigaku Smartlab 3 kW diffractometer equipped with Cu-Kα1 radiation source (λ = 1.54060 Å), using 40 kV and 30 mA as beam energy source. The patterns were collected in the 2θ range (10 - 90°) and at a scanning rate of 0.01 °/step with a speed of 4 °/min. To verify the surface chemical composition before and after electrochemical measurements, X-ray photoelectron spectroscopy (XPS) analysis was performed using Kratos Analytical Axis Supra instrument, with Al-Kα monochromatic X-ray source (hν = 1486.69 eV). The acquired spectra were further fitted using CasaXPS software and referenced to the sp^2 species in C 1s signal at 284.0 eV. In order to perform the binding energy scale correction. Pd 3d spectra were fitted with asymmetric Lorentzian function LA (0.95, 2, 150) for metallic state (Pd^0) and mixed Gaussian-Lorentzian functions GL (30) for Pd oxides and Pd plasmon loss. Inductively coupled plasma - optical emission spectroscopy (ICP-OES) analyses were performed using (Thermo-Fischer iCAP 7400) axial mode, RF power 1150 W, 340.458, 324.270, and 363.470 nm after dissolving the CP@Pd in a solution of 1:3 mixture of HCl and HNO_3 in a microwave reactor (Multiwave 5000 – Anton-Parr).

3.3.4. Electrochemical analysis

Electrochemical measurements were performed using the Autolab VIONIC potentiostat supported by INTELLO software, where 1 M KOH was used as an electrolyte. A

calibrated Ag/AgCl (3 M KCl = 0.210 V versus RHE) used as a reference electrode, graphite rod was used as a counter electrode and CPs with and without Pd was used as a working electrode. Linear sweep voltammetry (LSV) was performed at a scan rate of 2 mV s^{-1}, where the Tafel slopes are plotted after 100% iR correction. Electrochemical Impedance Spectroscopy (EIS) was evaluated at 20 mV overpotential using 10 mV as an AC perturbation potential, within a frequency range of 10^2 to 10^5 Hz. Copper underpotential deposition method was used to estimate the electrochemical surface area (ECSA) at a scanning rate of 10 mV s^{-1} and compared for all samples. Stability measurements were performed by 15 h long chrono-potentiometry. Stability measurements were also performed by accelerated degradation test by subjecting the catalyst to 2500 repetitions of cyclic potential sweeps in the potential range of ±50 mV at a higher scanning rate of 50 mV s^{-1}, in comparison to activity measurements of 2 mV s^{-1}. All the potentials presented are given versus RHE unless otherwise stated.

3.4. Results and discussion

3.4.1. Morphological and chemical characterization

Figure 3.A.1[*] shows SEM images of CP blank and ALD decorated CPs with Pd species. For reference, images of CP decorated with Pt NPs are shown as well. The CPs decorated with Pd species by different N_{ALD} from 0 to 600c Pd are presented. Samples with N_{ALD} = 75, 150, and 300 (Fig. 3.A.1 b-d) exhibit sparse and scattered Pd NPs on the surface of CPs. However, for $N_{ALD} \geq 450$ and 600 (Fig. S1e,f), the coverage of Pd NPs becomes more evident, in terms of size and distribution. During the ALD process for noble metals, the initial nucleation stage is followed by atom aggregation, leading to the formation of atomic clusters, which subsequently develop into NPs [12,38,39]. However, the utilization of acid-treated carbon substrates offers several advantages, including the provision of additional active sites for Pd precursor adsorption and facilitating enhanced Pd nucleation and growth [40]. A nucleation delay can be noted during the ALD process with the Pd precursor employed, which is in line with reported observations due to difficulty in removal of re-adsorbed Pd precursor ligands (hexafluoroacetylacetonate) on

[*] Appendix data can be found at the end of this chapter, page 79.

the support. The nucleation delay during the ALD process with the Pd precursor is a phenomenon that occurs when the Pd precursor does not react readily with the substrate surface, resulting in a slow and incomplete film formation. One possible explanation for this behavior is that the Pd precursor ligands, are strongly adsorbed on the surface and hinder the subsequent reactions of the Pd precursor with the surface hydroxyl groups. This can lead to a self-limiting effect, where the Pd precursor molecules compete with the adsorbed ligands for the available surface sites, and the growth rate decreases as the surface coverage increases [41]. **Fig. 3.A.1g,h** provides morphological overview of ALD decorated CP 50c Pt. N_{ALD} of 50 c was chosen for Pt, taking into consideration of previous reports [12,42]. The ALD of Pt on CPs shows an excellent coverage.

More in-depth information about the Pd species on CPs was obtained by HRTEM studies, where the elemental composition and indexing of crystalline lattice of Pd NPs were collected. **Figure 3.1** shows the high-angle annular dark-field imaging (HAADF) and dark field (DF4) images, providing further information about the presence of Pd species. The CP 30c Pd sample showed no traces of NPs, but only SAs that were marked by red circles in the relevant images. Increasing the N_{ALD} to 45c showed a mixture of SAs and SA clusters (marked by a red square, while no NPs were observed. When the N_{ALD} increased to 75c, the presence of NPs was observed in addition to SAs and SA clusters. The presence of SAs in addition to NPs on CP 150, 300, and 600c Pd was also approved by TEM in **Fig. 3.A.2a-c** with further XPS analysis provided later.

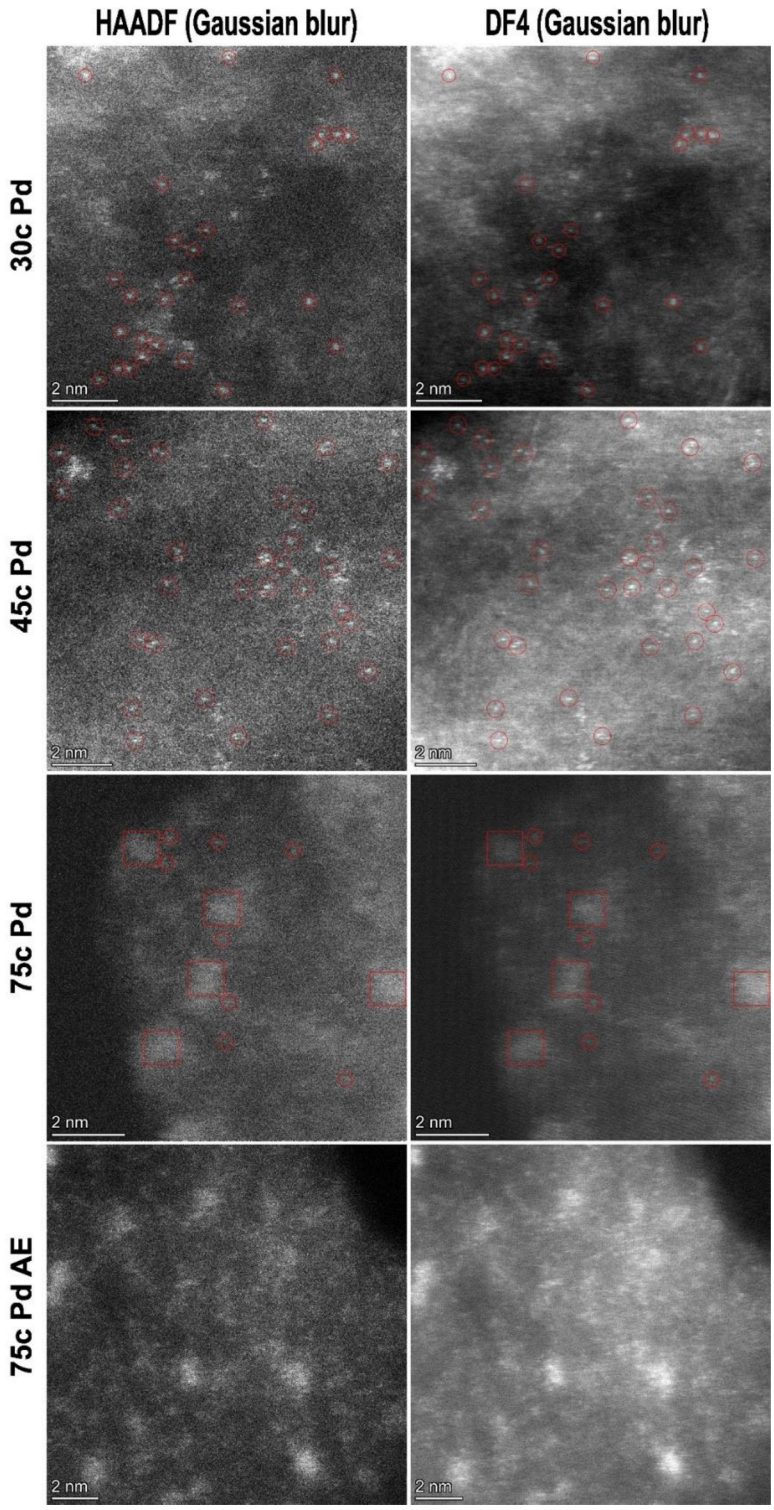

Figure 3.1. *HAADF-STEM images (left column) and Dark field (DF4) (right column) images for 30, 45, and 75c Pd (before and after electrochemical measurements (AE)).*

Fig. 3.A.3a-i shows the elemental distribution by combining HAADF-STEM imaging and STEM-EDX for the CP 600c Pd sample, providing elemental mapping for C-K, O-K, Pd-L, and ovelapped C+O+Pd maps, respectively. From the mapping, a significant reduction in oxygen distribution at Pd NPs location suggesting dominance of metallic nature from ALD depositied Pd. This was further confirmed by the STEM-EDX line scan that was conducted to take advantage of isolated Pd NP on CP as shown in **Fig. 3.A.3e**. **Fig. 3.A.3f** provides details of the graphical weight percentages along the analysed line scan (**Fig. 3.A.3e**) for C, O and Pd. The trend of O line when compared with Pd line were inversly related providing a cross confirmation of metallic nature of the ALD deposited Pd. HAADF-STEM imaging from **Fig. 3.A.1** revealed the presence of SA for lower N_{ALD} sample (CP 30c Pd), clusters (CP 45c Pd) and NPs staring from 75c Pd, which is in accordance to the ALD noble metal deposition profile, as suggested before. The distribution density of individual species of Pd increases with increase in N_{ALD}. As shown in **Fig. 3.A.4**, the NPs sizes exhibit a gradual growth with increasing the ALD cycles, showing average sizes of 0.7, 1.3, 7.1, 8.1 nm size for 75 c, 150c, 300c, and 600c Pd, respectively. The Fast Fourier Transformation (FFT) pattern obtained from a single Pd NP (**Fig. 3.A.3g-i**) reveals distinct diffractions represented by marked spots. These diffractions correspond to cubic structure and to (311), (002) and (111) planes with d-spacings of 0.12, 0.19, and 0.23 nm, respectively, which is inline with XRD analysis.

The crystal structure and phase composition of the CPs modified with Pd species were investigated by X-ray diffraction (XRD). **Fig. 3.A.5** shows the XRD patterns of the CPs decorated with Pd using different N_{ALD}. The Pd peaks are barely visible for $N_{ALD} = 75$ (indicating a low Pd loading on the surface) and become more evident from $N_{ALD} \geq 150$, suggesting crystalline nature and a higher Pd loading with increased N_{ALD}. However, some of the Pd peaks are partially overlapped by the CP substrate peaks evidenced at higher N_{ALD} (300 to 600 cycles), especially around 44.59°. The ALD Pd has a cubic crystal structure with diffraction peaks matching well with the standard reference pattern (PDF 01-087-0641). The characteristic Pd peaks at 2θ = 39.39, 45.8, 66.7, and 80.4° correspond to the (111), (200), (220), and (311) lattice planes, respectively. The diffraction peaks intensity for Pd increases with increasing the ALD cycles with lower half width of full maxima indicating a gradual increase in the crystallite size from 5.03 to

5.61 nm for CP 300c Pd to CP 600c Pd respectively (**Equation (3.A.1)**, **Table (3.A.1)** in the appendix of this chapter).

XPS analysis for CP 600c Pd was carried out to gain more insight about the surface chemical composition. **Fig. 3.2a** shows the wide-scan XPS survey spectrum revealing the presence of C, O, and Pd elements, where the C peak was used to correct the binding energy scale of the spectra. The minor peak observed for F arise from the fact of the re-adsorbed Pd precursor fragments (containing F species) on the substrate as explained before. On the other hand, Pd 3d two sublevels shown in **Fig. 3.2c** exhibits a significant amount of Pd in metallic form, as shown in the red fitted curves at 335 and 340.3 eV. Here, the peak energy splitting for Pd 3d spin-orbit doublets appears to be around 5.26 eV, similar values to those reported in the literature [43,44]. The shoulder peaks fitted in blue curves and located around 336.4 and 341.6 eV were denoted as Pd^{2+} and they correspond to the bonding with surface active O linked species, such as (C-OH and O-C=O) in the 286-289 eV range originated as a result of CP pretreatments resulting in Sas [45,46] and also a minor amount from O that forms PdO as a result of sample exposure to air, in-line with previous reports [44]. The olive peaks correspond to Pd^{4+} species centered at 338.2 and 343.4 eV. The reported PdO binding energy for CP 600c Pd was around 336.4 eV, close to the values reported for the surface oxides in the literature [47–50]. It is important to note that the bulk oxides typically exhibit lower binding energies. This is supported by the presence of Pd SAs detected by TEM, which contributes to the presence of shoulder Pd peak [45,51,52] (represented as Pd^{2+}). **Table 3.A.2** provides a quantitative assessment for the deconvoluted high resolution spectra of Pd peak, confirming atomic percentages of 79.8 and 13.5 for Pd^{0} and Pd^{+2} components, respectively.

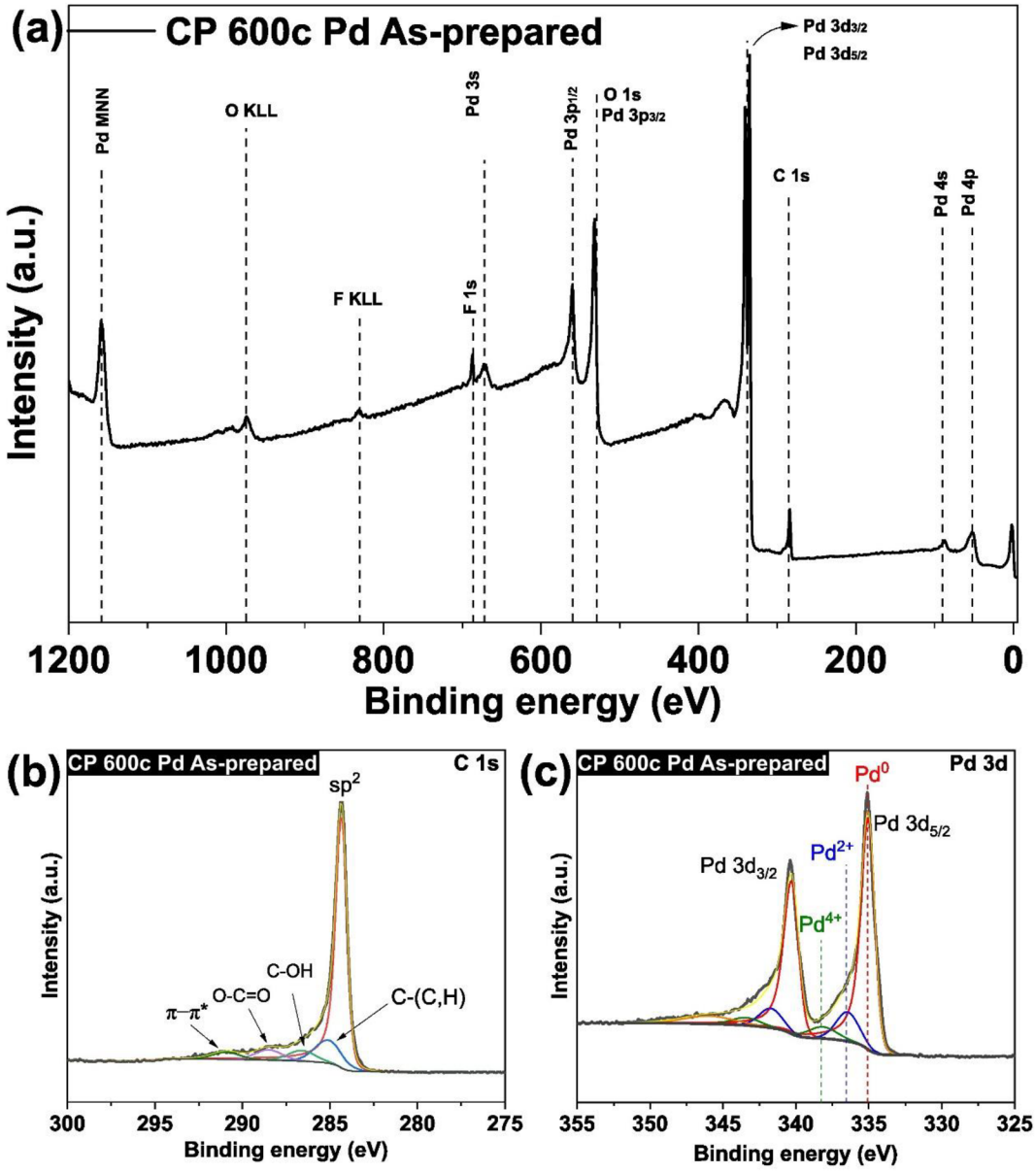

Figure 3.2. *XPS spectra of CP 600c Pd sample: a) wide survey spectra; b) and c) high-resolution spectra for C 1s and Pd 3d, respectively.*

3.4.2. HER activity of CP@Pd

During the H_2O dissociation on the surface of Pd, OH^- and H^* are formed as intermediates, where the H^* will participate in the production of H_2. Polarization experiments were conducted to investigate the performance of CPs decorated with Pd species for HER activity. The LSV analysis was performed in 1 M KOH solution with a further iR correction as shown in **Fig. 3.3a**. The LSV curves show excellent HER activity, with a blank CP sample shown as a reference. It is important to assess the overpotential for each electrode required to reach a cathodic current density of 10 mA cm^{-2}. The data in **Fig. 3.3a** shows that the presence of only SAs as a catalyst on the lowest N_{ALD} (30c Pd) results in much higher overpotential of 313.6 mV. As the SA density increases, SA clusters start to form, as shown in **Fig. 3.1** for 45c Pd, leading to lower overpotentials. A substantial decrease in overpotential values was obtained for 75c Pd ALD, leading to as low overpotential as 28.8 mV, a much lower value than the commercial Pd/C and Pt/C reported with a value of 175 and 72 mV [53]. Increasing the Pd loading quantity to 450 and 600c ALD shows a gain in overpotentials recording 5 and 4.55 mV, respectively. The observed overpotentials are much lower than the values reported in the literature [23,24]. This indicates that the treated CPs with ALD decorated Pd species have supported to facilitate faster electron transfer and H_2O reduction.

Tafel analysis was used as a parameter to elucidate the reaction mechanism and kinetics of the HER taking place at Pd species surface. This can provide a clear understanding of the Pd species behavior, and the mechanism involved within the HER. According to previous findings [54–56], Tafel slope for Pd NPs can range from 40 to 130 mV dec^{-1}. In the present case, the CP@Pd species including NPs, such as N_{ALD} 75c, 150c, 300c, 450c, and 600c, have Tafel slopes of 99, 59, 49, 47, and 49 mV dec^{-1} respectively, as shown in **Fig. 3.3b** indicating that the reaction kinetics follow Volmer-Heyrovsky mechanism. However, the lower Pd loaded CPs with SAs showed substantial increase in Tafel slope value recording 265, 197, and 226 mV dec^{-1} for 30, 45, and 60c Pd, respectively. The improved kinetics of Pd species on CP increased with increasing N_{ALD} up to 300c Pd, while higher N_{ALD} (300, 450, and 600) showed very similar Tafel slopes. The N_{ALD} of Pd deposition influenced the Pd species density, which played a critical role for alkaline

HER performance. According to our understanding, the optimal density of Pd species for HER performance was observed with N_{ALD} 300c and stabilizes with further increase until 600c Pd. However, the Tafel slope obtained from N_{ALD} 300 to 600c Pd, is comparable to some of the best reported values for Pd-based electrocatalysts[53]. For a comparative purpose, Tafel slope values for CP 50c Pt overlayed in **Fig. 3.3b** showing a value of 50.14 mV dec^{-1}, which is close to those recorded for the higher Pd loading of 450 and 600c Pd.

The initial H_2O dissociation has been widely considered as bottle neck problem for alkaline HER. A previous study [57] provides valuable insights into this process through comprehensive investigations, utilizing both Density Functional Theory (DFT) calculations and Extended X-ray Absorption Fine Structure (EXAFS) measurements. These analyses elucidate the role of Pd NPs as active centers in facilitating H_2O dissociation, leading to the generation of key reactive species, active Hydrogen atoms (H*) and hydroxyl groups (OH^-). Our study builds upon these findings by investigating the impact of NPs in the context of our experimental framework. A pronounced correlation between the presence and concentration of NPs and the enhancement of H_2O dissociation was observed. The increased footprint of NPs in the samples of CP@Pd with the rise in N_{ALD} concentration suggests a relation with improved H_2O dissociation, resulting in the enhanced generation of reactive H* species. Our findings support and further demonstrate the significance of NPs in the H_2O dissociation process during the alkaline HER. By integrating the results from reference [56] with our own experimental observations, the aim was to provide a more complete understanding of this critical reaction mechanism.

The generated H* on the Pd NPs surface are expected to spillover onto the available SAs of Pd, where the Volmer-Heyrovsky mechanism (explained in the Supplementary Information) occurs. Recently, the unprecedented activity for HER was demonstrated by SA of Pd[46] in comparison to SA of Pt and Au, when employed as cocatalysts on TiO_2 photocatalyst. This enhanced activity of Pd SA was mainly due to more prominent charge localization according to DFT analysis [46]. Similarly, in the current context, the adsorbed H^* on Pd SAs active sites reacts with the neighboring H_2O molecule, such that

the proton from the H_2O molecule combines with the adsorbed H* to form Hydrogen molecule (H_2). This overall synergistic effect between the Pd NPs and SAs represent the enhanced HER performance of the CP@Pd, the main highlight of this work.

Charge transfer analysis was carried out employing EIS and is presented in **Fig. 3.3c.** Fitting the experimental EIS data was carried out with a simple equivalent circuit model, consisting of only five elements. The circuit fits the experimental data well, as evidenced by the excellent agreement between the experimental data and the fitted data for all CPs decorated with Pd species. The fitting results illustrate the values of R_1, R_2/Q_1, and R_3/Q_2 indicating that the electrical properties of the CP substrate and the Pd species on CP in relation to the N_{ALD}. The values obtained from the fitting (**Table 3.A.3)** showed that the resistance (R_s) of the samples ranged from 2 to 3.19 Ω used for iR correction. The first parallel component (R_2/Q_1) illustrates the charge transfer kinetics of the carbon substrate, with resistance values varies from 0.57 to 1.69 Ω. While the second component (R_3/Q_2) illustrates the charge transfer resistance at the interface of catalytically active Pd species. The R_{ct} decreased significantly from 178.28 to 0.65 Ω with increasing N_{ALD} from 30 to 600c Pd. The decrease in R_{ct} with increase in N_{ALD}, confirms improvement on the electrical properties and thus the HER activity of CP@Pd. The observed increase in capacitance can be related to increase in the amount of adsorbed H* on the Pd surface [58]. The CP 50c Pt sample was used to perform a comparative assessment of HER under the same conditions. **Fig. 3.3d** provides a comprehensive view of the activity profiles of the respective electrodes, as depicted by the comparative bar plot of overpotentials and Tafel slopes. Pt displays an overpotential of 6.8 mV, which falls within the range of overpotential values observed for CP 300c and CP 450c Pd.

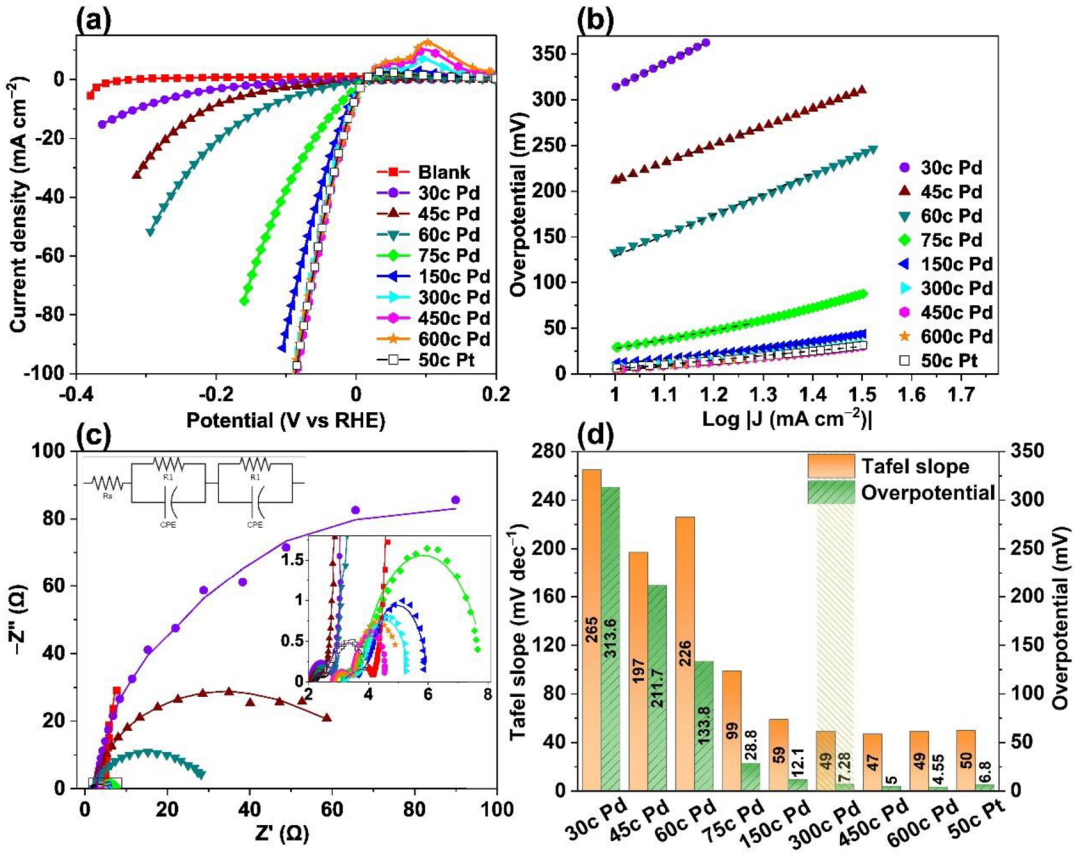

Figure 3.3. *Electrochemical HER analysis: a) iR corrected LSV; b) Tafel slope analysis in the current density range of (10 – ~30 mA cm^{-2}); (c) EIS experimental and fitting curves data; d) comparitive bar plot for Tafel slopes and overpotential values for CP Pd and CP 50c Pt samples.*

3.4.3. Number of active sites and their role in performance enhancement

For supported catalysts such as SA, NPs or thin films on flat or high surface area supports, the calculated electrochemical surface area (ECSA) used to determine the active catalyst surface area. One of the common methods to evaluate the ECSA of Pd noble metal electrocatalysts is to use the reduction peak of the oxide layer formed on the metal surface [59]. However, this method need to be carefully considered basing on the available Pd facets and potential range chosen in the CV scan to oxidize and reduce the Pd species available on the surface [60].

An alternative method that can overcome these drawbacks is to use under potential electrodeposition of Cu with a further stripping of deposited monolayer of Cu. Therefore, the ECSA for CP Pd electrodes was determined by integrating the Cu stripping peak, as shown in **Fig. 3.A.6(a-f)**. The initial choice of the applied potential was evaluated by performing a series of LSV initiating from different potentials as shown in **Fig. 3.A.6a**, where 0.31 V was used for Cu monolayer deposition. There is a large distinction of bulk Cu deposition and monolayer Cu deposition with applied initial potential for LSV. This potential for monolayer deposition was adopted for the rest of the CP samples decorated with Pd. As shown in **Fig. 3.4a**, ECSA increased gradually from 12.98 to 413.48 cm^2 as the N_{ALD} increased from 30c to 300c. Further increase in the N_{ALD} from 300 to 600c shows approximately close ECSA values of 413.48, 395.63, and 411.98 cm^2 respectively, which agrees with the overpotentials recorded from LSVs. The increase of ECSA values with increasing N_{ALD} can be attributed to the higher active surface area of Pd species exposed to the electrolyte [61–63]. Furthermore, the number of active sites (N) shown in **Fig. 3.4b** increases from 1.72×10^{16} to 5.47×10^{17} by increasing the N_{ALD} from 30 to 300c Pd, and with further increase in N_{ALD}, the number of active sites remains relatively stable with values of 5.47×10^{17}, 5.23×10^{17}, and 5.45×10^{17} for 300, 450, and 600c Pd respectively, which is proportional with ECSA obtained values. Therefore, the saturation of the available active sites starts to occur at N_{ALD} = 300c.

To gain deeper insight about the intrinsic activity of Pd species, the turnover frequency (TOF) was quantified as a pivotal marker of intrinsic catalytic performance [64]. TOF measures the efficiency of a catalyst active site for a specific reaction [65]. While our study has emphasized the ECSA values and the quantification of active sites within the Pd species, it is crucial to examine the TOF values, as depicted in **Fig. 3.4c**. Our analysis reveals that the TOF values for Pd species fall within the range of 0.15 to 0.22 H_2 s^{-1} at 30 mV, however, by applying $N_{ALD} \leq$ 45c Pd, TOF value start to decline. This suggest that apart from having only SAs as a catalyst, as observed in 30 and 45c Pd, all the samples share similar HER reaction strategy and only the increase in the number of active sites directly influences the low overpotentials observed with LSV measurements. It is worth noting that our determination of ECSA through copper monolayer deposition

involve both SAs and NPs present as a catalyst. This is a critical point of consideration in our TOF calculations.

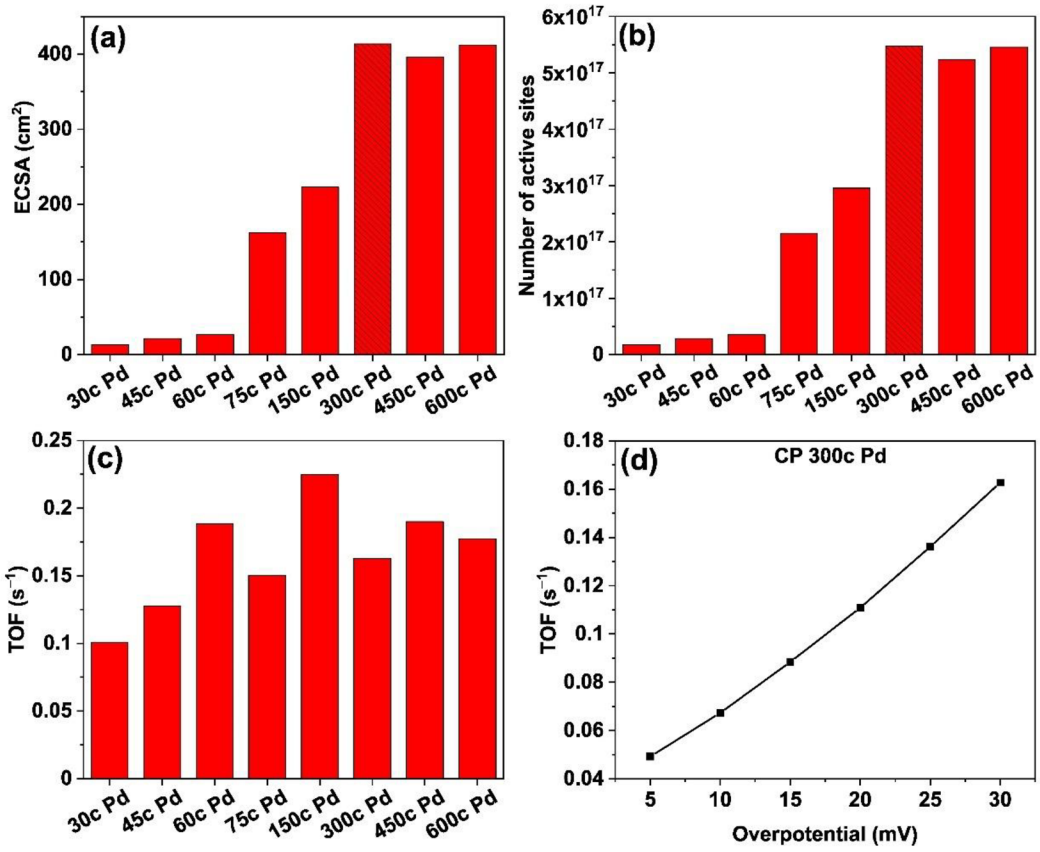

Figure 3.4. *a) Electrochemical surface area (ECSA); b) number of active sites; c) turnover frequency (TOF) for 75, 150,300, 450, and 600c Pd at 30 mV overpotential; d) TOF for CP 300c Pd at different overpotentials, where the connecting line used for eye guidance. The pattern highlighted columns in (a) and (b) referred to CP 300c Pd indicate the threshold at which the HER performance gets saturated.*

ICP-OES analysis was carried out for all samples that include NPs to determine the Pd metal loadings. The estimated weight percent (wt. %) of Pd as shown **Fig. 3.A.7** follow a linear increase of 1.61, 4.4, 9.87, 12.82, and 15.88 for CP 75, 150, 300, 450 and 600 c Pd, respectively. However, the activities found for the CP@Pd samples are mostly correlated with the number of active sites, rather than the loading mass, due to the fact that all the loading mass will not participate in the HER catalytic activity. It is possible to have

confusion when relating the improved overpotentials with the decrease in SAs as N_{ALD} increases. Due to agglomeration, the increase in NPs size as depicted in **Fig. 3.A.4** lowers the probability of SAs presence as the NPs are consuming larger area of the CP surface. However, NPs exhibit a stronger interaction with water molecules than SAs as described [57]. Thus, the increase in the NPs quantity in the higher Pd-loaded CPs resulting in producing more hydrogen atoms, compensating for the drop in Pd SAs.

3.4.4. Stability evaluation by staircase chronopotentiometric and accelerated degradation tests.

How well an electrocatalyst works in practice depends largely on how long it can maintain stable activity over the time. To further investigate the stability of CP 600c Pd, chronopotentiometric measurements for CP 600c Pd were assessed for 15 h with steps of different current densities, as shown in **Fig. 3.5a**. The overpotentials remained stable during the initial 12 h at an applied current density of 10 mA cm^{-2}. Stepping the current density to 20, 50, and 10 mA cm^{-2} and maintained for 1 h did not hamper the overpotential with change in current densities. In fact, a slight gain of 3 mV was observed during the final 1 h stability measurement employing 10 mA cm^{-2}. For comparison, 50c Pt ALD coated CP stability measurement was carried out under the same conditions. A raise in 10 mV of overpotentials were observed during the initial 12 h measurement at 10 mA cm^{-2}. Further changing the current densities to 20, 50, and 10 mA cm^{-2} displayed an average of 5, 2, and 6 mV higher overpotential, respectively, when compared with Pd.

LSV was performed for CP 600c Pd before and after the long-term stability test, as shown in **Fig. 3.5b**. The overpotential increased from 8.27 mV to 15.2 mV after the stability test, while the overpotential of CP 50c Pt increased from 6.8 mV to 17.6 mV, as shown in **Fig. 3.5c**. This is around 6.9 mV change for CP 600c Pd, compared to 10.8 mV for CP 50c Pt overpotential change, suggesting that CP@Pd retain more activity after the stability test. Part of the recorded change could be correlated to the loss of some fragments of the electrode due to H_2 bubbles generated on the surface. TEM (**Fig. 3.A.8**) and XPS (**Fig. 3.A.9 and Table 3.A.2**) analyses, carried out after the stability measurement, did not show any significant change in the morphology and oxidation state

of the samples. This is a promising result, as it suggests that the Pd species are stable and resistant to degradation under the test conditions. HR-TEM imaging and FFT pattern analysis in **Fig. 3.A.10a,b** showed that the Pd NPs had a matching cubic crystalline structure with the (311), (002) and (111) planes with d-spacings of 0.12, 0.19, and 0.23 nm, respectively, after stability measurements.

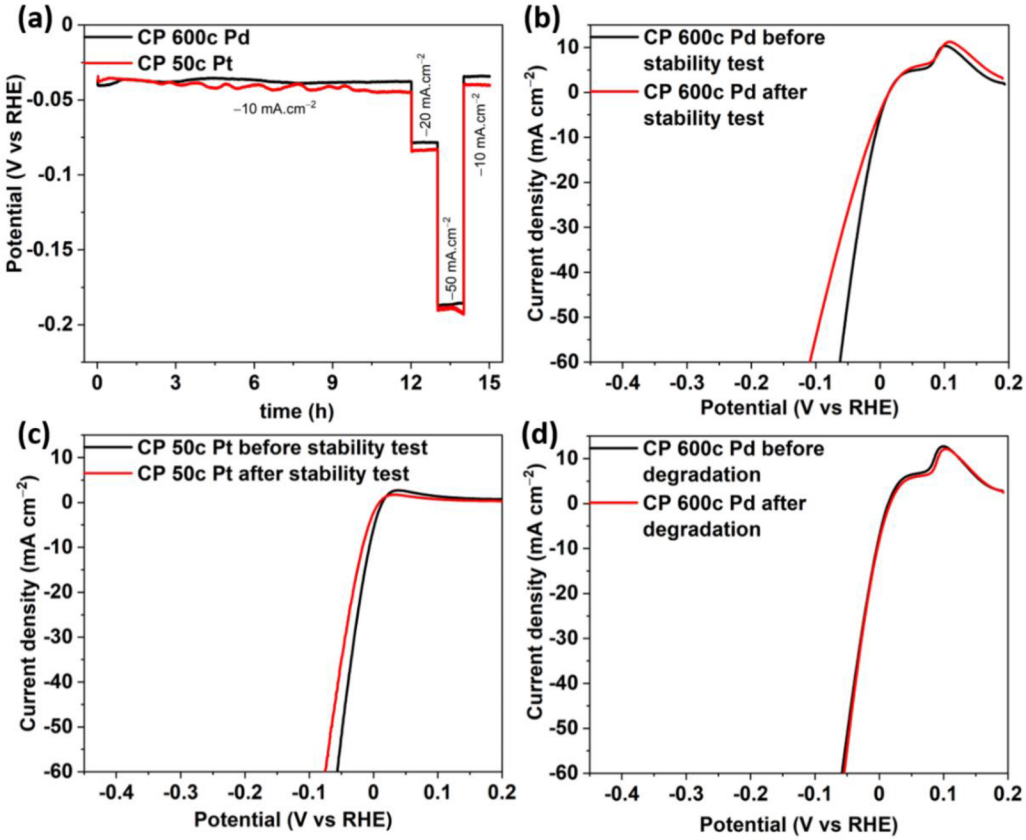

Figure 3.5. *Stability measurement: a) straicase chronopotentiometry ; b) LSV before and after stability test for CP 600c Pd; c) LSV before and after stability test for CP 50c Pt; d) LSV before and after degradation test for CP 600c Pd.*

Additionally, the stability of the electrodes was evaluated in dynamic conditions, where electrode was subjected to repeated CV at higher scan rate [66]. An accelerated degradation test was performed for the CP 600c Pd sample for 2500 cycles in a potential range of ± 50 mV and a scanning rate of 50 mV s^{-1}. The electrode displayed excellent stability, with 1 mV gain in the overpotential between the polarization curves collected

before and after test, as observed in **Fig. 3.5d**. A comparative summary of the relative overpotentials and Tafel slopes achieved in this work are listed in **Table 3.A.4**, along with results from other studies. The low values recorded for CP 450 and 600c Pd suggest excellent HER performance by highlighting the importance of using treated CPs and ALD technique to obtain Pd species comprising of SA and NPs having unique synergistic activity and excellent stability for the alkaline HER.

3.5. Conclusion

ALD was employed to decorate Pd species on activated CPs. The coexistence of both SAs and NPs plays the major role in improving the HER activity in an alkaline medium. The NPs play a crucial role in H_2O dissociation and the HER process proceeds in the presence of SAs. The combination of these parameters with an increased number of active sites by increasing N_{ALD}, ushered to an efficient and highly active catalyst with overpotentials of 4.55 mV. The overpotentials were comparable to CP@Pt catalyst prepared in similar fashion. However, the presence of only SAs on the lower Pd loaded CPs showed poor HER activity. Moreover, the developed CP@Pd catalyst showed excellent stability for prolonged duration with no significant loss in activity, as confirmed by various characterization techniques (XRD, XPS, HRTEM). Overall, this work highlights the synergistic effect of SAs and NPs of Pd on a conducting support as highly efficient and stable electrocatalysts for alkaline HER.

3.A. Appendix:

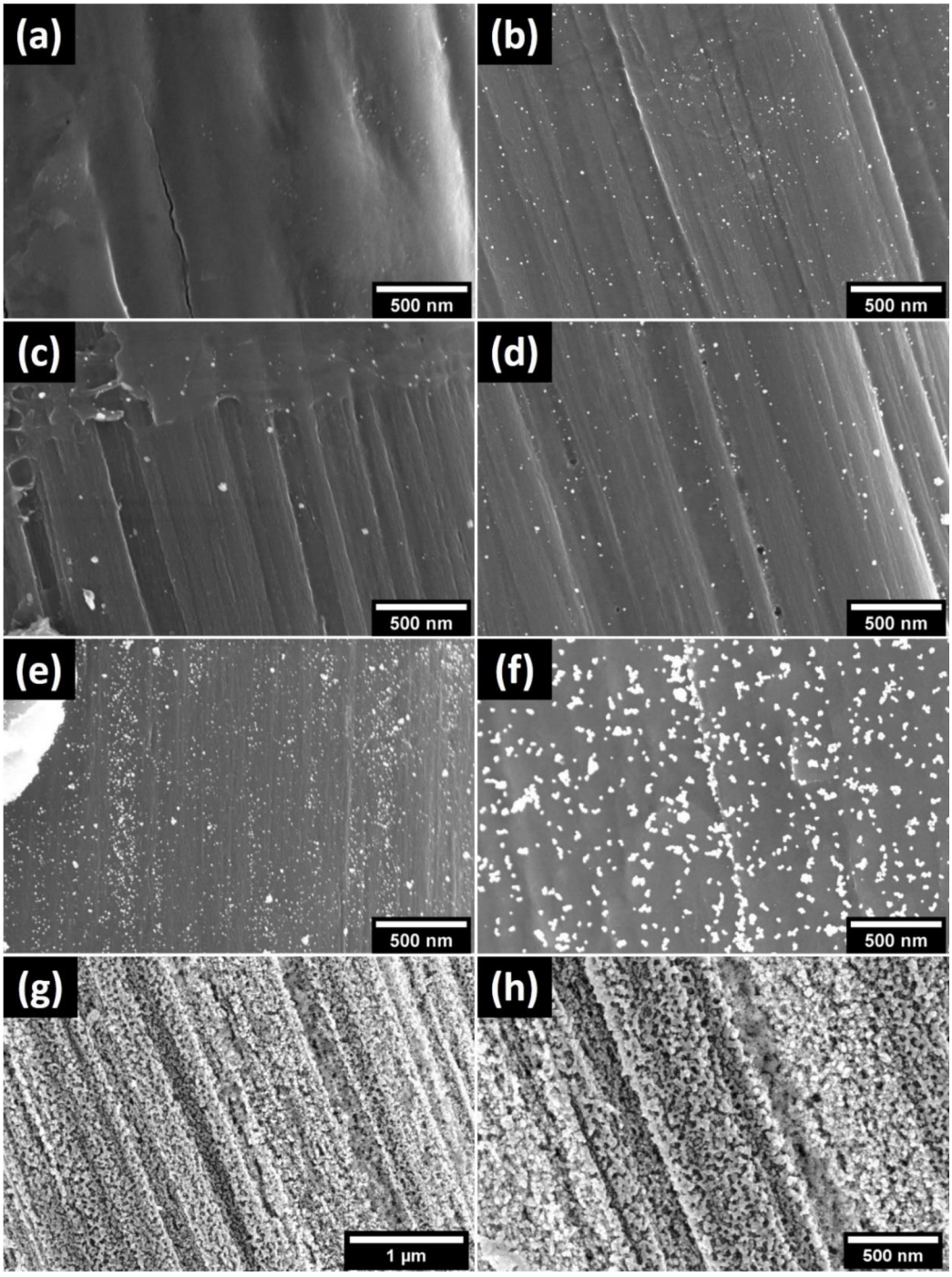

Figure 3.A.1. *SEM images of the CP surface with Pd NPs deposited using N_{ALD}: (a) Blank; (b) 75c; (c) 150c; (d) 300c; (e) 450c; (f) 600c; CP decorated with 50c Pt (g, h) as reference.*

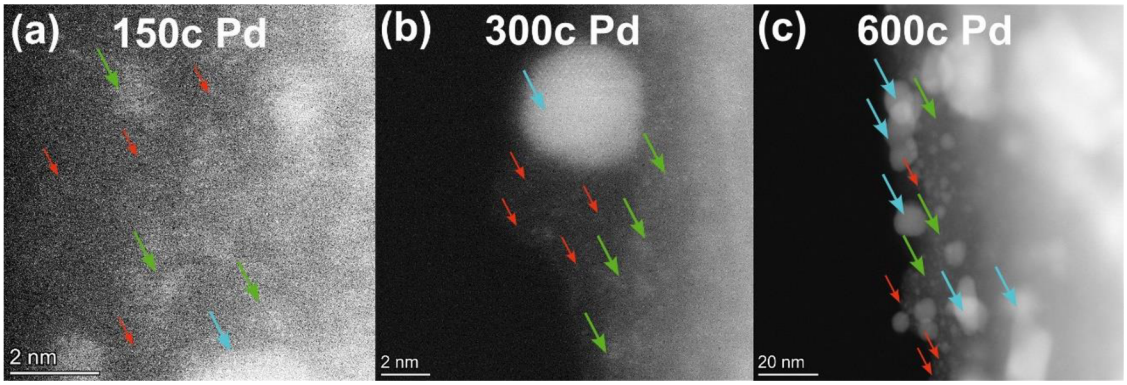

Figure 3.A.2. *(a) CP 150c Pd; (b) CP 300c Pd and (c) 600c Pd HAADF-STEM images. Arrow marks in red indicate SAs, green indicates atomic clusters and cyan indicate larger NPs.*

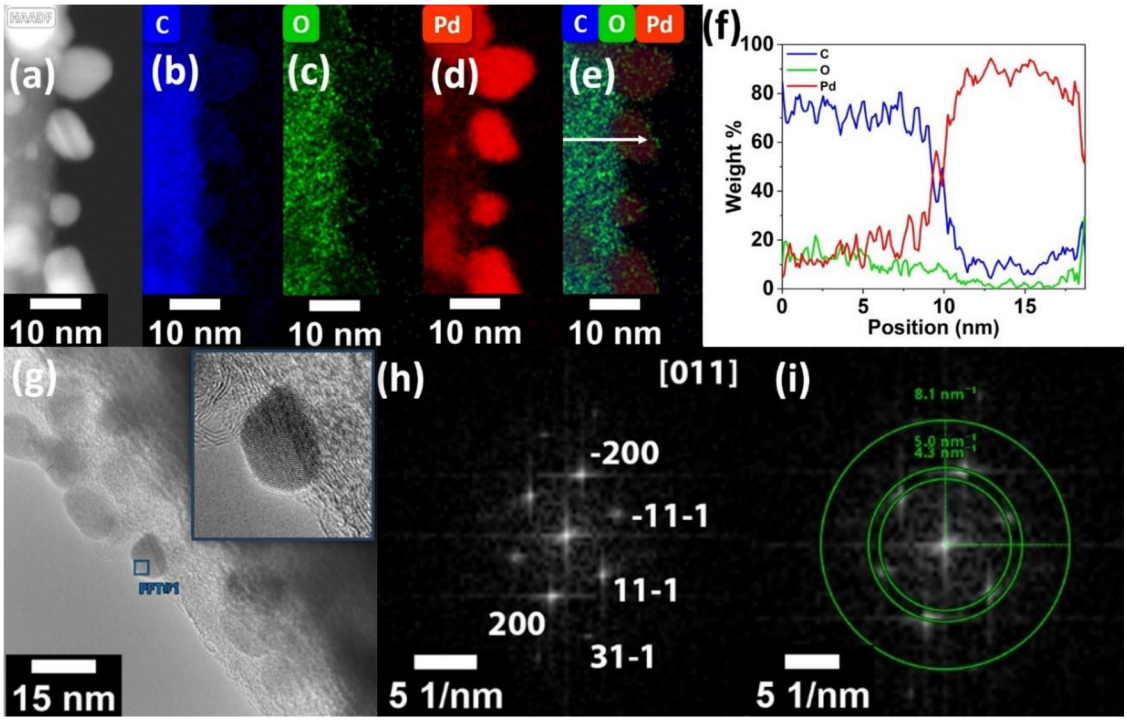

Figure 3.A.3. *TEM analysis: a) A HAADF-STEM image of CP 600c Pd sample; b-e) corresponding STEM-EDX elemental mapping, providing C-K, O-K, Pd-L, and overlapped maps; f) collected STEM-EDX spectrum obtained from the line scan, indicated by the white arrow shown in e); g) a HR-TEM image of the deposited Pd NPs used for FFT analysis (magnified insert); h) FFT analysis corresponding to a blue*

rectangle in g), revealing a Pd NP with cubic lattice oriented to [011] zonal axis; i) lattice d-spacing measurements obtained from FFT analysis of h).

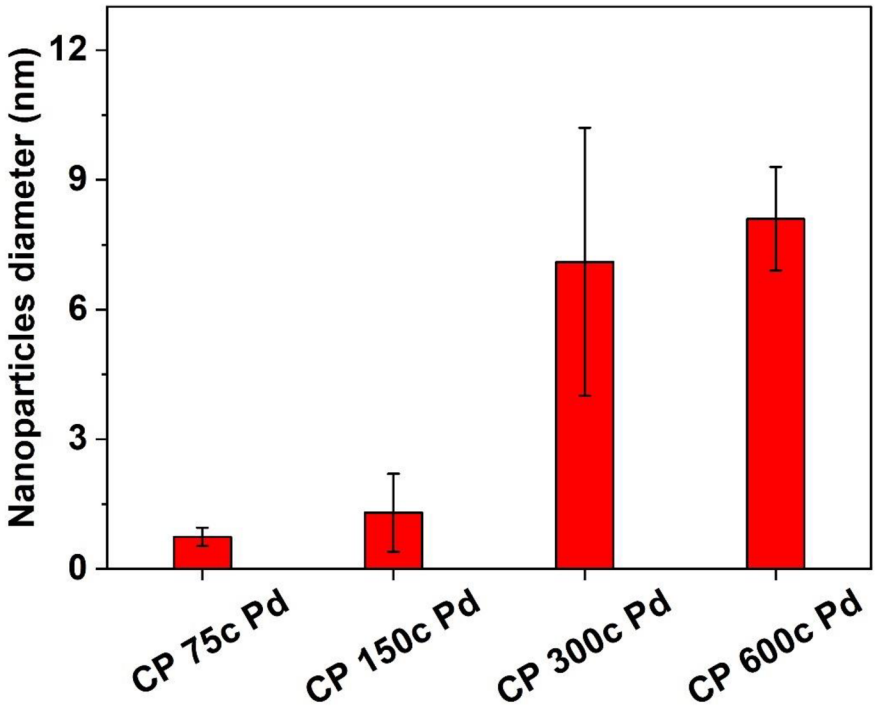

Figure 3.A.4. *Average diameter of Pd NPs determined from the HRTEM images.*

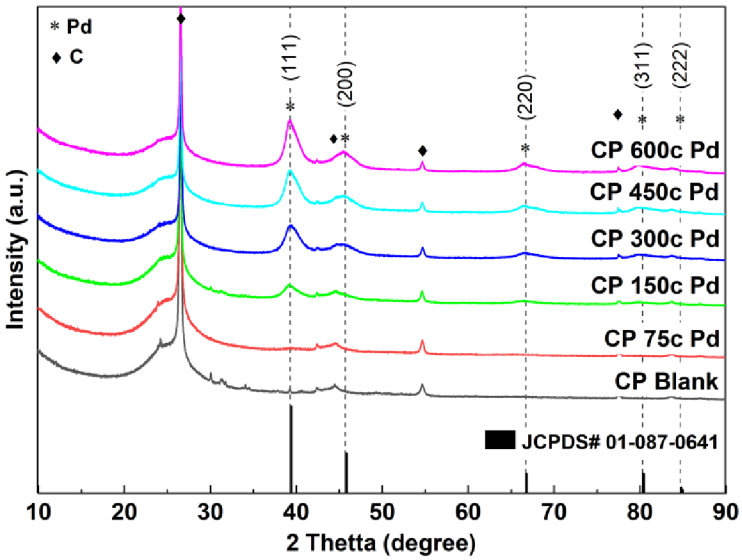

Figure 3.A.5. *XRD patterns of Pd-decorated CP for N_{ALD} 75, 150, 300, 450, and 600c and comparison to the blank CP.*

The average grain size of the Pd NPs was estimated using Scherrer's equation (1) from the XRD peaks of N_{ALD} = 450 and 600. The calculated grain size was about 5.616 nm coherent with the estimated NP size obtained from SEM micrographs, indicating a slight increase in the Pd NP size with N_{ALD} at this range.

$$d = \frac{K\lambda}{\beta\cos(\theta)} \qquad (3.A.1)$$

Such that (K = 0.9) is the Scherrer constant, (λ = 0.154 nm) is the wavelength of X-ray, and (β) is the full width at half maximum (FWHM). The result verifies the value obtained from the SEM micrograph.

Table 3.A.1. *Crystalline characteristics of cubic Pd NPs supported by carbon substrate derived from XRD data.*

catalyst	**2θ**	**Crystallite size (nm)**	**d (A°)**
CP 300c Pd	39.42	5.03	3.95

CP 450c Pd	39.32	5.11	3.96
CP 600c Pd	39.52	5.61	3.94

Table 3.A.2. *Atomic concentration (%) of Pd oxidation state determined by XPS for before and after stability measurement.*

	Pd^0	**Pd^{2+}**	**Pd^{4+}**
Before stability test	79.8	13.5	6.7
After stability test	67.7	26.9	5.4

Understanding Tafel kinetics:

To understand the mechanism of the rate limiting step of the reaction, the two possible pathways need to be examined: Volmer-Tafel and Volmer-Heyrovsky. Volmer-Tafel involves the adsorption of H* onto the electrode surface followed by recombination of the adjacent hydrogen induced by electron transfer to form H_2 as a product. However, low Tafel slopes obtained (**Figure 3.3b**) do not support this theory. Therefore, it is less likely that the Volmer-Tafel mechanism is the dominant. Volmer-Heyrovsky from the other hand, involves the adsorbed H* to interact with the adsorbed water molecule, producing H_2 as a result, which is the evident mechanism based on the low Tafel values obtained (lower than 40 mV dec^{-1}), suggesting the dominance of Volmer-Heyrovsky mechanism [56]. The possible chain reactions can occur according to reaction (3.A.2) and (3.A.4) successively [67].

Volmer: $$H_2O + e^- + Pd \rightleftharpoons Pd - H + OH^- \quad (3.A.2)$$

Tafel: $$2Pd - H \rightleftharpoons H_2 + 2Pd \quad (3.A.3)$$

Heyrovsky: $$Pd - H + H_2O + e^- \rightleftharpoons H_2 + OH^- + Pd \quad (3.A.4)$$

The relatively small variations in the values of a_2 for the different ALD cycles of Pd species suggest that the capacitance behavior of the Pd species is less sensitive to the

number of ALD cycles in the frequency range (10^{-2} – 10^{5}) compared to the more pronounced variations observed for CP substrate as shown for a_1. CP substrate has a porous and rough surface which can provide a large surface area for the deposition of Pd species. When Pd species are deposited on the CP substrate, they are well distributed on the surface of the substrate, increasing the effective active surface area. This increase in the effective active surface area leads to an increase in the capacitance of the CP substrate. On the other hand, the capacitance of Pd species fluctuates because their size and distribution on the carbon paper substrate may vary with different N_{ALD} of Pd. Additionally, the presence of surface impurities or defects on CP can also affect the capacitance of Pd NPs. These results suggest that the electrical properties of the CP substrate and the Pd species are strongly influenced by the number of ALD cycles.

Table 3.A.3. *EIS circuit components fitting values for all CP@Pd samples, using the circuit model shown in Figure 3c.*

CP N_{ALD} Pd	**R_s (Ω)**	**R_1 (Ω)**	**CPE_1 ($F.s^{(a-1)}$)**	**a_1**	**R_2 (Ω)**	**CPE_2 ($F.s^{(a-1)}$)**	**a_2**
CP 30c Pd	2.27	1.17	4.75×10^{-4}	0.66	178.28	0.087	0.96
CP 45c Pd	2.56	0.6	0.1051	0.18	61.03	0.092	0.97
CP 60c Pd	2	0.71	9.75×10^{-4}	0.67	26.55	0.091	0.92
CP 75c Pd	3.14	0.57	0.02	0.57	4.26	0.44	0.8
CP 150c Pd	3.13	1.69	1.21	1	1.3	0.27	0.26
CP 300c Pd	3.19	0.65	0.09	0.44	1.51	1.57	0.98
CP 450c Pd	2.78	0.7	0.049	0.48	1.12	2.11	1
CP 600c Pd	2.84	1.63	3.11	0.91	0.65	0.052	0.47
CP 50c Pt	2.2	0.33	0.037	0.64	1.58	1.09	0.68

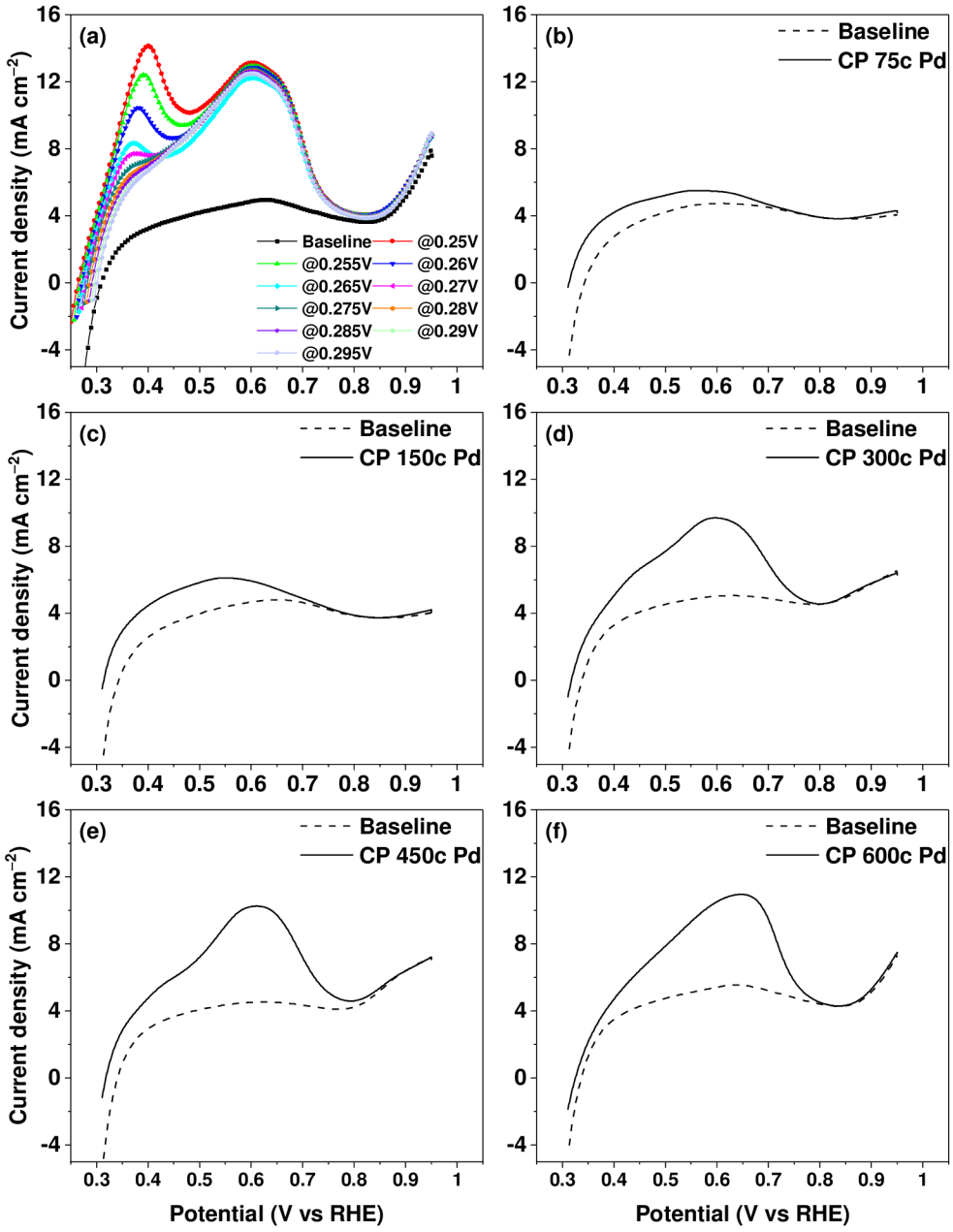

Figure 3.A.6. *Copper monolayer and bulk stripping LSV for (a) CP 600c Pd sample with Cu deposited at different potentials. Copper monolayer stripping for (b) CP 75c Pd; (c) CP 150c Pd; (d) CP 300c Pd; (e) CP 450c Pd and (f) CP 600c Pd at a deposition potential of 0.31 V vs RHE. Copper stripping and baseline LSV were performed in 0.5 M H_2SO_4 + 20mM $CuSO_4.5H_2O$, and 0.5 M H_2SO_4 respectively.*

If the relation (Eq. 3.A.5) that combines TOF and the number of active sites was taken into consideration, TOF is inversely proportional to the number of active sites (N). Therefore, as the number of active sites increases, the TOF decreases. However, the TOF is independent of the loading mass, as it is a measure of the intrinsic activity of each active site.

$$\mathrm{TOF} = \frac{\mathrm{I} \times \mathrm{N_A}}{2 \times \mathrm{F} \times \mathrm{N}} \tag{3.A.5}$$

Where (I) is the current density, (F) is the Faraday constant (96485.3 C), (N) is number of moles of active sites.

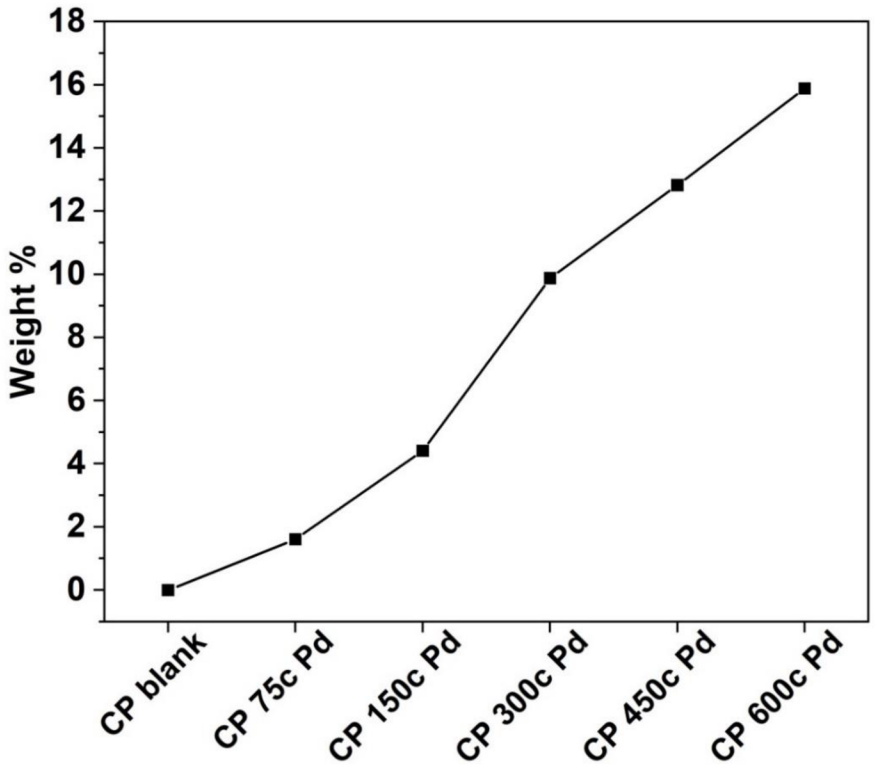

Figure 3.A.7. *The weight percent of the loaded Pd on the carbon substrat analysed by inductive coupled plasma atomic emission spectroscopy (ICP-OES). The connecting line is used for eye guidance.*

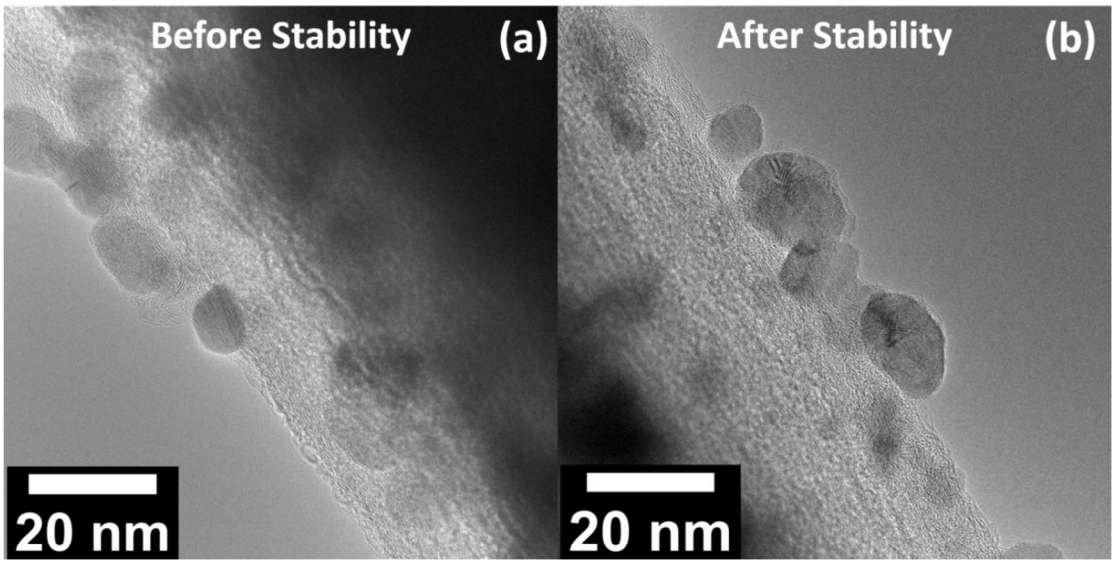

Figure 3.A.8. *TEM images for CP 600c Pd before and after stability measurements.*

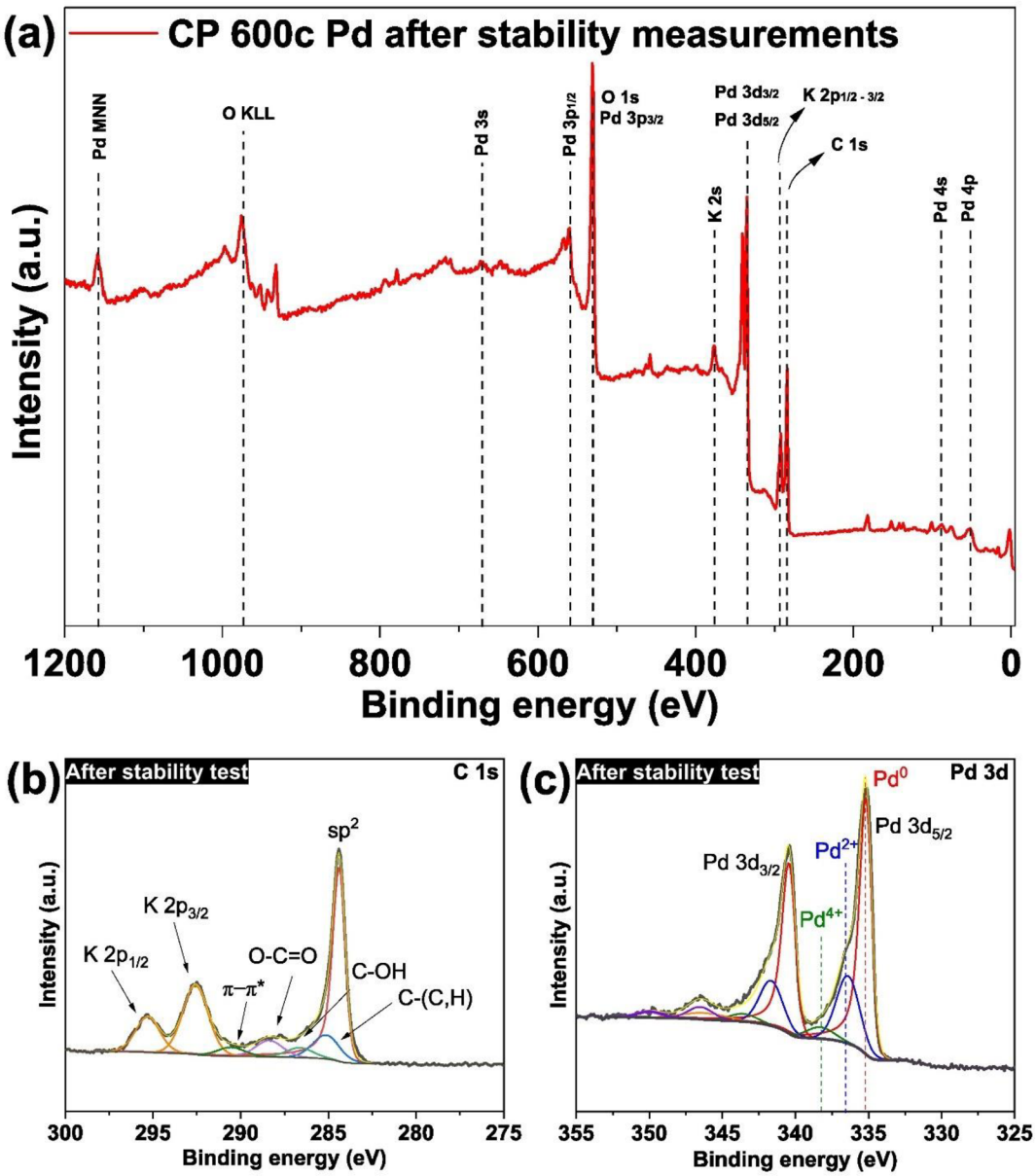

Figure 3.A.9. *XPS spectra for CP 600c Pd after stability measurements: (a) wide survey spectra; (b) and (c) high-resolution spectra for C1s and Pd 3d, respectively.*

After conducting the stability test, additional K peaks corresponding to K 2p was detected. These peaks were correlated with the adsorption of K^+ on the surface from the used KOH electrolyte. This occurred due to prolonged exposure of the sample to the KOH electrolyte as shown in the high-resolution spectra in **Figure 3.A.9b, c**. The high-

resolution C 1s spectrum exhibited four shoulder peaks at 284.8, 286.3, 288.0 and 290.2 eV corresponding to C-(CH) bonds, C-OH and O-C=O functional groups on the surface and π-π* bonds, besides the main peak at 284.0 eV attributed to sp^2 bonds. The intensity of the C 1s peak did not change significantly before and after the stability test. The atomic percentage of metallic Pd^0 decreased from 79.8 to 67.7% after stability test as shown in **Table 3.A.2**, while Pd^{4+} was detected in small quantities ranging between 6.7 and 5.4 atomic % before and after stability test.

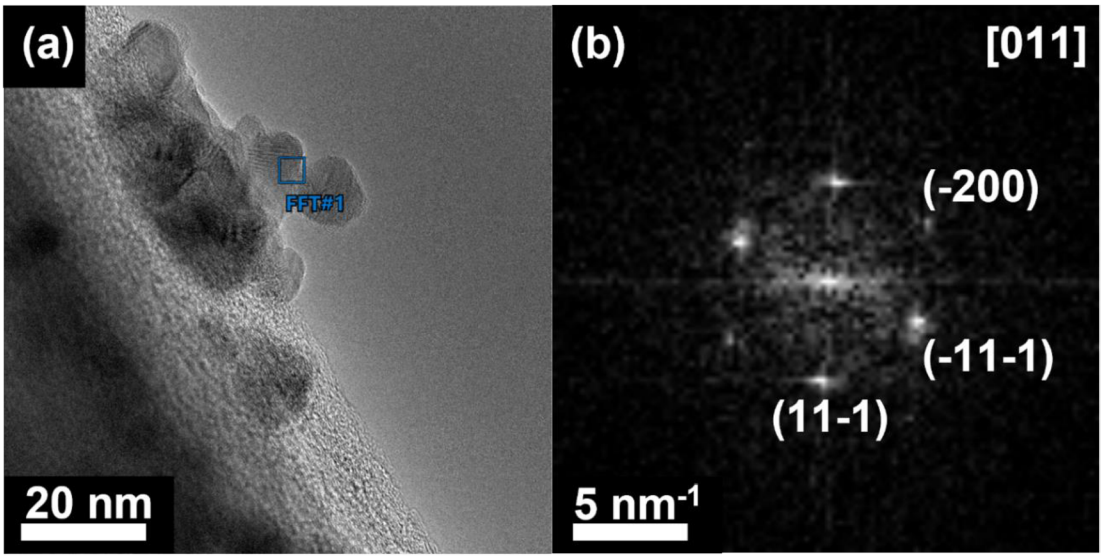

Figure 3.A.10. *(a) HR TEM image for CP 600c Pd after stability measurements; (b) FFT analysis corresponding to a blue rectangle in (a).*

Table 3.A.4. *Overview of Pd-based catalyst for HER, collected from the literature and compared with the values obtained in this work.*

Material	Substrate	Electrolyte	Overpotentials @10 mA cm^{-2}	Tafel slopes (mV dec^{-1})	Ref.
Pd@Ru	Palladium nanorods (Pd NRs)	1 M KOH	30	30	[68]
$NiCo_2S_4$/Pd	glassy carbon electrode	1 M KOH	83	70	[69]
$Pd_3P_{0.95}$ NPs	glassy carbon electrode	1 M KOH	75	64 PdP NPs-2	[70]
Cu-Pd, Pd	high surface area graphite (HSAG)	0.1 M KOH	145 mV, 63 mV	75, 42	[71]
Pd NPs	Carbonized wood membrane (CWM-2)	1 M KOH	302	64.5	[72]
Pd-Ru/C	glassy carbon electrode	1 M KOH	42	NA	[73]
Pd–P/Pt–Ni/C–Ac	Carbon	1 M KOH	21	55.4	[74]
CP 450c Pd	**Carbon paper (CP)**	**1 M KOH**	**5**	**47**	**This work**
CP 600c Pd	**Carbon paper (CP)**	**1 M KOH**	**4.55**	**49**	**This work**

References

[1] N.A. Kelly, Hydrogen production by water electrolysis, Woodhead Publishing Limited, 2014. https://doi.org/10.1533/9780857097736.2.159.

[2] V.R. Stamenkovic, D. Strmcnik, P.P. Lopes, N.M. Markovic, Energy and fuels from electrochemical interfaces, Nat. Mater. 16 (2016) 57–69. https://doi.org/10.1038/nmat4738.

[3] J. Durst, A. Siebel, C. Simon, F. Hasché, J. Herranz, H.A. Gasteiger, New insights into the electrochemical hydrogen oxidation and evolution reaction mechanism, Energy Environ. Sci. 7 (2014) 2255–2260. https://doi.org/10.1039/c4ee00440j.

[4] J. Zheng, W. Sheng, Z. Zhuang, B. Xu, Y. Yan, Universal dependence of hydrogen oxidation and evolution reaction activity of platinum-group metals on pH and hydrogen binding energy, Sci. Adv. 2 (2016) 1–9. https://doi.org/10.1126/sciadv.1501602.

[5] V.S. Bagotzky, N. V. Osetrova, Investigation of hydrogen ionization on platinum with the help of micro-electrodes, J. Electroanal. Chem. 43 (1973) 233–249. https://doi.org/10.1016/S0022-0728(73)80494-2.

[6] S.K. Park, D.Y. Chung, D. Ko, Y.E. Sung, Y. Piao, Three-dimensional carbon foam/N-doped graphene@MoS2 hybrid nanostructures as effective electrocatalysts for the hydrogen evolution reaction, J. Mater. Chem. A 4 (2016) 12720–12725. https://doi.org/10.1039/c6ta03458f.

[7] H. Jin, S. Sultan, M. Ha, J.N. Tiwari, M.G. Kim, K.S. Kim, Simple and Scalable Mechanochemical Synthesis of Noble Metal Catalysts with Single Atoms toward Highly Efficient Hydrogen Evolution, Adv. Funct. Mater. 30 (2020) 2–7. https://doi.org/10.1002/adfm.202000531.

[8] W. Sheng, H.A. Gasteiger, Y. Shao-Horn, Hydrogen Oxidation and Evolution Reaction Kinetics on Platinum: Acid vs Alkaline Electrolytes, J. Electrochem. Soc. 157 (2010) B1529. https://doi.org/10.1149/1.3483106.

[9] J.N. Tiwari, N.K. Dang, S. Sultan, P. Thangavel, H.Y. Jeong, K.S. Kim, Multi-heteroatom-doped carbon from waste-yeast biomass for sustained water splitting, Nat. Sustain. 3 (2020) 556–563. https://doi.org/10.1038/s41893-020-0509-6.

[10] M. Duan, T. Shu, J. Li, D. Zhang, L.Y. Gan, K.X. Yao, Q. Yuan, Boosting alkaline hydrogen evolution performance by constructing ultrasmall Ru clusters/Na+, K+-decorated porous carbon composites, Nano Res. 16 (2023) 8836–8844. https://doi.org/10.1007/s12274-023-5558-5.

[11] B.S. Kalanoor, H. Seo, S.S. Kalanur, Recent developments in photoelectrochemical water-splitting using WO 3 /BiVO 4 heterojunction photoanode: A review, Mater. Sci. Energy Technol. 1 (2018) 49–62. https://doi.org/10.1016/j.mset.2018.03.004.

[12] S.M. Thalluri, J. Rodriguez-Pereira, R. Zazpe, B. Bawab, E. Kolíbalová, L. Jelinek, J.M. Macak, Enhanced C-O Functionality on Carbon Papers Ensures Lowering Nucleation Delay of ALD for Ru towards Unprecedented Alkaline HER Activity, Small 19 (2023) 1–8. https://doi.org/10.1002/smll.202300974.

[13] N.K. Dang, M. Umer, P. Thangavel, S. Sultan, J.N. Tiwari, J.H. Lee, M.G. Kim, K.S. Kim, Surface enrichment of iridium on IrCo alloys for boosting hydrogen production, J. Mater. Chem. A 9 (2021) 16898–16905. https://doi.org/10.1039/d1ta02597j.

[14] S. Sultan, M.H. Diorizky, M. Ha, J.N. Tiwari, H. Choi, N.K. Dang, P. Thangavel, J.H. Lee, H.Y. Jeong, H.S. Shin, Y. Kwon, K.S. Kim, Modulation of Cu and Rh single-atoms and nanoparticles for high-performance hydrogen evolution activity in acidic media, J. Mater. Chem. A 9 (2021) 10326–10334. https://doi.org/10.1039/d1ta01067k.

[15] N. Mahmood, Y. Yao, J.W. Zhang, L. Pan, X. Zhang, J.J. Zou, Electrocatalysts for Hydrogen Evolution in Alkaline Electrolytes: Mechanisms, Challenges, and Prospective Solutions, Adv. Sci. 5 (2018). https://doi.org/10.1002/advs.201700464.

[16] E. Zoulias, E. Varkaraki, N. Lymberopoulos, C.N. Christodoulou, G.N. Karagiorgis, A review on water electrolysis, Tcjst 4 (2004) 41–71. http://hydrogenoman.com/docs/click on the attached.pdf.

[17] R.Q. Yao, Y.T. Zhou, H. Shi, Q.H. Zhang, L. Gu, Z. Wen, X.Y. Lang, Q. Jiang, Nanoporous Palladium-Silver Surface Alloys as Efficient and pH-Universal Catalysts for the Hydrogen Evolution Reaction, ACS Energy Lett. 4 (2019) 1379–1386. https://doi.org/10.1021/acsenergylett.9b00845.

[18] J. Ge, P. Wei, G. Wu, Y. Liu, T. Yuan, Z. Li, Y. Qu, Y. Wu, H. Li, Z. Zhuang, X. Hong, Y. Li, Ultrathin Palladium Nanomesh for Electrocatalysis, Angew. Chemie - Int. Ed. 57 (2018) 3435–3438. https://doi.org/10.1002/anie.201800552.

[19] F.H.B. Lima, J. Zhang, M.H. Shao, K. Sasaki, M.B. Vukmirovic, E.A. Ticianelli, R.R. Adzic, Catalytic activity - d-band center correlation for the O2 reduction reaction on platinum in alkaline solutions, J. Phys. Chem. C 111 (2007) 404–410. https://doi.org/10.1021/jp065181r.

[20] C. Zhang, Z. Zhou, X. Wang, J. Liu, J. Sun, L. Wang, W. Ye, C. Pan, A. Medical, C. Zhang, Synergy between Palladium Single Atoms and Small Nanoparticles Co-Anchored on Carbon Atom Self-Doped Graphitic Carbon Nitride Boosting Photocatalytic H2 Generation, (n.d.).

[21] Y. Lu, J. Wang, Y. Peng, A. Fisher, X. Wang, Highly Efficient and Durable Pd Hydride Nanocubes Embedded in 2D Amorphous NiB Nanosheets for Oxygen Reduction Reaction, Adv. Energy Mater. 7 (2017) 1–7. https://doi.org/10.1002/aenm.201700919.

[22] H. Lv, X. Chen, D. Xu, Y. Hu, H. Zheng, S.L. Suib, B. Liu, Ultrathin PdPt bimetallic nanowires with enhanced electrocatalytic performance for hydrogen evolution reaction, Appl. Catal. B Environ. 238 (2018) 525–532. https://doi.org/10.1016/j.apcatb.2018.07.060.

[23] S. Liu, X. Mu, H. Duan, C. Chen, H. Zhang, Pd Nanoparticle Assemblies as Efficient Catalysts for the Hydrogen Evolution and Oxygen Reduction Reactions, Eur. J. Inorg. Chem. 2017 (2017) 535–539. https://doi.org/10.1002/ejic.201601277.

[24] Y. Jia, T.H. Huang, S. Lin, L. Guo, Y.M. Yu, J.H. Wang, K.W. Wang, S. Dai, Stable Pd-Cu Hydride Catalyst for Efficient Hydrogen Evolution, Nano Lett. 22 (2022) 1391–1397. https://doi.org/10.1021/acs.nanolett.1c04840.

[25] J. Zheng, S. Zhou, S. Gu, B. Xu, Y. Yan, Size-Dependent Hydrogen Oxidation and Evolution Activities on Supported Palladium Nanoparticles in Acid and Base, J. Electrochem. Soc. 163 (2016) F499–F506. https://doi.org/10.1149/2.0661606jes.

[26] K. Gu, F. Wei, Y. Cai, S. Lin, H. Guo, Dynamics of Initial Hydrogen Spillover from a Single Atom Platinum Active Site to the Cu(111) Host Surface: The Impact of Substrate Electron-Hole Pairs, J. Phys. Chem. Lett. 12 (2021) 8423–8429. https://doi.org/10.1021/acs.jpclett.1c02019.

[27] H. Shen, H. Li, Z. Yang, C. Li, Magic of hydrogen spillover: Understanding and application, Green Energy Environ. 7 (2022) 1161–1198. https://doi.org/10.1016/j.gee.2022.01.013.

[28] U. Petek, F. Ruiz-Zepeda, M. Bele, M. Gaberšček, Nanoparticles and single atoms in commercial carbon-supported platinum-group metal catalysts, Catalysts 9 (2019). https://doi.org/10.3390/catal9020134.

[29] W. Xu, M. Cao, J. Luo, H. Mao, H. Gu, Z. Sun, Q. Liu, S. Zhang, Research progress on single atom and particle synergistic catalysts for electrocatalytic reactions, Mater. Chem. Front. 7 (2023) 1992–2013. https://doi.org/10.1039/d2qm01352e.

[30] C.B. Thompson, Y. Lu, A.M. Karim, Kinetic Synergy between Supported Ir Single Atoms and Nanoparticles during CO Oxidation Light-Off, Ind. Eng. Chem. Res. 60 (2021) 15960–15971. https://doi.org/10.1021/acs.iecr.1c02806.

[31] W. Zhou, J. Jia, J. Lu, L. Yang, D. Hou, G. Li, S. Chen, Recent developments of carbon-based electrocatalysts for hydrogen evolution reaction, Nano Energy 28 (2016) 29–43. https://doi.org/https://doi.org/10.1016/j.nanoen.2016.08.027.

[32] L. Zhang, J. Xiao, H. Wang, M. Shao, Carbon-Based Electrocatalysts for Hydrogen and Oxygen Evolution Reactions, ACS Catal. 7 (2017) 7855–7865. https://doi.org/10.1021/acscatal.7b02718.

[33] I. Dumitrescu, P.R. Unwin, J. V. MacPherson, Electrochemistry at carbon

nanotubes: Perspective and issues, Chem. Commun. 7345 (2009) 6886–6901. https://doi.org/10.1039/b909734a.

[34] J.P. Chen, S. Wu, Acid/Base-Treated Activated Carbons: Characterization of Functional Groups and Metal Adsorptive Properties, Langmuir 20 (2004) 2233–2242. https://doi.org/10.1021/la0348463.

[35] Y.J. Kang, H.K. Jo, M.H. Jang, G.J. Han, S.J. Yoon, K. Oh, J. Il Park, Acid treatment enhances performance of beads activated carbon for formaldehyde removal, Carbon Lett. 33 (2023) 397–408. https://doi.org/10.1007/s42823-022-00428-5.

[36] J.J. Senkevich, F. Tang, D. Rogers, J.T. Drotar, C. Jezewski, W.A. Lanford, G.C. Wang, T.M. Lu, Substrate-independent palladium atomic layer deposition, Chem. Vap. Depos. 9 (2003) 258–264. https://doi.org/10.1002/cvde.200306246.

[37] G. Zhang, S. Sun, D. Yang, J.P. Dodelet, E. Sacher, The surface analytical characterization of carbon fibers functionalized by H2SO4/HNO3 treatment, Carbon N. Y. 46 (2008) 196–205. https://doi.org/10.1016/j.carbon.2007.11.002.

[38] J.Y. Feng, R.K. Ramachandran, E. Solano, M.M. Minjauw, M. Van Daele, A. Vantomme, D. Hermida-Merino, A. Coati, H. Poelman, C. Detavernier, J. Dendooven, Tuning size and coverage of Pd nanoparticles using atomic layer deposition, Appl. Surf. Sci. 539 (2021). https://doi.org/10.1016/j.apsusc.2020.148238.

[39] J.W. Elam, A. Zinovev, C.Y. Han, H.H. Wang, U. Welp, J.N. Hryn, M.J. Pellin, Atomic layer deposition of palladium films on Al2O3 surfaces, Thin Solid Films 515 (2006) 1664–1673. https://doi.org/10.1016/j.tsf.2006.05.049.

[40] J.L. Figueiredo, M.F.R. Pereira, M.M.A. Freitas, J.J.M. Órfão, Characterization of Active Sites on Carbon Catalysts, Ind. Eng. Chem. Res. 46 (2007) 4110–4115. https://doi.org/10.1021/ie061071v.

[41] D.N. Goldstein, S.M. George, Surface poisoning in the nucleation and growth of palladium atomic layer deposition with Pd(hfac)2 and formalin, Thin Solid Films 519 (2011) 5339–5347. https://doi.org/10.1016/j.tsf.2011.02.037.

[42] N. Cheng, S. Stambula, D. Wang, M.N. Banis, J. Liu, A. Riese, B. Xiao, R. Li, T.K. Sham, L.M. Liu, G.A. Botton, X. Sun, Platinum single-atom and cluster catalysis of the hydrogen evolution reaction, Nat. Commun. 7 (2016) 13638. https://doi.org/10.1038/ncomms13638.

[43] M.T.X. Nguyen, M.K. Nguyen, P.T.T. Pham, H.K.P. Huynh, H.H. Pham, C.C. Vo, S.T. Nguyen, High-performance Pd-coated Ni nanowire electrocatalysts for alkaline direct ethanol fuel cells, J. Electroanal. Chem. 888 (2021) 115180. https://doi.org/10.1016/j.jelechem.2021.115180.

[44] M. Brun, A. Berthet, J.C. Bertolini, XPS, AES and Auger parameter of Pd and

PdO, J. Electron Spectros. Relat. Phenomena 104 (1999) 55–60. https://doi.org/10.1016/s0368-2048(98)00312-0.

[45] H. Yan, H. Cheng, H. Yi, Y. Lin, T. Yao, C. Wang, J. Li, S. Wei, J. Lu, Single-Atom Pd 1 /Graphene Catalyst Achieved by Atomic Layer Deposition: Remarkable Performance in Selective Hydrogenation of 1,3-Butadiene, J. Am. Chem. Soc. 137 (2015) 10484–10487. https://doi.org/10.1021/jacs.5b06485.

[46] G. Cha, I. Hwang, S. Hejazi, A.S. Dobrota, I.A. Pašti, B. Osuagwu, H. Kim, J. Will, T. Yokosawa, Z. Badura, Š. Kment, S. Mohajernia, A. Mazare, N. V. Skorodumova, E. Spiecker, P. Schmuki, As a single atom Pd outperforms Pt as the most active co-catalyst for photocatalytic H2 evolution, IScience 24 (2021). https://doi.org/10.1016/j.isci.2021.102938.

[47] D. Bhalothia, T.H. Huang, P.H. Chou, K.W. Wang, T.Y. Chen, Promoting formic acid oxidation performance of Pd nanoparticlesviaPt and Ru atom mediated surface engineering, RSC Adv. 10 (2020) 17302–17310. https://doi.org/10.1039/d0ra01303j.

[48] R. Westerström, C.J. Weststrate, J. Gustafson, A. Mikkelsen, J. Schnadt, J.N. Andersen, E. Lundgren, N. Seriani, F. Mittendorfer, G. Kresse, A. Stierle, Lack of surface oxide layers and facile bulk oxide formation on Pd(110), Phys. Rev. B - Condens. Matter Mater. Phys. 80 (2009) 1–11. https://doi.org/10.1103/PhysRevB.80.125431.

[49] R. Westerström, M.E. Messing, S. Blomberg, A. Hellman, H. Grönbeck, J. Gustafson, N.M. Martin, O. Balmes, R. Van Rijn, J.N. Andersen, K. Deppert, H. Bluhm, Z. Liu, M.E. Grass, M. Hävecker, E. Lundgren, Oxidation and reduction of Pd(100) and aerosol-deposited Pd nanoparticles, Phys. Rev. B - Condens. Matter Mater. Phys. 83 (2011) 1–10. https://doi.org/10.1103/PhysRevB.83.115440.

[50] X. Cheng, Z. Wang, Y. Mao, P. Hu, Evidence of the O-Pd-O and Pd-O4 structure units as oxide seeds and their origin on Pd(211): Revealing the mechanism of surface oxide formation, Phys. Chem. Chem. Phys. 21 (2019) 6499–6505. https://doi.org/10.1039/c8cp06224b.

[51] S. Yu, X. Cheng, Y. Wang, B. Xiao, Y. Xing, J. Ren, Y. Lu, H. Li, C. Zhuang, G. Chen, High activity and selectivity of single palladium atom for oxygen hydrogenation to H2O2, Nat. Commun. 13 (2022) 1–9. https://doi.org/10.1038/s41467-022-32450-6.

[52] X. Zhao, X. Li, D. Xiao, M. Gong, L. An, P. Gao, J. Yang, D. Wang, Isolated Pd atom anchoring endows cobalt diselenides with regulated water-reduction kinetics for alkaline hydrogen evolution, Appl. Catal. B Environ. 295 (2021) 120280. https://doi.org/10.1016/j.apcatb.2021.120280.

[53] T. Jiang, L. Yu, Z. Zhao, W. Wu, Z. Wang, N. Cheng, Regulating the intermediate affinity on Pd nanoparticles through the control of inserted-B atoms for alkaline hydrogen evolution, Chem. Eng. J. 433 (2022) 133525.

https://doi.org/10.1016/j.cej.2021.133525.

[54] R. Tan, D. Wu, S. Xu, Y. Zhu, D. Xiong, L. Wang, P. Yang, P.K. Chu, Electrocatalytic hydrogen evolution of palladium nanoparticles electrodeposited on nanographene coated macroporous electrically conductive network, Int. J. Hydrogen Energy 43 (2018) 2171–2183. https://doi.org/10.1016/j.ijhydene.2017.12.064.

[55] G. Valenti, A. Boni, M. Melchionna, M. Cargnello, L. Nasi, G. Bertoni, R.J. Gorte, M. Marcaccio, S. Rapino, M. Bonchio, P. Fornasiero, M. Prato, F. Paolucci, Co-axial heterostructures integrating palladium/titanium dioxide with carbon nanotubes for efficient electrocatalytic hydrogen evolution, Nat. Commun. 7 (2016) 1–8. https://doi.org/10.1038/ncomms13549.

[56] T. Shinagawa, A.T. Garcia-Esparza, K. Takanabe, Insight on Tafel slopes from a microkinetic analysis of aqueous electrocatalysis for energy conversion, Sci. Rep. 5 (2015) 1–21. https://doi.org/10.1038/srep13801.

[57] P. Liu, Z. Huang, X. Gao, X. Hong, J. Zhu, G. Wang, Y. Wu, J. Zeng, X. Zheng, Synergy between Palladium Single Atoms and Nanoparticles via Hydrogen Spillover for Enhancing CO2 Photoreduction to CH4, Adv. Mater. 34 (2022) 1–11. https://doi.org/10.1002/adma.202200057.

[58] J. Li, J. Hu, M. Zhang, W. Gou, S. Zhang, Z. Chen, Y. Qu, Y. Ma, A fundamental viewpoint on the hydrogen spillover phenomenon of electrocatalytic hydrogen evolution, Nat. Commun. 12 (2021) 1–12. https://doi.org/10.1038/s41467-021-23750-4.

[59] C. Wei, R.R. Rao, J. Peng, B. Huang, I.E.L. Stephens, M. Risch, Z.J. Xu, Y. Shao-Horn, Recommended Practices and Benchmark Activity for Hydrogen and Oxygen Electrocatalysis in Water Splitting and Fuel Cells, Adv. Mater. 31 (2019) 1–24. https://doi.org/10.1002/adma.201806296.

[60] L.L. Fang, Q. Tao, M.F. Li, L.W. Liao, D. Chen, Y.X. Chen, Determination of the real surface area of palladium electrode, Chinese J. Chem. Phys. 23 (2010) 543–548. https://doi.org/10.1088/1674-0068/23/05/543-548.

[61] L. Yang, Y. Tang, S. Luo, C. Liu, H. Song, D. Yan, Palladium Nanoparticles Supported on Vertically Oriented Reduced Graphene Oxide for Methanol Electro-Oxidation, ChemSusChem 7 (2014) 2907–2913. https://doi.org/10.1002/cssc.201402352.

[62] J. Shu, R. Li, Z. Lian, W. Zhang, R. Jin, H. Yang, S. Li, In-situ oxidation of Palladium–Iridium nanoalloy anchored on Nitrogen-doped graphene as an efficient catalyst for methanol electrooxidation, J. Colloid Interface Sci. 605 (2022) 44–53. https://doi.org/10.1016/j.jcis.2021.07.056.

[63] K. Naga Mahesh, R. Balaji, K.S. Dhathathreyan, Palladium nanoparticles as hydrogen evolution reaction (HER) electrocatalyst in electrochemical methanol

reformer, Int. J. Hydrogen Energy 41 (2016) 46–51. https://doi.org/10.1016/j.ijhydene.2015.09.110.

[64] D. Voiry, M. Chhowalla, Y. Gogotsi, N.A. Kotov, Y. Li, R.M. Penner, R.E. Schaak, P.S. Weiss, Best Practices for Reporting Electrocatalytic Performance of Nanomaterials, ACS Nano 12 (2018) 9635–9638. https://doi.org/10.1021/acsnano.8b07700.

[65] C. Costentin, G. Passard, J.M. Savéant, Benchmarking of homogeneous electrocatalysts: Overpotential, turnover frequency, limiting turnover number, J. Am. Chem. Soc. 137 (2015) 5461–5467. https://doi.org/10.1021/jacs.5b00914.

[66] M. Batool, A. Hameed, M.A. Nadeem, Recent developments on iron and nickel-based transition metal nitrides for overall water splitting: A critical review, Coord. Chem. Rev. 480 (2023) 215029. https://doi.org/10.1016/j.ccr.2023.215029.

[67] A. Lasia, Mechanism and kinetics of the hydrogen evolution reaction, Int. J. Hydrogen Energy 44 (2019) 19484–19518. https://doi.org/10.1016/j.ijhydene.2019.05.183.

[68] Y. Luo, X. Luo, G. Wu, Z. Li, G. Wang, B. Jiang, Y. Hu, T. Chao, H. Ju, J. Zhu, Z. Zhuang, Y. Wu, X. Hong, Y. Li, Mesoporous Pd@Ru Core-Shell Nanorods for Hydrogen Evolution Reaction in Alkaline Solution, ACS Appl. Mater. Interfaces 10 (2018) 34147–34152. https://doi.org/10.1021/acsami.8b09988.

[69] G. Sheng, J. Chen, Y. Li, H. Ye, Z. Hu, X.Z. Fu, R. Sun, W. Huang, C.P. Wong, Flowerlike NiCo2S4 Hollow Sub-Microspheres with Mesoporous Nanoshells Support Pd Nanoparticles for Enhanced Hydrogen Evolution Reaction Electrocatalysis in Both Acidic and Alkaline Conditions, ACS Appl. Mater. Interfaces 10 (2018) 22248–22256. https://doi.org/10.1021/acsami.8b05427.

[70] T. Xia, M. Zhao, B. Tong, Z. Kang, Y. Wu, W. Ding, B. Feng, Synthesis of PdP nanoparticles as electrocatalysts for hydrogen evolution reaction in an alkaline medium, Nano 14 (2019) 1–10. https://doi.org/10.1142/S1793292019500590.

[71] M. Nunes, D.M. Fernandes, M. V. Morales, I. Rodríguez-Ramos, A. Guerrero-Ruiz, C. Freire, Cu and Pd nanoparticles supported on a graphitic carbon material as bifunctional HER/ORR electrocatalysts, Catal. Today 357 (2020) 279–290. https://doi.org/10.1016/j.cattod.2019.04.043.

[72] W. Deng, Y. Li, F. Wang, Q. Ma, S. Min, Palladium Nanoparticles Supported on Basswood-Derived Porous Carbon Membrane as Free-Standing Cathodes for Efficient pH-Universal Electrocatalytic H2 Evolution, Electrocatalysis 12 (2021) 340–349. https://doi.org/10.1007/s12678-021-00657-8.

[73] X. Qin, L. Zhang, G.L. Xu, S. Zhu, Q. Wang, M. Gu, X. Zhang, C. Sun, P.B. Balbuena, K. Amine, M. Shao, The Role of Ru in Improving the Activity of Pd toward Hydrogen Evolution and Oxidation Reactions in Alkaline Solutions, ACS Catal. 9 (2019) 9614–9621. https://doi.org/10.1021/acscatal.9b01744.

[74] Y. Wu, M. Zhao, J.P. Cao, J. Xu, T. Jin, N. Asao, Amorphous/low-crystalline core/shell-type nanoparticles as highly efficient and self-stabilizing catalysts for alkaline hydrogen evolution, Chem. Commun. 56 (2020) 8984–8987. https://doi.org/10.1039/d0cc03016c.

Chapter 4: General conclusion and outlook

This doctoral thesis focused on the controlled synthesis of Pd NPs with tunable properties for HER and MOR, through the in-depth understanding of the reaction mechanisms taking place during ALD nucleation and growth, and the effect of the prepared material for HER and MOR. In addition, OER transition Cu_2O has been tuned from p-type to n-type and used as photoabsorber with the support of ultrathin ALD layers to reduce its oxidative dissolution during the water splitting process. The following general conclusions can be drawn from this work:

- Reproducible ALD route for the synthesis of Pd NPs on various high surface area substrates, (such as TNTs) was developed and optimized, in addition to the treated CPs for better hydrophilicity that proved to be very effective in supporting the HER mechanism and improve the charge transfer. The Pd NPs exhibited a narrow size distribution, a high loading density, and a strong adhesion to the substrates. The Pd NPs were characterized by various techniques, such as XRD, TEM, XPS, and electrochemical measurements.

- The Pd NPs decorated on TNTs showed a remarkable electrocatalytic performance for MOR in 1M KOH. The Pd/TNTs electrodes had a high resistance to CO poisoning, with considerable currents, and a good stability for MOR. The results were compared with Pd loaded on other substrates, and proved to have better resistivity against CO, thanks to the oxophilic effect of TNTs as a substrate that has supported the MOR. It is worth noting that the combination of Pd and TNTs that already showed good adhesion, provided a large surface area substrate that are highly tunable and stable, along with the unidirectional 1D and favorable electron transfer.

- The Pd NPs deposited on CPs by ALD were found to form Pd SAs, atomic clusters, and NPs, which had a synergistic effect on the alkaline HER. The Pd SAs and NPs catalysts had a superior HER performance and very low overpotentials than the commercial Pt/C catalysts and other Pd-based catalysts presented in the literature. However, the overpotentials and Tafel slope values became close to that of 50c Pt loaded on the treated CPs at N_{ALD} = 450 c Pd. The mechanism of the synergistic effect was revealed by XPS and high-resolution TEM images and characterizations, which showed that the Pd SAs and NPs modulated the electronic structure and facilitated the hydrogen spillover effect.

Based on the results presented in this thesis, further research could be carried out as described below:

- Expanding the potential of ALD in the synthesis of other noble metal NPs, the exploration can include metals beyond the commonly studied Pd and Pt, such as Rhodium (Rh), Iridium (Ir), and Gold (Au). By using ALD as a precise technique to synthesize these metals, this could unlock a spectrum of possibilities for catalytic applications across diverse substrates. For instance, Rhodium NPs synthesized via ALD could exhibit unique catalytic properties in reactions like formic acid oxidation, which is crucial in fuel cells. Similarly, Ir and Au NPs synthesized through ALD could be investigated for their efficiency in glycerol oxidation. Furthermore, exploring the potential of ALD-synthesized noble metal NPs for carbon dioxide reduction reactions using the combination of materials presented in this thesis could offer sustainable pathways for mitigating greenhouse gas emissions. This expansion of ALD techniques to covers a broader range of noble metals and catalytic reactions, holds promise for addressing critical challenges in energy conversion and environmental sustainability.

- It is also possible to use the ALD technique to fabricate bimetallic or multimetallic NPs, broadening the scope beyond single metal NPs. Combinations such as Pd-Pt, Pd-Ru, Pt-Ru, and Pt-Ir could be synthesized on diverse substrates, offering a more possibilities for investigating their electrocatalytic properties. By exploring these combinations, which in principle complicates the study of the electrochemical reactions due to the different interactions of the studied material with the electrolytes and the formation of varios compounds, including MOR, HER, ORR, and EOR. This investigation can be extended to study the interplay between composition, size, shape, and structure of bimetallic or multimetallic NPs and their electrocatalytic performance and stability. For instance, understanding how the atomic arrangement at the NP interface influences catalytic activity could lead to the development of highly efficient and durable catalysts for various energy conversion and environmental remediation applications. Through experimentation and characterization, insights gained from studying these complex NPs could introduce a way for the design of next-generation catalysts with tailored properties for specific electrochemical processes.

- In addition to the ALD technique, methods like plasma treatment, thermal annealing, or chemical processing (such as chemical reduction) can be integrated with the synthesized noble metals NPs and substrates and finely tuned to amplify their electrocatalytic performance. For instance, plasma treatment can facilitate surface functionalization, altering the chemical composition and surface energy of the NPs and substrates to optimize catalytic activity. Similarly, thermal annealing can induce structural transformations, such as grain growth or phase transitions, enhancing the stability and conductivity of the catalysts. Additionally, chemical reduction methods can be employed to tailor the electronic structure of the NPs, optimizing their reactivity towards specific electrochemical reactions. Through systematic experimentation and characterization using techniques such as XPS, SEM, and EIS, this can clarify the underlying mechanisms behind these modifications. By gaining insights into the structure-property relationships that may lead to enhanced electrocatalytic performance, which can devise the strategies for the design of advanced catalyst materials with superior activity, selectivity, and durability for a wide range of electrochemical applications.

- The proposed utilization of ALD techniques for synthesizing noble metal NPs on a wide range of substrates presents a crucial part for the understanding of electrocatalytic process reactions. This approach involves the exploration of various substrate materials. Since in this thesis, the effect of using metal oxide such as TiO_2 NTs and the chemically treated and highly conductive carbon substrate. Additionally, it is possible to study the interactions between noble metal NPs and metal oxides, metal nitrides, metal carbides, metal phosphides, and metal sulfides, in order to evaluate their electrocatalytic performance for water splitting reactions. Employing precise control over ALD deposition parameters, such as precursor chemistry, temperature, and cycle number, is essential for achieving uniform NP growth and morphology while minimizing defects and impurities. Characterization techniques, including XRD, XPS, and TEM, facilitate comprehensive analysis of the structural and compositional properties of the resulting noble metal NP-substrate interfaces. Surface engineering strategies, including pre-treatment methods and interfacial modifiers, are employed to enhance adhesion, stability, and reactivity, thereby ensuring optimal electrocatalytic performance. Careful evaluation of catalytic activity, kinetics, selectivity, and stability under relevant operating conditions

serves as a crucial benchmark for assessing the efficiency of ALD-synthesized NP-substrate systems. Through material design and optimization, it is possible to explain the catalytic behavior and tailor noble metal NP-substrate configurations for enhanced electrochemical performance.

- The potential application of ALD techniques in fabricating noble metal NPs on 3D porous structures, including aerogels, foams, and scaffolds, introduces a new dimension to the study. By evaluating the characteristics of 3D porous structures, such as high porosity, large surface area, and enhanced mass transport properties, this aims to explore and the advantages of these substrates in catalytic applications. ALD offers precise control over NP deposition on complex geometries, enabling the fabrication of well-defined noble metal NP architectures within the porous network. Characterization techniques, including SEM and gas adsorption analysis such as Brunauer–Emmett–Teller (BET) to assess the resulting noble metal NP-3D porous structure interfaces surface area. Through evaluation of electrocatalytic performance, it is possible to study the influence of NP morphology, distribution, and interfacial interactions on catalytic activity and stability. The integration of ALD-synthesized noble metal NPs with 3D porous structures holds significant promise since several studies has been talking about the effect of the exposed crystal planes in the activity of the catalyst. Therefore, implementing these high surface area substrates can help in exposing specific catalytically active crystalline planes leading for more selective reactions.

- The identification of Pd SAs and NPs has been confirmed through deep analysis employing XPS and TEM in this thesis. In explaining the HER mechanism, particular attention has been given to understanding the synergistic effects observed when SAs and NPs are combined. To support this understanding, density functional theory (DFT) calculations can offer a powerful tool for predicting the sequential steps of the process, accounting for bonding strengths and their impact on HER kinetics. This supplementary validation is pivotal for providing additional insights into any uncertainties surrounding the proposed mechanism, thus solidifying the overall credibility of the findings.

Summary

Optimizing the synthesized electrode activity is crucial when designing the catalyst, whether it is related to the morphological structure or complementing it with other materials to serve a different purpose. Previous studies on various electrocatalysts structures in the recent years have provided a basic understanding of the work in this thesis. However, the controllability of the deposited electrocatalyst and its structure has only been roughly estimated. It is crucial to work on a process that ensures reproducibility and defines the necessary morphology, as these are the main factors when assessing catalyst performance.

The aim of this study was to develop a combination of the noble metal Pd with other high surface area materials to limit the poisoning effect, which is a major issue in the use of direct methanol fuel cells. Additionally, Pd is a promising water splitting catalyst for HER, but its performance is not comparable to that of Pt, which is considered the benchmark material. The aim of the study was to identify a catalyst structure, in combination with a tuned substrate, that would enable the Pd catalyst to achieve HER activity comparable to that of Pt.

Chapters 2 and **3** are the main sections related to the Pd catalyst. **Chapter 2** discusses the use of TNTs with high surface area as a support for MOR. TNTs are selected due to their ease of reproduction, high surface area, and high stability. However, the main advantage of using TNTs as substrates is their oxyphilic nature and ability to act as electron donors, supporting the conversion of intermediates to final products such as CO_2. The activity of the ALD-synthesized Pd NPs depends on their coupling with the substrate to provide longevity during the oxidation reaction. **Chapter 3** discusses the synthesis of an ALD Pd catalyst coupled with a highly conductive carbon substrate that facilitates HER activity. The catalyst shows comparable activity to Pt, a benchmark material. The study also investigates the mechanism of the HER reaction, attributing the high catalytic activity to the synergistic effect of SAs and NPs. Overall, Pd performs well as a standalone catalyst. However, combining it with other materials as a support can significantly reduce the overpotentials for HER and overcome the intermediates that can obstruct the reaction in the case of MOR as an electrode for DMFCs.